A Preliminary Musculoskeletal Model of the German Shepherd Lumbosacral Spine

A thesis presented in partial fulfilment of the
requirements for the degree of

MASTER OF SCIENCE

in

Animal Science

at Massey University, Manawatū, New Zealand.

Sophie Anna Reed

2017

Abstract

German shepherd dogs (GSD) are commonly utilised in police and military forces, where they undertake physically demanding working roles. These duties, combined with the typical GSD musculoskeletal conformation, consequently result in a high incidence of degenerative lumbo-sacral stenosis in this breed. This debilitating condition compromises the welfare of the animal and often results in premature loss from service.

A preliminary mathematical musculoskeletal model was developed in the AnyBody Modelling System software platform from computed tomography imagery and muscle dissection. Positions of hard and soft tissue elements were recorded from the specimen to construct this patient-specific model. Inverse dynamics simulations were run with incremental alterations of two muscle input parameters: muscle fibre length and sarcomere length. The effect of these parameters was found to be extremely sensitive on the model output values, with minor input variations resulting in major output variations.

Histology data was obtained from muscle excised in the dissection, and indicated variability in muscle sarcomere length up to 0.681 μm within the muscle and an average of 0.389 μm between GSD muscles. The sensitivity analysis indicated a 0.1 μm variation in sarcomere length exceeded the set threshold of ± 2.5 % from the measured sarcomere length output value of strength for the muscle sacrocaudalis dorsalis medialis. Muscle length sensitivity indicated a 1 mm input variation remained within the strength output threshold, while a 2 mm variation exceeded the threshold.

This research resulted in the development of a preliminary and functional biomechanical model of the GSD lumbo-sacral spine capable of simulation studies. The results of the inverse dynamics sensitivity analysis identified the critical effect of variation of muscle fibre length and sarcomere length as muscle input parameters, and emphasised the requirement of precise muscle measurement, specific to each individual muscle.

Acknowledgements

Research is never the work of one person. Behind the scenes is a village of stakeholders. Among the many who have made up my village are the following colleagues and mentors whom I would like to thank, jointly and individually, for their help along the way. I am so fortunate in having been able to work with you all.

This project may well never have come to fruition without the help of Dr Bob Colborne, my chief adviser and mentor. My sincere thanks for your guidance and oversight throughout this complex project. I thank you for your trust in me as well as your support and encouragement.

For your extra support and guidance around welfare, thank you Dr Ngaio Beausoleil. You recognised the possibilities of what could be achieved by merging my diverse backgrounds of animal science and design.

To Dr Kevin Stafford, for helping sow the seeds for this project. Your open door and your open mind supported me along the way.

To my ‘technician extraordinaire’, James Wang - my sincere thanks for your impressive work ethic and dedication.

I would also like to acknowledge the assistance of these Massey University staff; your input has been invaluable:

Nicki Moffatt and your exceptional Radiology Department, Dr Matthew Perrott for guidance with histology, Alan Nutman for your anatomy expertise, and the numerous IVABS staff who made time to share their specialist knowledge.

And finally, to the Working Dog Centre - you understood the need for this research and, in so doing, provided the opportunity to make a contribution in a field of special interest to me.

Table of Contents

List of Figures

List of Tables

List of Abbreviations

AMS	AnyBody Modeling System
AR	Axial rotation
CT	Computed tomography
DLSS	Degenerative lumbosacral stenosis
eps	strain
FE	Flexion and extension
GSD	German shepherd dog
k	stiffness
LB	Lateral bending
Lf_{nom}	Nominal muscle fibre length (cm)
Lf_{opt}	Optimal muscle fibre length (cm)
Lm_{nom}	Nominal muscle length (cm)
Lmt	Muscle-tendon element length (cm)
Ls_{nom}	Nominal sarcomere length (μm)
Ls_{opt}	Optimal sarcomere length (μm)
$Ls_{opt\ (canine)}$	Optimum canine sarcomere length (2.5 μm)
Lt_{nom}	Nominal tendon length (cm)
NZ	New Zealand
ρ_{canine}	Uniform canine muscle tissue density (1.059 g/cm^3)
PA	Pennation angle (°)

PCSA	Physiological cross-sectional area
PDS	Police Dog Section
ROM	Range of motion
TLEM	Twente Lower Extremity Model
USMWD	United States military working dog
Vol	Volume (cm^3)
2E	Two-element muscle

1. INTRODUCTION

1.1 General introduction

The German shepherd dog (GSD) is commonly used for police and military work worldwide, as well as for search and rescue, and service and assistance roles. GSDs in law enforcement roles are required to fulfil physically demanding duties that include activities such as high-speed locomotion, heavy jumping and landing and ballistic movements. The high intensity of these strenuous activities impacts on many working GSDs that, consequently are prematurely lost from service. A predominant cause of this loss involves column diseases, most commonly degenerative lumbo-sacral stenosis (DLSS), a multifactorial degenerative disorder of the lumbo-sacral articulation, with ensuing *cauda equina* compression which manifests as debilitating pain (Meij & Bergknut, 2010). GSDs are reputed to have the highest incidence of DLSS across all canine breeds, with this propensity thought to be attributed to abnormal lumbar vertebral characteristics, along with the popularity of this breed in taxing military and police service roles (Worth, 2014).

The early retirement or euthanasia of these dogs has wide-reaching welfare, logistical and financial implications. Welfare can be compromised when sensory inputs of the physical and functional domains are processed, together with cognitive and affective inputs, resulting in a negative expression in the mental domain of the animal's conscious subjective experience (Mellor, Patterson-Kane, & Stafford, 2009). Factors contributing to a decreased state of welfare in GSDs with debilitating spinal cord diseases include chronic pain and the frustration of being unable to engage in work roles and express behaviours for which they were bred. Other implications of considerable wastage include the significant investment of time and costs of breeding, initial training and maintenance, as well as the logistical problems encountered regarding replacement dogs when a significant number of GSDs are retired before their expected operational life is achieved.

Working dog breeding programmes appoint genetically superior GSDs as breeding stock to maximise the likelihood of their offspring possessing optimal characteristics. This selective practice aims to maintain successful working lines and select against hereditary physical traits that are undesirable in working roles, such as DLSS. As transitional vertebral anomalies that predispose GSD to DLSS have been identified as familial, this is a worthwhile consideration when selecting breeding stock to minimise the occurrence of breakdown of the lumbo-sacral joint (Morgan, Bahr, Franti, & Bailey, 1993). A greater depth of research is required to identify all indicators of DLSS and enable selection for optimal lumbo-sacral joint conformation.

Resolving DLSS and other painful debilitating conditions in GSDs is achievable through surgical decompression of the *cauda equina* and stabilisation of the lumbo-sacral or other caudal lumbar articulations. These procedures successfully reduce pain and disability associated with the condition; however, further research is required around the lumbo-sacral articulation to optimise treatment intervention options in working dogs (Worth, 2014). Biomechanical testing is a viable option to investigate DLSS in the natural skeletal conformations of working GSDs that are affected by the condition. Testing is required to investigate the efficiency of surgical intervention by assessing potential strength and failure resistance of the adaptation (Worth, 2014). Additionally, biomechanical analysis can be used to pre-empt possible complications through analysis of the onwards effects on surrounding hard and soft tissues, caused by fusing spinal joints.

Development of a biomechanical canine musculoskeletal model of the lumbar spine will allow investigation into the forces and torques which the lumbo-sacral spine of the working GSD is subjected to throughout their high levels of physical activity. Inverse dynamics simulation studies will enable the identification of any discrete weak points in the spine that increase GSDs propensity to injury. Investigating the mechanics of such breakdown would thus allow prediction of spinal morphologies that predispose GSDs to breakdown, and avoid investing high-impact training in dogs possessing such characteristics. As such, the ability to scale this canine model for application to other GSDs is a crucial component for its success. This modelling tool can be employed to assist in lowering the prevalence of DLSS in the GSD working population, which will subsequently improve welfare and longevity in active service, and minimise the requirement for euthanasia or re-homing (Stafford, 2006).

The primary objective of this research project was to develop a three-dimensional musculoskeletal model of a single GSD lumbo-sacral spine, comprised of physiologically valid muscles attached to anatomically correct positions on articulated bone segments. A scalable mathematical model was constructed in the AnyBody Modeling System (AMS) software, a proprietary platform widely used in human medicine for orthopaedic modelling, simulating and analysing the neuromusculoskeletal system using AnyScript, a programming language similar to C++. Kinematic analysis and inverse dynamics simulations provided output data quantifying the linear forces crossing, torsional moments around, and muscle work done across lumbar and lumbo-sacral joints of the GSD. Medical imaging of the pelvis, sacrum and lumbar spine provided the three-dimensional renderings of the individual vertebral elements of the model that were reassembled into their true orientations. Soft tissue morphometric data was primarily obtained through careful dissection of a GSD cadaver and microscopic examination, while other soft tissue mechanical data was added from the literature. References acknowledging techniques used for the collection of musculoskeletal data in this model are provided in the Methods and Materials chapter (Chapter 3). Muscle and ligament elements were attached to three-dimensional nodes on the skeletal model, to simulate muscle action. All node coordinates were mapped using a three-dimensional camera system (Qualisys) and solid modelling computer-aided design and computer-aided engineering software (SolidWorks).

This preliminary working model is the crucial initial phase of a larger modelling programme required to further develop this GSD model to include the pelvic limb and to determine ground reaction forces transmitted through the spine during dynamic activities. Subsequent modelling will aim to manipulate hard and soft tissue variables to examine the effect of different spinal conformations on the forces and torques across motion segments, and evaluate which spinal conformations predispose to spinal injury. Further scope includes predictive modelling of orthopaedic procedures to determine the functional outcome and investigations into prominent injuries and clinical conditions through tarsal, elbow, and stifle joint mechanical function in both working and companion dogs of various breeds.

1.2 Outline of thesis

Following this introduction, a review of the literature (Chapter 2) presents a comprehensive background of the research topic. Materials and methods are then described in detail (Chapter 3), followed by the results (Chapter 4), which are analysed in the discussion (Chapter 5). Conclusions regarding the overall research embarked upon are drawn in Chapter 6. Ancillary datasets to Chapter 4 are listed in Appendices I and II.

2. REVIEW OF LITERATURE

2.1 Welfare of German shepherd working dogs

2.1.1 Working German shepherd role requirements

The German shepherd dog (GSD) operates within police and military forces globally, as well as in search and rescue, and assistance or service capacities, undertaking demanding roles that require animals that are both physically capable and of suitable temperament (Stafford, 2006). The prominence of this breed among many law enforcement agencies is a testament to the alignment of their typical characteristics to this line of work. Preferred attributes of the GSD include their large size, strength, speed, and endurance, along with their willingness to work, high level of drive, courage, intelligence, and environmental adaptability (Stafford, 2006; Worth, 2014).

Their role in the New Zealand Police force entails patrol duties, tracking criminals, apprehension of criminals, armed offender operations, and identification work. The NZ Police working line of GSDs have been bred, reared and trained to fulfil these duties effectively and safely, therefore, these dogs are expected to accomplish the requirements of their role (Stafford, 2006). These working dogs are utilised for a variety of activities, which inadvertently may lead to some degree of welfare compromise, regardless of the handler's intentions. The range of welfare issues these dogs are subjected to are typically specific to their particular function and activity, such as stress-inducing tracking from a crime scene at night when both the dog and handler may be in danger (Stafford, 2006, 2013). Despite these potentially detrimental effects of the GSDs' training and work, for many of them, working is largely a positive experience. Selective breeding for desirable physical attributes and behaviours undertaken by the NZ Police results in GSDs that are predisposed to engage in their required duties, ideally minimising the likelihood of adverse experiences capable of compromising GSD welfare (Stafford, 2006).

The suggested considerations for achieving good welfare of these NZ Police GSDs emphasise the importance of identifying trends in the incidence of injury, illness, and adverse experiences that have welfare implications, or lead to animals being withdrawn from active duty. Identifying the factors conducive to welfare compromise enables appropriate strategies to be investigated and implemented to mitigate these losses, and improve the health and wellbeing of GSD tasked to the NZ Police force (Worth et al., 2013).

2.1.2 Defining animal welfare

The welfare status of an animal may be defined as the integrated outcome of all sensory and other neural inputs, combined from environments both internal and external to the animal. These inputs are cognitively processed and interpreted according to the animal's species-specific and individual nature and experience, then perceived consciously (Mellor et al., 2009). While animal welfare definitions somewhat lack integration, there is consensus on the inclusion of the three general orientations of biological function, affective state and natural state (Fraser, 2003; Mellor et al., 2009). Subsequently, good welfare is achieved through physical health, adaptation to interactions with positive emotional experiences and lack of suffering, and minimal deviation from conditions of the original wild state of the species, hence supression of most natural behaviours, respectively (Mellor et al., 2009).

The state of welfare experienced can be assessed by the degree to which the needs of the animal are, or are not, being met across the five interacting disciplines first put forward by Mellor and Reid, namely nutritional, environmental, health, behavioural and mental domains (Mellor et al., 2009). The sensory and neural inputs are processed by the animal regarding the largely physical or functional domains of nutrition, environment, health and behaviour, supplemented with cognitive and affective inputs, and processed prior to the mental domain expression of the animal's conscious subjective experience. The character of this conscious experience is positioned on the welfare-suffering continuum, ranging between extreme suffering and high welfare states. An animal's placement on this continuum ultimately determines the final welfare status (Mellor et al., 2009). Additionally, the intensity of the affective experience domain is likely altered at a rate proportional to the noxiousness of the subjective experience in the physical and functional domains, and in turn impacts comparably on the animal's welfare status (Mellor et al., 2009).

Ultimately, the status of animal welfare, wherever it may lie on the welfare continuum, denotes the integrated outcome of all brain inputs, internal and external to the animal. The precursor to the welfare status is an internal subjective experience that results in experiences or feelings ranging from positive, through neutral, to negative. It cannot be measured directly as this notion is too simple to adequately represent the complex assessment that requires scientifically informed appraisal of all contributing factors, hence, a discrete overall value of wellbeing is not possible.

2.1.3 Welfare implications for working German shepherds

The welfare of working dogs across the disciplines varies considerably; however, there is a common dearth of information on the longevity, health and wellbeing of working dogs. While welfare considerations are suggested for any service animal, investigation into the impact of training for and engagement in working roles on the wellbeing of the dogs is lacking (Stafford, 2006; Worth et al., 2013). Conclusions regarding a working dog's wellbeing, and any degree of welfare compromise, cannot be reliably drawn from this scanty information, therefore, research into the distress encountered by working dogs in both their training and working roles is necessary (Stafford, 2006). The range of welfare issues that working dogs are subjected to is diverse, yet specific to their particular function and activity (Stafford, 2006). The requirements of these working dogs may subject them to various factors that contribute to an adverse impact on their overall wellbeing, for example, injury and stress. However, due to their selective breeding and training for specific roles, engaging in required duties reaps powerful positive reinforcement, therefore, for many of them, work is largely a pleasant experience (Stafford, 2006). Police and military working GSDs routinely undertake training and work of a similarly strenuous nature that indeed compromises their physical and psychological welfare, and their subsequent short working life might indicate poor welfare (Stafford, 2006).

While the expected operational life of a New Zealand Police GSD is eight years, this was reached by only 40% of dogs, with the average age of loss from active duty being substantially lower at 6.6 years. In accordance with New Zealand Police Dog Section (NZ PDS) policy, replacement dogs commence training one year prior to the current-serving dog reaching the planned retirement age (8 years) (Worth, 2014; Worth et al., 2013), which may be problematic when GSDs are lost from service sooner than anticipated. A recent study investigating reasons for loss of NZPDS GSDs from active service identified the primary cause of retirement, affecting 65% of GSDs, as a failure to cope with the physical requirements of the role (Worth, 2014; Worth et al., 2013). The underlying cause of this inability to perform physically for the majority (69%) of GSDs prematurely dismissed from service was degenerative musculoskeletal disease, of which 27% of cases were caused by back and spinal problems, with many of these likely involving the lumbo-sacral joint (Worth et al., 2013). Amongst active service NZ Police GSDs, the orthopaedic disease degenerative lumbo-sacral stenosis (DLSS) has been observed as one of the most prevalent spinal disorders of the lumbo-sacral spine, and the most important cause of loss from active service (Meij & Bergknut, 2010; Worth, 2014; Worth et al., 2013). DLSS is described as "a multifactorial degenerative disorder of the lumbo-sacral articulation, with ensuing *cauda equina* compression manifesting as debilitating pain" (Meij & Bergknut, 2010). With GSDs having the highest breed incidence of lumbo-sacral disc degeneration, it has been proposed that working GSDs are predisposed to DLSS due to a combination of abnormal anatomical characteristics and their specific work duties (Worth, 2014). The propensity for GSDs to encounter degeneration of the lumbo-sacral disc is reiterated across several studies. Swedish insurance data documented lumbo-sacral degenerative disease in GSDs as being the highest breed-specific risk encountered with 27.9 (± 2.4) claims per 10,000 dog years deemed at risk. This was also the leading cause for euthanasia in the breed with 18.1 (± 1.1) deaths per 10,000 dog years (Bergknut et al., 2012). In GSD serving as United States (US) military working dogs (MWDs), spinal cord disease (including lumbo-sacral disease) was classified as the second most likely cause of death or euthanasia, affecting 19% of all GSDs (Moore, Burkman, Carter, & Peterson, 2001). This was also the primary cause of discharge from service (34%) in US MWD GSDs five years or older (R. I. Evans, Herbold, Bradshaw, & Moore, 2007).

Selective breeding of the NZ Police GSDs appoints the most suitable genetic stock with superior phenotypes for reproduction to maximise the success of breeding and training programmes to reduce, for example, the incidence of hereditary conditions such as hip dysplasia. Further improving the genetic stock of breeding GSDs to select for dogs less prone to developing DLSS has been suggested to potentially mitigate DLSS-related losses. As transitional vertebral anomalies are known to predispose dogs to DLSS and are familial, this is a worthwhile consideration to include when selecting NZ Police GSD breeding stock (Morgan et al., 1993). Research efforts targeting indicators of DLSS are required to detect further heritable anatomical variations that contribute to diseases of the lumbo-sacral joint to optimise the conformation of the lumbo-sacral joint. Lowering the prevalence of DLSS in the working GSD population by increasing the prosperity of breeding programmes may improve the welfare of police dogs, and reduce the number of animals not fit for service requiring re-homing or euthanising. (Stafford, 2006; Worth, 2014).

Good working GSDs are extremely valuable animals, both in their capabilities within the NZ Police and the expense in refining them for their required duties. The investment in each dog prior to active service has breeding and initial training costs of approximately $25,000. Once in active service, each GSD requires an annual expenditure of $120,000 to remain operational. For financial reasons alone, reducing GSD loss and maximising longevity of duty is of significant importance for the NZ PDS (Stafford, 2006; Worth, 2014; Worth et al., 2013).

Resolution of painful debilitating conditions in GSDs can be achieved, whether for the continuation of work or for ease of suffering post-retirement. Of the NZ Police GSDs affected by DLSS that were examined at Massey University, procedures of both surgical decompression of the *cauda equina* and stabilisation of the lumbo-sacral articulation were achieved, successfully resolving the pain and disability associated with the condition (Worth, 2014; Worth et al., 2013). Further research is required around lumbo-sacral articulation to optimise treatment intervention options and reduce the anecdotal high failure rates of surgical implants in working dogs. Biomechanical testing is a viable option to investigate the efficiency of surgical intervention for working GSDs with DLSS by assessing potential strength and failure resistance of the adaptation prior to being applied clinically (Worth, 2014).

2.1.4 Welfare assessment and improvements for German shepherds

Compromise to NZ Police GSD welfare within the assessment domains is likely to occur within two of the four physical or functional domains of health and behaviour with sensory and neural inputs and are manifested in the affective experience domain where cognitive-neural inputs and activity related to external challenges are integrated before the final mental domain expression. Compromise of the health domain for NZ Police GSDs may occur in response to traumatic injury, disease agents or toxins, genetic disorders or other forms of functional impairment. The response experienced may include breathlessness, nausea, sickness, pain, distress, fear or anxiety. Behaviour compromise may occur in working GSDs, but particularly in ex-service GSDs, due to a general lack of productive occupation, stimulation and opportunity for performing actions with satisfying outcomes. Additional shortcomings could also include a lack of positive social interactions and substrates allowing the expression of behaviour patterns of foraging/hunting, play, and exploration (Mellor et al., 2009).

Ultimately, it is of great importance to identify both negative and positive factors across the five domains that influence animal welfare, as they contribute significantly to the subsequent length of the working life of GSDs. Greater research efforts are crucial in determining the contributing factors of welfare compromise, particularly regarding diseases common to the breed, such as degenerative musculoskeletal and lumbo-sacral disease, as well as the stress and distress experienced throughout working GSDs' range of duties. Only through increased knowledge and awareness may strategies be developed to mitigate loss and increase the longevity of GSDs in working roles and benefit the animals conscripted to service by increasing their health and wellbeing (Littlewood & Mellor, 2016; Mellor & Beausoleil, 2015; Mellor et al., 2009; Stafford, 2006; Worth, 2014; Worth et al., 2013).

2.2 Musculoskeletal modelling

2.2.1 Defining musculoskeletal modelling

Musculoskeletal modelling is a tool that offers insight into the biomechanics of the complex anatomical body and, as a study of biological systems from an engineering perspective, offers itself particularly well to the field of medicine (Aleotti, Caselli, Bracchi, & Gosi, 2008; Ignasiak, Dendorfer, & Ferguson, 2015). The general aim of this modelling is to enable the prediction of parameters such as muscle and joint reaction forces which are difficult or infeasible to measure due to the anatomical complexities of the musculoskeletal system (Brown, Kawcak, McIlwraith, & Pandy, 2003; de Zee, Hansen, Wong, Rasmussen, & Simonsen, 2007). As such, biomechanical modelling serves to represent the musculoskeletal structure as a series of individual bone segments mechanically linked through physiological joints within a system, and is capable of predicting intra-component contractile and compression forces generated by musculo-tendon actuators that cross the joints (Damsgaard, Rasmussen, Christensen, Surma, & de Zee, 2006; Dries et al., 2016; Ignasiak et al., 2015).

It follows then that thorough and true representation of muscle architecture is vital for meaningful biomechanical model outputs (Marra et al., 2015). Knowledge of muscle architecture also serves to provide greater insight into the structure-function relationship and allows for more realistic estimates of force magnitudes and distributions and, in turn, accurate joint contact forces to ultimately increase comprehension of joint injury aetiology (Brown et al., 2003). The bony segments in modelling are typically defined as rigid geometrical bone representations with an orthogonal and local coordinate system defined. With the skeletal and muscle elements of the model established, three-dimensional segmental motion and force plate data is input to enable inverse dynamics simulation for calculation of forces and moments acting upon joints (Dries et al., 2016). The resulting biomechanical analysis of the model provides insight into intrinsic muscle function and capacity and forces, as calculated through the output quantitative analysis values (Kura, Luo, Kitaoka, & An, 1997; Shahar & Banks-Sills, 2004).

Model capabilities of improving understanding of the internal and external influences affecting the musculoskeletal system would serve to enhance insight into orthopaedic conditions and predict their likely progression (Dries et al., 2016). Applications may include force analysis and predictions of force on the joints and cartilage and loading patterns of the musculoskeletal system. Additionally, this may act as a diagnostic tool to assist with clinical recommendations regarding implant and prosthesis integration for orthopaedic conditions, as well as assist in examining the pathomechanics behind the failure of bone integrity and articular injuries (Brown et al., 2003; Dries et al., 2016; Marra et al., 2015; Shahar & Banks-Sills, 2004).

These predictive capabilities of forces for computational modelling and biomechanical analysis of biological structures have shown their worth in providing quantitative and dynamic patient-specific information. This offers a depth of information that guides treatment choice through indication of optimal resolutions or anticipation of the outcomes of orthopaedic intervention. This technique overcomes the limitations of current practice recommending treatments through largely subjective, static, and qualitative evaluation (Marra et al., 2015). Furthermore, this tool is capable of offering detail on the mechanisms underlying injury from joint surface loading. Such loading is brought about by forces of muscle contraction, as well as ground-reaction forces experienced during both normal gait and more strenuous activities such as jumping and landing (Brown et al., 2003).

However, to achieve these beneficial outcomes, accurate muscle and joint force predictions require a very detailed and complete dataset including precise musculoskeletal geometry and architecture (Brown et al., 2003).

2.2.2 Musculoskeletal modelling strengths and limitations

Musculoskeletal modelling is commonly used as a tool to predict forces from model simulations in a non-invasive manner. The models fill the niche left exposed in obtaining datasets *in vivo* for biomechanical models. Musculoskeletal datasets compiled from living subjects are sparse due to the technical, biological and ethical concerns encountered. (Brown et al., 2003; Shahar & Banks-Sills, 2004; Shahar & Milgram, 2001). A key benefit of musculoskeletal modelling includes avoiding the difficulties in obtaining force measurements from the largely inaccessible deep regions of the spine (Arshad, Zander, Dreischarf, & Schmidt, 2016). Additionally, values of force transmitted across joints by muscles prove difficult to measure *in vivo* and so an indirect approach must be used to determine such forces and moments by solving the equations governing the equilibrium of a series of rigid bone segments connected by joints. (Shahar & Milgram, 2001).

While computer modelling is considered to enable reasonable estimations of forces, the process of constructing a musculo-skeletal model, testing, validating, and ultimately running simulations is a huge undertaking, and not without limitations (de Zee et al., 2007; Koblauch, 2015). The representation of a complex living organism through a model is naturally simplified (de Zee et al., 2007; Early, Mente, Dillard, & Roe, 2015). Limitations include the lack of knowledge around the influence of model input parameters, such as lumbar spine rhythm and intra-abdominal pressure, on the model outcome (Arshad et al., 2016)

Outputs from mathematically-based biomechanical models are validated through comparison to *in vivo* measurements that, when obtainable, are often arduous to collect. This is an inherently difficult task requiring experimental corroboration and it is paradoxical that this is also the partial reasoning for the development of the model (de Zee et al., 2007; Ignasiak et al., 2015; Shahar & Banks-Sills, 2004). This difficulty in proper validation has been reported by Marra et al. (2015) as being responsible for delaying the introduction of biomechanical modelling tools for use in clinical practice.

The quality of results obtained from model simulations is of course dependent on the accuracy of inputs, such as segment masses and moments of inertia, which can be experimentally determined (Christophy, Senan, Lotz, & O'Reilly, 2012). Accuracy of muscle parameters is maximised by more complex muscle models, such as the Hill-type model, which is capable of producing advanced muscle forces and activation patterns (Christophy et al., 2012).

The spinal column is a complex structure that protects the spinal cord, provides structural support, and enables mobility (Aleotti et al., 2008). Spinal models typically consist of a set of vertebral bone segments separated by discs and joints, connected by passive ligaments providing restraint, with movement controlled through muscle activation (Aleotti et al., 2008). However, assumption of even mass distribution and disregarded elastic couplings between segments is a limitation of spinal models (Ignasiak et al., 2015).

2.2.3 Canine musculoskeletal modelling

Application of musculoskeletal modelling to the canine lumbo-sacral spine has not been widely implemented, with the majority of efforts to date focusing on human spine modelling (Shahar & Milgram, 2001). While there is a significant contribution to kinematic analysis of canine extremities, biomechanical data for the canine spine is lacking (Aleotti et al., 2008). The pelvic limb has been a common focus of canine modelling, perhaps due to the large body of knowledge and ease of gathering the kinematic and force data necessary for inverse dynamics simulations. The clinical incidence of hip, stifle and tarsal joint injury is a likely contributing factor in this interest. Modelling of the canine pelvic limb to yield the magnitude and direction of joint reaction forces and muscle work requires accurate anatomic and morphometric data including segmental inertia and joint descriptions, as well as muscle contractile parameters and attachment sites (Shahar & Milgram, 2001).

Spinal motion is a complex process influenced by the three-dimensional conformation of the caudal spine and its many joints. This can be assessed through dynamic measurement *in vivo* or by artificially manipulating the motion segments ex vivo in a materials testing apparatus (Aleotti et al., 2008; Benninger et al., 2006). Patterns of three-dimensional motion in the canine lumbar spine are complex in their nature (Benninger et al., 2004) and are limited by ligaments and short muscles providing stability at the expense of contractile range.

Computer-assisted gait analysis also has diagnostic usefulness in identifying locomotor dysfunctions, however, this tool is not commonly used to analyse the spine. This is partly due to the difficulty of identifying the three-dimensional motion of spinal segments with surface markers (Wachs, Fischer, & Schilling, 2016). It follows that forces from the pelvic limb are found to be transmitted to the caudal spine, and it has been proposed that the lumbar and pelvic motions should therefore be viewed as a single functional unit when examining orthopaedic dysfunctions in dogs (Wachs et al., 2016). Investigations into spinal rhythm as a consequence or result of vertebral morphology are required as no known literature relates vertebra shape and corresponding intervertebral rotations (Arshad et al., 2016). There is unavoidable measurement error in data from the skin movement over the vertebra when measuring spine rhythms (Tafazzol, Arjmand, Shirazi-Adl, & Parnianpour, 2014) and so kinematic marker attachment to spinous processes would be required to accurately describe the true three-dimensional spinal motion patterns *in vivo*.

Sacroiliac joints are required to be rigid to facilitate high levels of force transmission experienced through propulsion from the pelvic limbs, muscular contraction, and to support the weight of the trunk. Additionally, however, this joint also plays a shock absorbing role to ground reaction forces, which requires flexibility. Forces transmitted up the pelvic limbs and through the pelvis, sacrum, and lumbo-sacral joints, are likely a contributing factor to articular injuries associated with the absorption of ground reaction forces. GSDs, which have prominent sagittally-aligned sacroiliac joints, are observed to experience higher shear forces (Brown et al., 2003; Saunders et al., 2013). Furthermore, instability and disease of the sacroiliac joint causing restricted motion is hypothesised to increase the forces experienced at other joints in the vicinity, such as the hip and lumbo-sacral joint (Saunders et al., 2013).

Working GSDs, particularly in police and military roles, are known to experience a number of problems associated with spinal column disease, with one of the most prominent effects being degenerative lumbosacral stenosis (Bergknut et al., 2012; Linn, Bartels, Rochat, Payton, & Moore, 2003; Meij & Bergknut, 2010; Worth, 2014). This multifactorial condition has suggested links of causation and development of disease to genetics, taxing physical activity, and external environmental variables; this requires further investigation to identify the causes of degeneration and provide effective treatment (Bergknut et al., 2012; Hediger et al., 2009; Linn et al., 2003)

The spine is subjected to a range of mechanical stresses, however, determining the physiological loading of the lumbar spine and lumbo-sacral joint is complex (Hediger et al., 2009). The GSD, and in particular male dogs, are overrepresented in their incidence of spinal disease, suggesting a genetic component being responsible, along with external factors of activity levels and environmental variables (Bergknut et al., 2012).

Biomechanical analysis of the forces acting on the lumbo-sacral area will improve understanding of the physiology of gait and the resulting mechanisms antagonised by high-intensity activity that contribute to injury and disease (Shahar & Milgram, 2001). Orthopaedic conditions are commonly a result of excessive forces acting upon the musculoskeletal system or forces acting in such a way that the spine is mal-equipped to withstand (Dries et al., 2016). For example, forces distributed in a non-physiological manner may be a contributing factor to spinal disorders and ligament ruptures (Dries et al., 2016). Modelling of these conditions would be an extremely valuable tool to predict the effect of further spinal degeneration on the biomechanical function (Schmidt, An, Lim, Nowicki, & Haughton, 1998).

There is a reported lack of biomechanical research on spinal modelling, but with the consistent increases in both technology and body of literature, investigations of musculoskeletal properties and subsequent development of biomechanical models is expected to progress. This would, in turn, encourage a cycle whereby the more models that are built, the greater the momentum gains in data collection necessary for model input will be, ultimately furthering this specific field of research (de Zee et al., 2007; Pintar, Yoganandan, Myers, Elhagediab, & Sances, 1992).

2.2.4 Human musculoskeletal modelling

While human and canine subjects possess markedly different postures with bipedal and quadrupedal locomotion, respectively, data might be shared between models of these two species, albeit with caution. In biomechanical studies of the lumbar spine, the interchangeable nature of select data between human and canine models is supported in some instances, including the contribution of ligaments and discs to stability of a spinal motion segment (Zimmerman et al., 1992).

As such, *in vitro* canine models have been used for assessment of surgical procedures and internal fixation devices for human lumbar spines (Lim, Goel, Weinstein, & Kong, 1994; Wilke, Wenger, & Claes, 1998). While possessing different postures, qualitative results showed stress distribution similarities with vertebral bodies transmitting the majority of the load in both canine and human spinal models (Lim et al., 1994). Human ligament data has also been used in canine research, with its use justified by speculated commonalities between mammalian ligaments (Shahar & Banks-Sills, 2004). Muscle data, however, is considered more difficult to transfer between species, with limitations arising from musculo-tendon differences, and the questionable accuracy of scaling factors (Dries et al., 2016).

Human lumbar spine musculoskeletal modelling and computer simulation has powerful applications in understanding lower back pain, and optimising clinical treatments and investigating the effects of surgical procedures such as spinal implants (Putzer, Ehrlich, Rasmussen, Gebbeken, & Dendorfer, 2015). Using such biomechanical modelling to study specific spinal kinetics could improve understanding of causation of spinal disorders hence improve prevention and treatment (Arshad et al., 2016; Ignasiak et al., 2015).

Interacting forces among hard and soft tissues and the environment controls movements and loads experienced in the lumbar spine. However, due to the complexity of the many morphological and mechanical elements associated with the spine, obtaining load measurements such as forces and moments in direct, yet non-invasive, techniques is not feasible (Arshad et al., 2016; Marra et al., 2015). The complexity of the epaxial muscles with their layered and multi-directional nature makes for extremely challenging acquisition of measurements, especially for the deeper and largely inaccessible muscles (Arshad et al., 2016).

The AnyBody Modeling System^{TM} (AMS) version 6.1 (AnyBody Technology A/S, Aalborg, Denmark) is a software platform capable of developing and analysing biomechanical models of musculoskeletal systems conducting various activities (de Zee et al., 2007). Inverse dynamics operations provide physics-based simulation of biological structures, and to date are primarily used to simulate human models. Accordingly, no further comparisons can be drawn with the preliminary canine model of this research.

3. MATERIALS AND METHODS

3.1 Introduction

This three-dimensional computer model of the canine lumbo-sacral spine was developed to fill a gap in the literature regarding simulation studies of the canine spine. The aim of this study was to develop an anatomically correct model capable of providing kinematic simulation and inverse dynamics feedback on environmental interactions, and subsequent forces acting on bone, soft tissue, and joints in any dynamic condition.

The canine spine model was designed using musculoskeletal modelling software around a single German shepherd dog cadaver, using medical images and dissection measurements. The model was developed from a collection of rigid spinal segments from Computed tomography (CT), oriented as observed in the cadaver. By attaching physiologically valid muscle vectors to anatomically correct points, a comprehensive subject-specific model incorporating musculoskeletal geometry and muscle-tendon architecture was produced. A single patient-specific canine model was crucial as a starting point to allow for scaling of medical imaging from subsequent live dogs to the original verified model, enabling its future application and relevance.

The German shepherd dog was selected for this biomechanical modelling and simulation study due to the significant incidence of degenerative musculoskeletal disease involving the lumbo-sacral joint in this breed (Worth et al., 2013). Future scaling of the model will be limited to German shepherd dogs due to the varied musculoskeletal conformations across canine breeds.

This study will also be beneficial as a precursor to an ensuing, more extensive canine study by developing and trialling preliminary data collection and modelling techniques. The more detailed model, including the rest of the spine, the ventral abdominal muscles and pelvic limbs would be capable of evaluating gait and environmental interaction forces experienced by the working dog. Ultimately, the aim is to have a full working model of the entire dog.

One of the challenges of the study concerns the quantitative aspects of data collection from the single, unpreserved canine cadaver available. The tissues degrade and so the time taken for meticulous muscle dissection precludes the assessment of deeper intervertebral ligaments. However, alternate generic data were sourced and valid scaling techniques incorporated to complete the dataset as best possible and achieve a functioning model. Methods for this study were based primarily on the TLEM (Horsman, Koopman, van der Helm, Prose, & Veeger, 2007) and TLEM 2.0 (Carbone et al., 2015) studies of the human lower extremities, which were implemented into the same three-dimensional modelling software as used in this study. These studies largely dictated the required input parameters, and how best to obtain the data to achieve a final working model.

3.2 Model development

3.2.1 Cadaver specimen

All data were collected from a single German shepherd dog cadaver (male, age and mass unknown). The dog was euthanised for reasons other than musculoskeletal disease. The primary area of interest of the intact specimen was the lumbo-sacral spine region, namely the sacrum, sacroiliac joints and caudal lumbar vertebrae L4 to L7, along with all connected muscles, tendons and ligaments.

3.2.2 Medical imaging

Computed tomography (CT) of the intact specimen was acquired by Massey University Radiology Department. Imaging was inclusive of the fourth lumbar vertebra through to the sacrum, and captured the dorsal section of the pelvis including the sacroiliac joints. A Phillips Brilliance 16-slice helical scanner (Phillips Healthcare, The Netherlands) was used for the CT, with a voxel size 0.8 mm X 0.8 mm X 0.8 mm, a 1 mm slice thickness, and a 0.5 mm overlay. All CT imaging was performed on the pelvis and lumbo-sacral spine of the intact canine cadaver (Figure 3.1). Following the collection of the CT images, the trunk was sectioned in the transverse plane at the L7 vertebra and the hind limbs were removed, leaving the L7 vertebra attached to the pelvis.

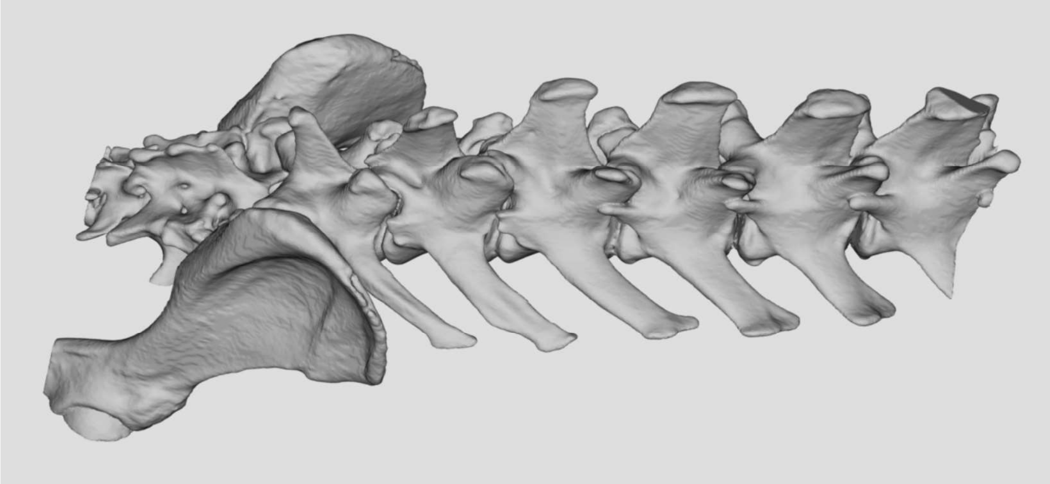

Figure 3.1. CT image of the intact GSD specimen.

On completion of the soft tissue dissection, bone segments were separated and all soft tissue was macerated by immersion in moderately heated water over 72 hours, and then removed by scalpel, leaving only clean bone segments remaining. Further CT images were subsequently acquired of the separate lumbar sections, sacrum and pelvis (Figure 3.2) to accurately capture individual bone geometries, particularly of the articulating surfaces of the sacroiliac joint.

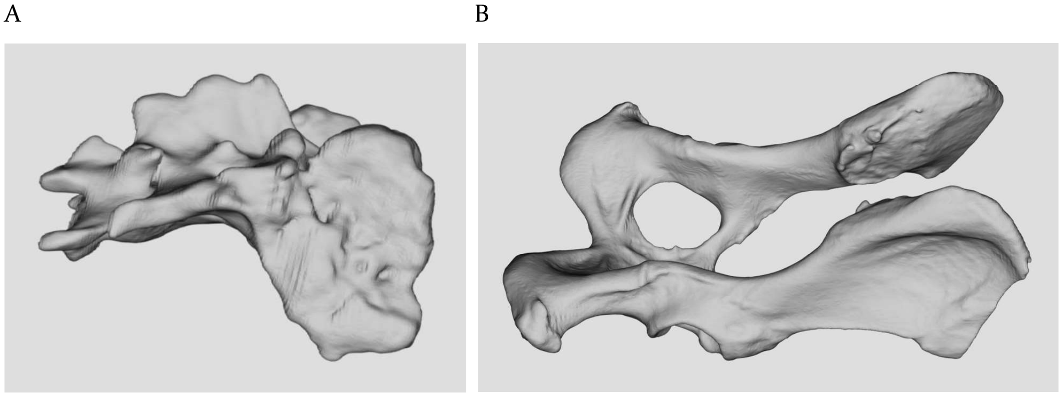

Figure 3.2. Individual CT images of GSD sacrum (A) and pelvis (B).

3.2.3 Cadaver measurements

The frozen sectioned specimen, consisting of the pelvis, sacrum, and partial seventh lumbar vertebra, was stored for approximately 2.5 years prior to being used in this study. The specimen was submerged in water and thawed in a refrigerator for 48 hours prior to a careful and complete dissection of all muscles and tendons in the lumbo-sacral region. Skin, superficial and deep fascia, and subcutaneous fat was removed prior to the full dissection commencing (Figure 3.3).

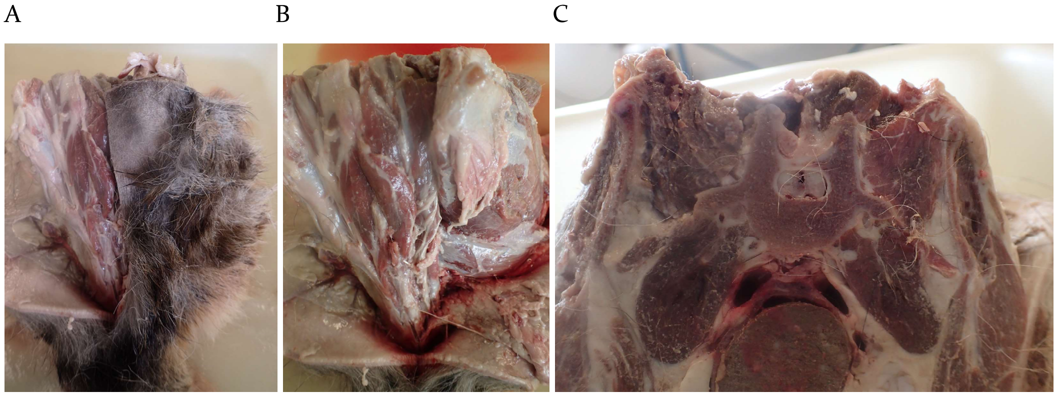

Figure 3.3. General images of GSD specimen at the start of the dissection from dorsal (A,B) and cranial (C) aspects.

Throughout the dissection, the Qualisys motion capture camera system (Qualisys Medical AB, Partille, Sweden) was used to measure the position of muscle-tendon origins and insertions in three-dimensional space, allocating X, Y, and Z coordinates to each point. The camera system had a spatial accuracy of 0.2 mm. The volume of space assessed by the Qualisys camera system was calibrated using a Qualisys calibration frame and wand to establish an anatomical reference frame. Five reflective pins were then fixed on anatomical positions for use as reference markers on the specimen. All captured coordinates were recorded with respect to the five reference markers (Figure 3.4), ultimately expressing all coordinate data in relation to the established anatomical reference frame (Horsman et al., 2007). The position of the pins were as follows: three pins were inserted into the transverse cut through the seventh lumbar vertebra marking the cranial plane of the specimen, one in the median plane of the body, and two in the base of the left and right transverse processes. The remaining two pins were inserted along the caudal midline; in the caudodorsal point of the median sacral crest, and the spinous process of the first caudal vertebra.

The established anatomical reference frame allowed for measurements to be obtained between soft tissue points of interest using temporary reflective marker pins. Coordinate data were captured primarily to compare the attachment points of muscles against those described in the literature (H. E. Evans & de Lahunta, 2013).

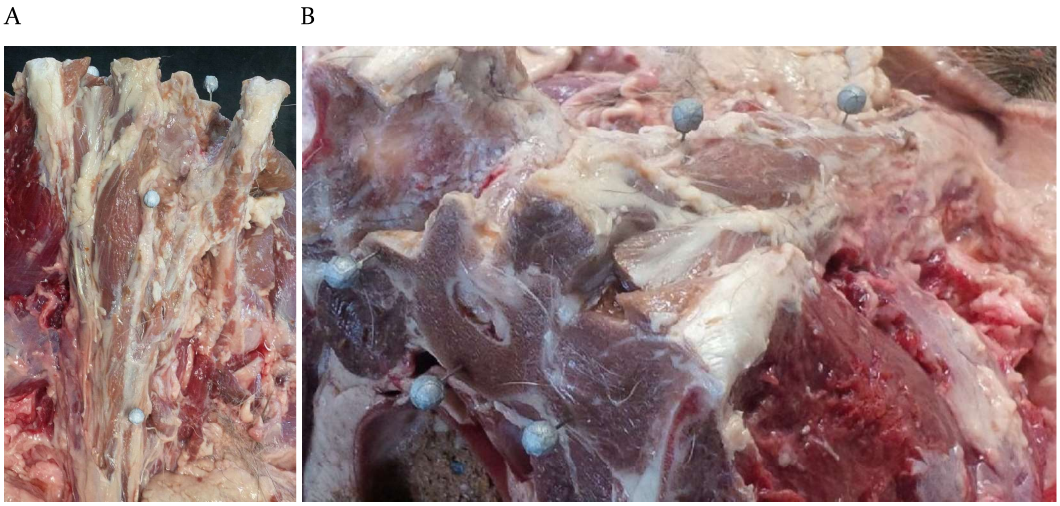

Figure 3.4. Fixed Qualisys pins to define reference frame for specimen dissection.

3.2.3.1 Muscle geometrical parameters and morphometric data

Each muscle was isolated from surrounding intermuscular connective tissue (Figure 3.5) and identified with reference to a canine anatomical textbook (H. E. Evans & de Lahunta, 2013). Muscle belly length and slack tendon lengths, the sum of which equalled the total muscle-tendon element length (Klein Breteler, Spoor, & Van der Helm, 1999), were measured using a non-stretch nylon string whilst the muscle remained attached. The string length was then measured against a ruler (± 0.05 cm). The lengths of several representative muscle fibres were measured for each muscle element, with the exact number being dependent on the size of the muscle element.

In the instance of the muscle being asymmetrical in gross appearance with variability of muscle fibre lengths, or if the tendon possessed dissimilar overlap lengths across the muscle, singular length values were estimated from an average of the irregular measured values.

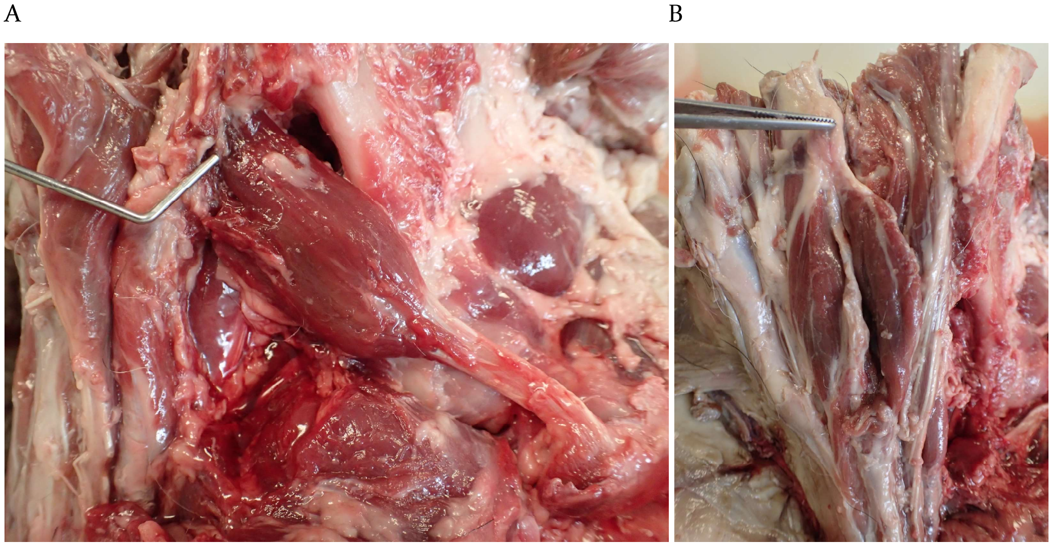

Figure 3.5. Specimen during dissection with piriformis (A) and sacrocaudalis dorsalis medialis (B) muscles indicated.

Pennation angle, which described the orientation of muscle fibres relative to its line of action, was defined as the angle formed between the direction of the muscle fibre bundles (fascicles) and the line connecting the muscle's origin and insertion (Sharir, Milgram, & Shahar, 2006). This was measured in one dimension by establishing two string lines and measuring the difference in angle at their intersection with a protractor. Measurement precision was ± 2°. The first string line followed the course of the muscle fascicles, and was measured in three portions (distal, middle, and proximal) of the muscle. If fascicle direction appeared varied across the muscle, further measurements were sampled at multiple sites from various regions within the muscle. Intersecting the fascicle string line was the second string line, which ran between singular origin and insertion points and represented the muscle line-of-action.

A single pennation angle was recorded for each muscle, calculated as an average angle determined by calculating an arithmetic mean from all measured angles (Sacks & Roy, 1982; Sharir et al., 2006). The angle of pennation was only deemed significant and utilised for PCSA calculation if in excess of 20 degrees; hence lesser angles were disregarded (Shahar & Milgram, 2001; Sharir et al., 2006).

Using the Qualisys camera system and established anatomical reference frame, coordinates were obtained from the temporary reflective marker positions to capture the following points of interest: muscle-tendon element length, muscle line of action, muscle fibre direction, and muscle origin and insertion attachment site areas (Figure 3.6). The attachment sites were the last coordinates to be obtained, being recorded immediately after excision of the individual muscles. The entire attachment site area was recorded with coordinates describing the perimeter of the attachment sites. The size and shape of each muscle attachment site dictated how many measured points were necessary to accurately represent the site, as described in para 3.2.4.7 (Pellikaan et al., 2014).

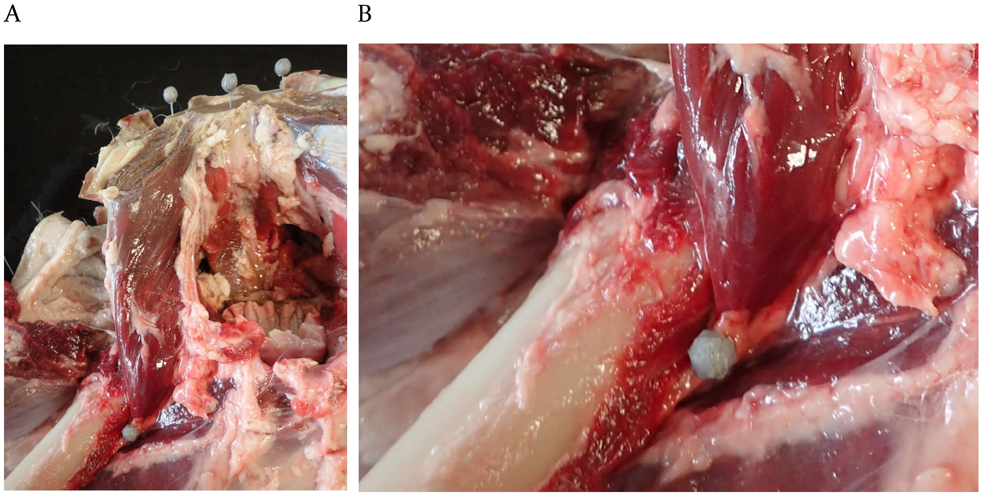

Figure 3.6. Qualisys camera system temporary marker indicating the iliopsoas muscle attachment site

Tendon, fat and excessive connective tissue were removed from the muscle prior to weighing using an electronic scale with a 0.01 g accuracy. Muscle volume was measured by the water dislocation method, using a scaled cylinder with an accuracy of 0.1 mL.

A small biopsy was taken from each muscle for microscopic examination of sarcomere length, as necessary for subsequent muscle parameter calculations. Each representative biopsy was taken from a site central and deep to the muscle belly, measured approximately 20 mm long by 10 mm wide, and was submerged immediately in 10% formalin where it remained for 48 hours. Alteration of muscle size across all muscle samples, hence filament lengths, due to the fixation and excision process was deemed to be negligible and insignificantly altered, with less than 5% shrinkage or elongation across all muscle biopsy samples (Klein Breteler et al., 1999; Sacks & Roy, 1982). This enabled the post-fixation lengths to be used with confidence in calculations.

Smaller samples of approximately 5 mm in length and width were taken from the centre of the fixed muscle biopsy, with care taken to ensure that these final samples possessed no visible tissue damage. The Massey University Histology Lab carried out all subsequent work in preparing the tissue biopsies for viewing under a microscope. This tissue processing included the following stages: embedded in wax, sectioned longitudinally (parallel to the muscle fibres), mounted to a glass slide, cover-slipped using glycerol, de-waxed, and remained unstained ready for microscopic evaluation.

The mounted samples were observed under a light microscope (Ziess Axiophot) at 400x magnification with a 100x oil-immersion objective for inspection of sarcomere length (Sharir et al., 2006; Young, Papa, Lyon, George, & Miller, 1990). Sarcomeres were defined as the repeating subunits of a myofibril (the cylindrical bundles of contractile proteins) within a skeletal muscle fibre or myofibre, arranged in bundles or fascicles spanning the entire length of the muscle (King, Reiss, & Roberts, 2001). The regions of interest regarding sarcomere length were the striations of alternating light and dark bands running across the myofibril, and in particular, the Z- lines running through the middle of the light bands (Figure 3.7). Measuring the distance between adjacent Z-lines was a considered a reliable method of accurately defining the length of a sarcomere (King et al., 2001).

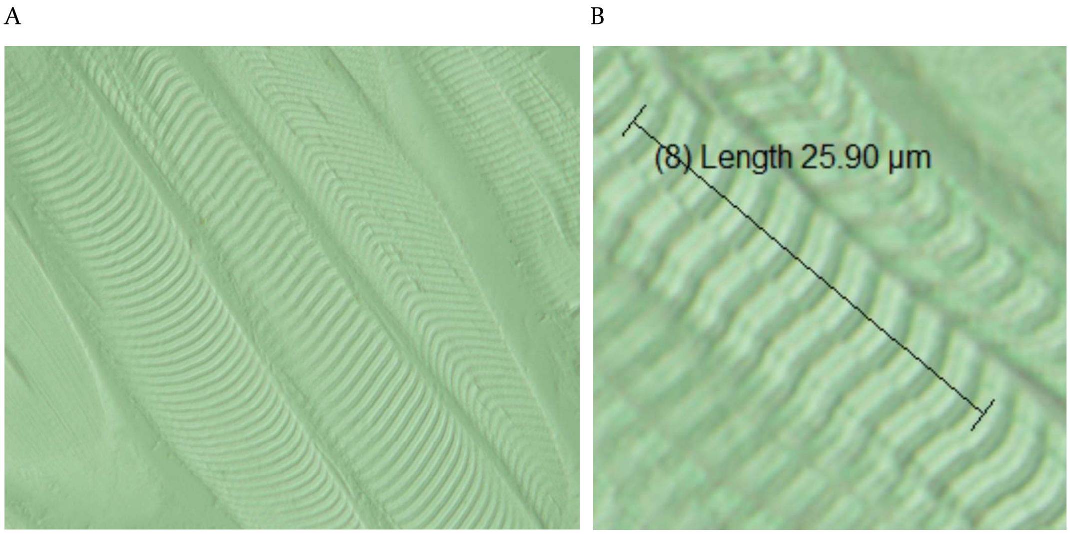

Figure 3.7. Microscopic image showing myofibril bands (A) and length of ten sarcomeres and z-lines (B).

Nominal sarcomere length, required for determining optimal fibre length, was measured by evaluating the Euclidean distance between successive Z-lines under the microscope, and capturing a clear image of the multiple fibres and sarcomeres (Horsman et al., 2007; Infantolino, Ellis, & Challis, 2010; Young et al., 1990). The resulting high-resolution image was captured with, and processed by, an image capture system (Olympus DP70: Cellsens dimensions) capable of gathering sarcomere measurements. The inbuilt and calibrated scale of the imaging software, allowed for all lengths to be measured accurately and recorded as the true value observed under the light microscope.

Blocks of 10 adjacent sarcomeres were measured and their mean section length recorded. This measurement was repeated across 10 random and representative locations spanning the fibres of each muscle sample. Nominal sarcomere length for the muscle was calculated from the average of these 100 observed sarcomere lengths (10 representative measures of 10x adjacent sarcomere sections) (Infantolino et al., 2010; Sacks & Roy, 1982; Sharir et al., 2006).

Any sarcomere lengths deemed abnormally small were not measured, as this was likely a result of muscle fibres breaking during rigor mortis (Klein Breteler et al., 1999). One sample biopsy per muscle was deemed sufficient as attested to in (Sacks & Roy, 1982), whereby nominal sarcomere lengths from different regions within a single muscle were shown to differ by less than 5%.

As cadaver position affects muscle position and, therefore, nominal sarcomere length, the neutral position of the specimen in this study was deemed suitable for collection of accurate nominal sarcomere lengths. These measurements were comparable across different muscles as each muscle was in a neutral position, rather than stretched which would inflict consequential lengthening of the nominal sarcomere measurements (Sacks & Roy, 1982).

3.2.3.2 Ligament Parameters

Attachment sites and lines-of-action of all ligaments in vicinity of the lumbo-sacral joint were estimated from the literature (H. E. Evans & de Lahunta, 2013). All ligaments were deemed to run in a straight line between their origin and insertion (Horsman et al., 2007).

3.2.3.3 Joint Geometry

Three-dimensional spinal range of motion limits of German shepherd dogs from the fourth lumbar vertebrae to the sacrum were taken from the literature (Meij, Suwankong, Van der Veen, & Hazewinkel, 2007; Saunders et al., 2013; Schmidt et al., 1998). The range of motion in each plane was described across 3 rotational axes with movement around the longitudinal axis (axial rotation), sagittal plane (flexion and extension), and lateral plane (abduction and adduction).

3.2.3.4 Prominent Bony Landmarks

All ligaments and soft tissue were removed from the specimen prior to separating the partial seventh lumbar vertebrae, sacrum, and pelvis. Prominent bony landmarks, needed for definition of the global coordinate frame (Klein Breteler et al., 1999), were measured on the bone surfaces in relation to the established anatomical reference frame during the dissection of the specimen. The fixed markers identifying the bony landmarks were captured alongside each temporary marker pin so as to provide a set reference to compare all points of interest against.

3.2.4 Post-processing

3.2.4.1 Medical image post-processing

All image post-processing was conducted in the Philips Extended Brilliance Workspace (EBW) (version 4.5.5.51035) with the aim of obtaining optimal quality images. Processing was conducted on the DICOM file 'soft thins neutral' CT scans, which possessed high quality surface rendering. Initially, the bone image quality was optimised via window level and width adjustment settings. These fine adjustments assisted in the model's accuracy to the specimen and valid centre of mass calculations, as well as to ensure an aesthetically pleasing final model.

Slice-by-slice tissue segmentation was then conducted independently across 3 planes to clean up the bone segments. This involved the removal of hard and soft tissue attached to, and in the vicinity of, the hard tissue segment of interest to isolate the singular bone segment from all adjacent tissues. The resulting individual bone segments selected for use in the final model consisted of the pelvis and sacrum from the individual bone CT files, and lumbar vertebrae four through to seven extracted and cleaned up from the initial CT scan of the intact canine specimen.

The pelvis and sacrum bone segments required minimal adjustments and possessed optimum detail in the articular surfaces due to their independent CT scans. Lumbar vertebrae four through to seven were more labour intensive in eliminating the unwanted surrounding tissue, with facet joint articular surfaces requiring the most detailed and thorough attention. Lastly, the bone segment was exported as an .stl file, so as to be readable by third party software for subsequent post-processing requirements.

3.2.4.2 Transformation and Registration

The individual bone segments of the pelvis and sacrum were registered to the intact whole bone segment from the initial CT scan within the mechanical modelling software AnyBody Modeling System^{TM} (AMS) version 6.1 (AnyBody Technology A/S, Aalborg, Denmark). Transformation was achieved using an affine matrix from which the vector of translation and the matrix of linear transformation were extracted, and inserted into each segment in AnyBody as the r0 and Axes0, respectively. The affine class of transformation was selected from the available mathematical classes of computer graphics due to its combination of the linear transformation and translation functions, and the preservation of collinearity and ratios of distance. The matrix of affine transformation of each rigid bone segment in three-dimensions was determined based on the coordinates of two sets of landmarks, each with a minimum of four points, and constructed in the AnyBody Modelling System using the AnyFunTransform3DLin2 class.

Registration of the individual bone segments to the original intact bones was accomplished for the sacrum and pelvis by first acquiring identical landmarks from both the individual and intact bone, as described in para 3.2.4.3. The translation vector and rotation matrix extracted from the affine transformation matrix were then used to arrange each individual bone segment in its true neutral anatomical position and orientation to construct the skeletal element of the model. This correct alignment also enabled a more effective resolution of the AnyBody kinematic analysis solver when running the InitialConditions operation.

This method of registration was used to align the reference frame orientation of joint nodes to the AnyBody global reference frame. Transformation of the pelvis and sacrum joint node coordinates was also required as the nodes were obtained from the SolidWorks individual bone segment .stl files, as described in para 3.2.4.9, then transformed to the global reference frame of the intact bone .stl file. The joint node coordinates underwent their final transformation to the local coordinate system of each segment in the AnyBody Modelling System.

3.2.4.3 Prominent Bony Landmarks

The prominent bony landmarks identified in the anatomical reference frame were not applicable to the primary local and global reference frames, as described in para 3.2.4.4 and 3.2.4.5, respectively. This was due to various reasons regarding accessibility of bone surfaces on the specimen as discussed in detail in para 5.2.3.

Prominent bony landmarks were instead selected on singular bone segment .stl files, which were created from the CT medical imaging (Figure 3.8). This selection was obtained using SolidWorks version 2015 (Dassault Systèmes S.A., Vélizy-Villacoublay, France), a solid modelling computer-aided design and computer-aided engineering computer program. Prominent bony landmarks were selected on the basis of their ease of identification in radiographs in accordance with (Shahar & Milgram, 2001), which will be crucial in determining muscle attachment sites from anthropometric scaling of subsequent dogs in the future.

The bony landmarks for the pelvis and sacrum bone segments were observed as follows:

Sacrum: The median sacral crest caudodorsal process, the caudodorsal tips of the left and right lateral sacral crests, and the dorsal cranial tips of the left and right sacral wings.

Pelvis: The left and right cranial dorsal iliac spines, and left and right caudal dorsal iliac spines.

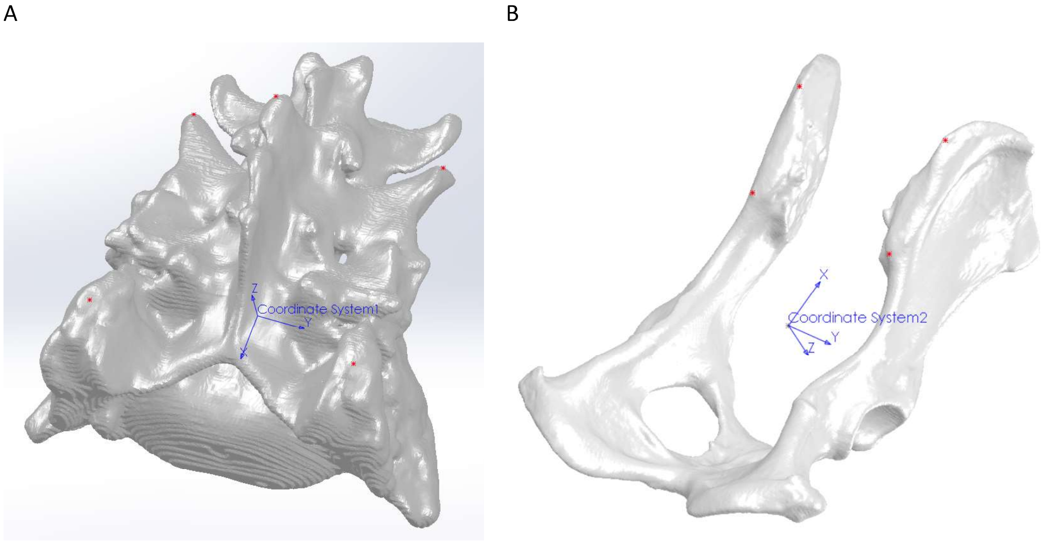

Figure 3.8. Bony landmarks of sacrum (A) and pelvis (B) as captured in SolidWorks.

The lumbar vertebrae bony segment medical images were acquired from the original CT scan of the intact specimen for later processing. As their position was already correctly oriented, they did not require prominent bony landmarks to be captured for realignment.

3.2.4.4 Local reference frames

The six individual and cleaned bone segments (pelvis, sacrum, and 4 lumbar vertebrae) .stl files were imported into SolidWorks for the creation of a local coordinate system per bony segment. An orthogonal coordinate system was applied to each bone's local origin, with X, Y, and Z axes coinciding with the anatomical directions of cranial-caudal, medial-lateral, and ventral-dorsal, respectively (Shahar & Milgram, 2001). The origin of each local reference was positioned at the bone's centre of mass, calculated from the .stl file of each bone in SolidWorks using a uniform bone density of 1400 kg/m^3 (Pressel et al., 2005).

Local anatomical reference frames and origins (O) were defined for the pelvis, sacrum and lumbar vertebrae, with the X-, Y-, and Z-axis orientated perpendicular to one another:

- Sacrum
  O: sacrum centre of mass, located approximately at the intersection between the midline, the dorsal edge of the base, and mid wing in line with the cranial intermedial sacral crest.
  Z: the line parallel to a line connecting the left and right lateral sacral crests, pointing laterally towards the right portion

X: the median line running along the median sacral crest, pointing cranially
Y: the line pointing dorsally, perpendicular to the Z- and X- axis

- Lumbar Vertebrae
  O: sacrum centre of mass, located approximately on the midline, at the midpoint of the vertebral foramen.
  Z: the line parallel to a line connecting the left and right caudal articular processes, pointing laterally towards the right portion
  X: the median line running with the spinous process, pointing cranially
  Y: the line pointing dorsally, perpendicular to the Z- and X- axis
- Pelvis
  O: Pelvis centre of mass, located approximately at the intersection between the midline, equidistant between the left and right ilium bodies, and the dorsal level of the left and right greater ischiatic notches.
  Z: the line parallel to a line connecting the left and right left and right cranial dorsal iliac spines, pointing laterally towards the right portion
  X: the median line, equidistant from the left and right cranial dorsal iliac spines, pointing cranially
  Y: the line pointing dorsally, perpendicular to the Z- and X- axis

3.2.4.5 Global reference frames

The global reference frame is required to give each bony motion segment a frame of reference for three-dimensional motion against its neighbouring segments. To establish this global coordinate system in SolidWorks, four prominent bony landmarks were acquired on each of the six individual bone segments, and these identical landmarks were also identified on the original and intact canine specimen. All landmarks had X, Y, and Z coordinates captured and nodes assigned to the position. Landmark nodes from the local reference frame of each segment were then transformed into the position of nodes on the entire CT scan, in the new global reference frame. Thus, all individual bony segments were realigned to their true anatomical position as seen in the original CT scan of the entire canine specimen.

With bone segments reassembled in their correct natural alignment and position relative to one another (Figure 3.9), and all local coordinates transformed into a single global coordinate system, this allowed for interactions and subsequent measurements of muscle-tendon elements and ligament lengths between nodes on different bone segments in the global reference frame. This also enabled each bone segment to move in three-dimensions independent of its neighbouring segments.

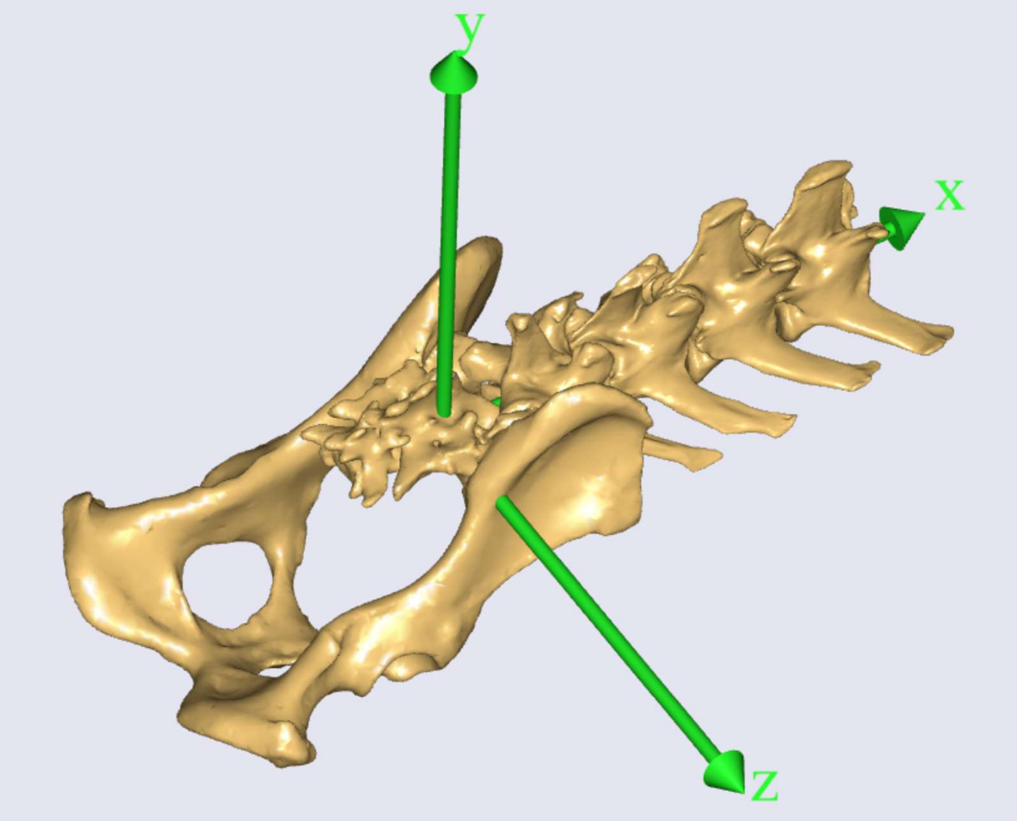

Figure 3.9. Canine pelvis, sacrum and partial lumbar spine skeletal elements realigned in the AnyBody Modeling System.

The global reference frame and origin (O) were defined for the entire model, comprised of the pelvis, sacrum and four lumbar vertebrae, with the X-, Y-, and Z-axis orientated perpendicular to one another:

- O: Internal to the sacrum on the intersection of the midline, the sacrum base, and the caudodorsal point of the cranial most process of the sacrum medial crest.
  Z: the line parallel to a line connecting the left and right lateral sacral crests, pointing laterally towards the right portion
  (+Z = right, -Z = left)
  X: the median line running along the median sacral crest, pointing cranially (+X = cranial, -X = caudal)
  Y: the line pointing dorsally, perpendicular to the Z- and X- axis (+Y = dorsal, -Y = ventral)

3.2.4.6 Inertial Parameters

Inertial parameters are typically an integral part of biomechanical models, taking into account segment mass and the accelerations around the principal axes. The importance of these parameters lies in their ability to dictate the segment's resistance to change in angular velocity and also, to determine how the segments will react to forces and the resulting moments applied on them (Dries et al., 2016). However, the angular accelerations normally applied to the spinal elements of the musculoskeletal system are small, and as such are not critically important in the model.

Anthropometric measurements for estimation of inertial parameters as seen in (Carbone et al., 2015) include: segment mass, centre of mass, principal axis of inertia and principal moment of inertia. These parameters were calculated based on segmented bone volumes from CT imaging.

Inertial values in this study are calculated from a uniform bone density of 1400 kg/m^3 (Pressel et al., 2005) and bone mass in SolidWorks, thus are deemed lower estimations than probable due to the lack of total muscle and fat volumes in the vicinity of the bony segment, typically provided by magnetic resonance imaging (MRI) data.

However, the inertial properties of the lumbar spine and pelvis area of this canine model are considered too low to bear any significant impact on the model's motion. This conclusion was drawn acknowledging the required presence of large accelerations to show any influence on inertia and motion. As spinal acceleration in gait is of a high frequency and transient in nature, the vertebral angular acceleration experienced in locomotion is short-lived and noisy, hence filtered out. This filtering, coupled with the absence of any necessary angular acceleration, does not support spinal inertia as a relevant variable. The expected inertia in the canine spine is, for the most part, virtually zero, therefore, the inertial estimates based on the centre of mass and uniform bone density inputs in SolidWorks are considered adequate.

The current estimate in the model is motivated by the difficulty in distributing contributions of the surrounding abdominal masses to the inertial moments, along with the unlikelihood of any significant velocities and accelerations across the bony segments of this canine model (de Zee et al., 2007). It is, therefore, more appropriate to assume the lower inertial influence in this study and fulfil the inertial parameters, rather than leave a gap in the dataset.

3.2.4.7 Modelling of muscle parameters

Muscle attachment sites were acquired in the local reference frame of each bony segment, with reference to the literature (H. E. Evans & de Lahunta, 2013), by creating nodes on the .stl file in SolidWorks. These node coordinates were utilised to map the perimeter of the muscle-tendon element attachments to the bone, prior to separating the muscle into representative elements.

The representation of each muscle by elements, was referenced heavily from (Van Der Helm & Veenbaas, 1991), and was applied as follows:

Muscle-tendon actuators were divided into a number of representative muscle-tendon elements, utilising a minimal number of force vectors, so as to accurately describe the mechanical effect of the muscle. The number of force vectors required to accurately represent the muscle element's line of action was dependent on the muscle architecture, and the shape and size of the attachment site. The force vectors were depicted as elements with singular origin and insertion attachment site nodes. All muscles were comprised of these elements, with attachment sites comprising of between one and six nodes. The maximal number of six nodes, was identified as the minimum number of element force vectors deemed capable of sufficiently representing a muscle with a large surface attachment area, while keeping the resulting error in the mechanical effect negligible.

The number of elements representing the muscle was ultimately dependent on the number of degrees of freedom the muscle could independently influence, with the number of elements corresponding directly to the number of independent equations describing the effect of the muscle at its insertion on the bone.

Each muscle was divided into the appropriate number of muscle elements, with muscle attachment site contours approximated and modelled as various shapes and described by (Pellikaan et al., 2014) with reference to (Van Der Helm & Veenbaas, 1991) and (Van Der Helm, Veeger, Pronk, Van Der Woude, & Rozendal, 1992) as follows:

- Point: Calculated as the mean of the measured muscle attachment coordinates on the bone. The error was defined as the mean distance of the measured coordinates to the calculated coordinate of the muscle element attachment site.
- Line (straight or curved): A three-dimensional polynomial for the x-, y-, and z-coordinates was fitted to the measured coordinates. The resulting attachment sites of the muscle elements were proportionally distributed along the polynomial. For a first order polynomial at least two attachment sites, and for a higher order polynomial at least three attachment sites were defined. The error of the three-dimensional polynomial fit was defined as the mean distance of the data points to the polynomial.

- Surface: The measured coordinates were defined as and projected onto a plane. The circumference of the projected coordinates could define an area, and were divided into three equal parts. In each of the parts, two elements were proportionally distributed over the area resulting in six points describing the surface. The error was the mean distance of the measured coordinates to the optimised plane.

As above, representative muscle origin and insertion sites were defined, in order of increasing complexity, as a point, straight line, curved line, or surface attachment. The nature of the true attachment site areas, and ensuing representation, dictated the number of nodes, hence elements, required to accurately represent the muscle and its mechanical effect. The number of nodes corresponding to the varied representations of attachment sites was as follows: point sites had only one element node, straight line had two element nodes, and both curved-line and surface sites had at least three element nodes. The complexity of the muscle attachment sites and number of nodes allocated per site was the determining factor as to how many representative muscle elements the muscle was subdivided into.

The attachment sites of muscles were modelled in the following representations:

- Point: Muscles with a relatively small attachment area were considered single units exerting force along the line between origin and insertion (Sharir et al., 2006), and subsequently were approximated by one central node.
- Line: An area with a length relatively large in comparison to its width was approximated by a straight or curved line. Two and three or more nodes represented first order polynomials (straight lines) and higher order polynomials (curved lines), respectively (Horsman et al., 2007).
- Surface: A large area was approximated by a surface, represented by between three and six nodes.

Muscle attachment sites captured with the Qualisys camera system during the dissection were attempted to be validated with known canine muscle insertion points from the literature (H. E. Evans & de Lahunta, 2013). However, as the prominent bony landmarks from the anatomical reference frame did not marry up with those from the SolidWorks local reference frame, and the specimen for dissection lacked complete lumbar vertebrae caudal to the sacrum, the muscle attachment sites from the specimen dissection were unable to be translated outside of their original anatomical reference frame. These issues were rectified by ensuring the final nodes representing muscle attachment sites were acquired on individual bones in the local reference frame in SolidWorks, obtained exclusively by referencing the anatomy text. Lastly, all node coordinates were transformed into the AnyBody local coordinate reference frame to obtain the necessary musculo-tendon measurements (Figure 3.10).

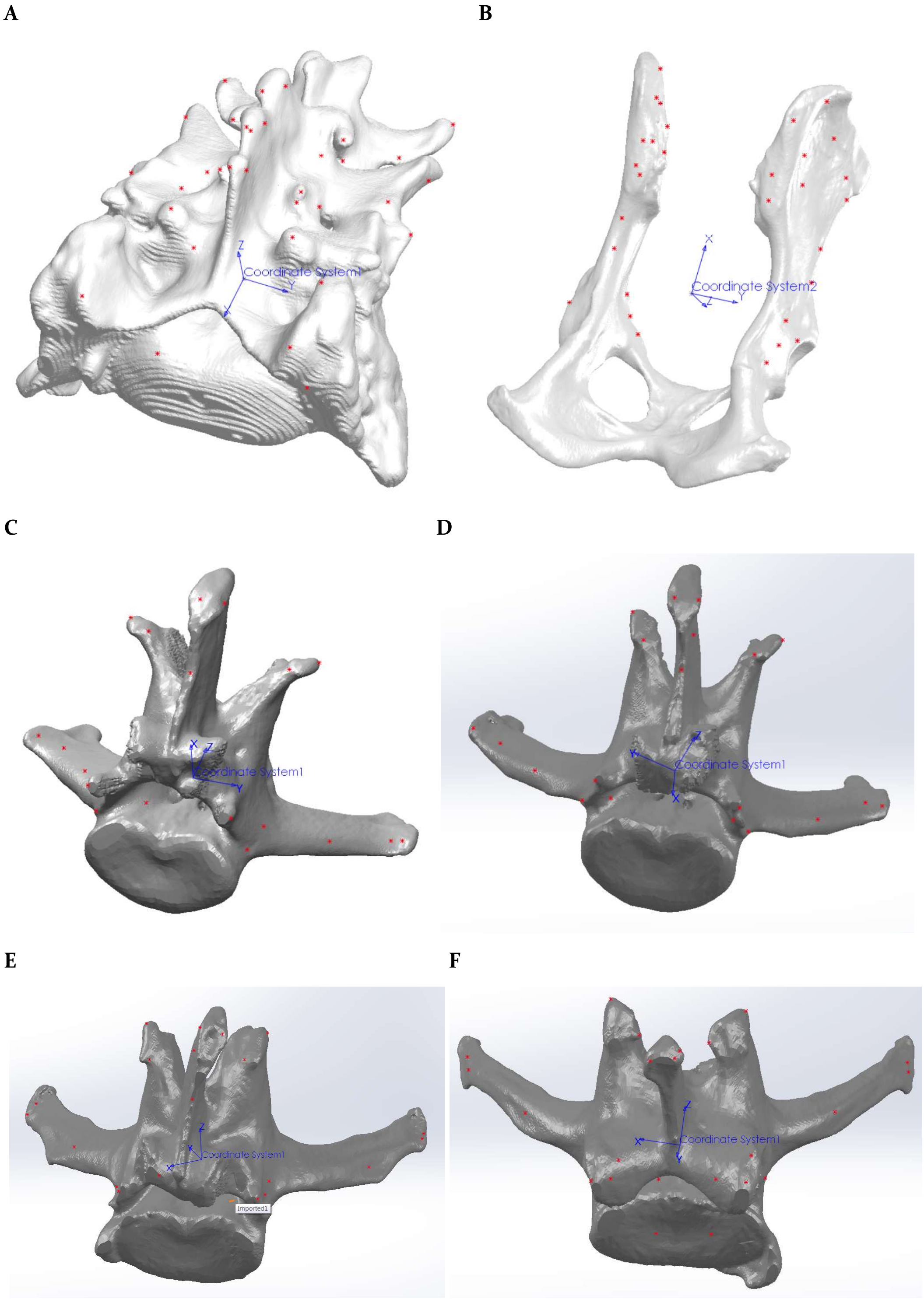

Figure 3.10. SolidWorks muscle nodes of the sacrum (A), pelvis (B) and lumbar vertebrae L4-7 (C-F).

Muscle morphometry data collection for calculation of muscle input parameters required multiple datasets and calculations for the input parameters imperative to the final three-dimensional complex muscle model. The input three calculated input parameters for the complex muscle model were nominal tendon length, nominal fibre length, and the physiological cross-sectional area (PCSA).

The two lengths were calculated as follows:

1) Muscle-tendon element length was obtained by determining the three-dimensional distance between the origin (o) and insertion (i) node coordinates.

$$\text{MT length} = (d) = \surd\ (x_i - x_o)^2 + (y_i - y_o)^2 + (z_i - z_o)^2$$

With a single time step at the zero moment in the AnyBody Modelling System, i.e. the neutral position of the model as captured by CT medical imaging of the intact specimen, muscle lengths were captured using the predefined linear measure. A vector variable, namely a linear measure from the origin to insertion points, was defined for every muscle element. The length of this vector described the length between the coordinates, hence the muscle-tendon element length.

2) Muscle fibre length, or nominal fibre length, represented the length of the muscle and was calculated by subtracting the nominal tendon length, measured in the dissection, from the muscle-tendon element length (Klein Breteler et al., 1999).

The last remaining parameter to be calculated, muscle PCSA, represented the ratio of muscle volume to effective/optimal muscle fibre (fascicle) length (Horsman et al., 2007). This reflected the number of sarcomeres in parallel in a muscle, and is therefore proportional to the amount of force the muscle is capable of exerting (Shahar & Milgram, 2001; Sharir et al., 2006).

PCSA is typically calculated as $(m * \cos \alpha)/(l * \rho)$, where m is the muscle mass (g), α is the nominal pennation angle (°), l is the nominal fibre length (cm), and ρ is the uniform canine muscle tissue density assumed (1.059 g/cm^3) (Shahar & Milgram, 2001). However, since no significant pennation angles (in excess of 20 degrees) were recorded in this study, the PCSA was alternately calculated, excluding pennation angle, as:

$$\begin{aligned} \text{PCSA} &= (m / \rho) / \text{LF}_{\text{opt}} \\ &= vol / \text{LF}_{\text{opt}} \end{aligned}$$

Muscle mass was divided by the specific canine muscle tissue density, resulting in *vol*, the muscle volume (cm^3), which was subsequently divided by the LF_{opt}, the optimum muscle fibre length of that muscle (Klein Breteler et al., 1999). PCSA that could not be calculated from the dissected specimen was sourced from other data where possible. The TLEM and AMS datasets provided PCSA data that, when scaled could be used allow the model to function. This is not ideal, but was preferable to a gap in the dataset. In accordance with the isometry principles outlined in Cuff, et al. (2016), muscle mass was scaled against body mass with a slope equal to 1.00, while PCSA was scaled against body mass with a slope of 0.667 (i.e. the area was proportional to two thirds of the mass). Most epaxial muscles were unable to be sourced from other canine studies; therefore, sarcomere length data was estimated from the one epaxial muscle measured in the dissection, sacrocaudalis dorsalis medialis. This was the best data available, hence was utilised for all epaxial muscles in this study.

Necessary for determining PCSA, the optimal fibre length of a muscle element part was defined as the position whereby the muscle has the greatest force potential. The optimal muscle fibre length (Lf_{opt} (cm)) was calculated as the mean muscle belly length or nominal fibre length (LF_{nom}(cm)), divided by the mean nominal sarcomere length of that muscle (LS_{nom} (μm)), multiplied by the optimum canine sarcomere length ($LS_{opt\ (canine)}$(μm)) identified in (Herzog, Kamal, & Clarke, 1992) as 2.5 μm (Horsman et al., 2007; Klein Breteler et al., 1999).
The equation for the calculation of optimal muscle fibre length is as follows:

$$LF_{opt} = LF_{nom} / LS_{nom} * LS_{opt\ (canine)}$$

Nominal fibre length was derived from the nominal muscle-tendon element length minus the nominal tendon length, and nominal sarcomere length was assessed from each muscle by averaging 100 sarcomere lengths as previously described in para 3.2.3.1.

As the model did not include all ventral muscles of the dog, two additional ventral stabilising muscles were added to the model. This addition's primary purpose was to provide resistance during extension of the spine, imitate the role of superficial ventral muscles such as rectus abdominis, and balance out the work done by the complete group of dorsal muscles modelled. The left and right ventral stabilisers attached to the bony protrusions of the pubic tubercle of the pelvis, and extended cranially to the ventral body of the fourth lumbar vertebra.

3.2.4.8 Modelling of ligament parameters

Ligaments were modelled in a similar fashion to the muscle-tendon elements. Ligament properties were less complex with smaller attachment sites compared to muscles, hence had fewer representative elements and nodes (Figure 3.11). All ligaments were modelled as straight lines in accordance with the methods used by (Carbone et al., 2015). All ligament attachment site data was acquired from the anatomy text (H. E. Evans & de Lahunta, 2013), and processed via SolidWorks as was described with muscle parameters in para 3.2.4.7. Biomechanical properties of ligaments were obtained from studies conducted on human subjects (Chazal et al., 1985; Pintar et al., 1992). The two ligament input parameter required for the model were stiffness and strain. Stiffness was calculated from the slope of the linear-most portion of the force-deformation curve, while strain at failure was scaled down by the human to canine mass ratio for use in the canine model.

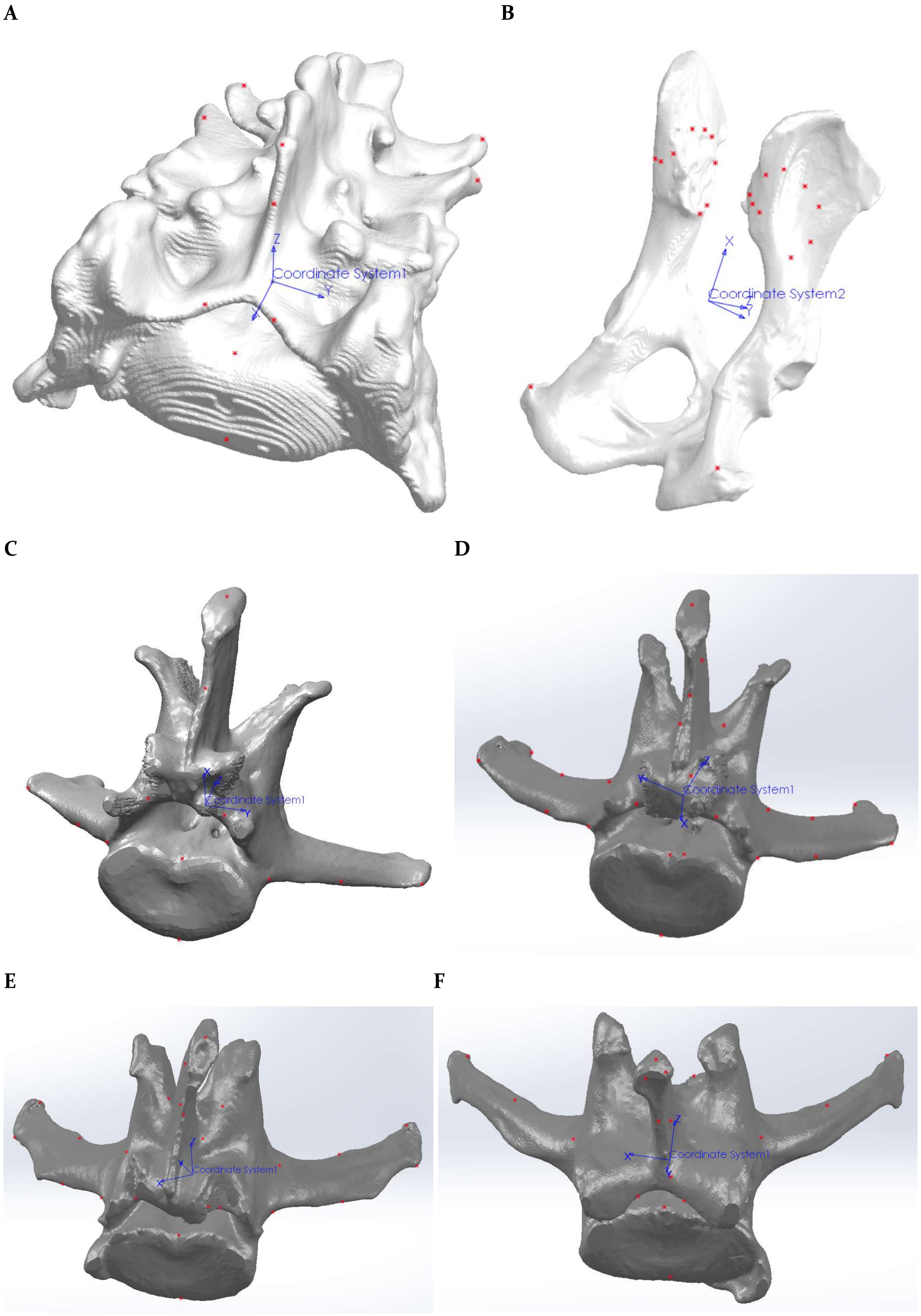

Figure 3.11. Ligament nodes of the sacrum (A), pelvis (B) and lumbar vertebrae L4-7 (C-F) as captured in SolidWorks.

3.2.4.9 Estimation of joint geometry

Joints were defined to constrain the segments with respect to each other. Spherical joints were assigned to all joints in the canine three-dimensional model, allowing 3 degrees of freedom, and 3 different rotations: flexion and extension, medial and lateral bending, and internal and external axial rotation. This type of joint was classed in the modelling software as a point constraint, also known as a ball-and-socket joint. Using a spherical joint acknowledged the factors influencing and limiting the joint range of motion, such as ligaments and bone contact, while accurately representing the overall range of movement through a single node.

In the lumbar vertebral joints of the canine specimen, the intervertebral junctions between adjacent vertebrae consisted of discs and paired facet joints between the bodies and articular processes respectively. Lumbar intervertebral joint rotation centres were calculated based on a spherical fit through the trajectory of the cranial vertebrae with respect to the caudal lumbar vertebrae. The intervertebral centre of rotation was allocated as the optical centroid of the intervertebral disc, at the midpoint between the two surrounding vertebral bodies. A single node was positioned equidistant from the two nodes assigned to the caudal face of the cranial vertebral body, and the cranial face of the adjacent caudal vertebral body.

The joints of the sacrum included the lumbo-sacral joint and a pair of sacroiliac joints. Lumbo-sacral joint rotation centres were calculated based on a spherical fit through the trajectory of the L7 vertebrae with respect to the sacrum, similar to the intervertebral joints. The left and right sacroiliac joints were each identified by a central node on the articular surface of each sacrum wing (Figure 3.12). A single node, central to the left and right sacroiliac joint nodes, was then identified to represented the overall model movement occurring between the sacrum and pelvis. The ranges of motion for input to the canine model were defined from the literature (Meij et al., 2007; Saunders et al., 2013; Schmidt et al., 1998), with the total motion restricted by limiting factors such as ligament and muscle-tendon element resistance, and by bone on bone contact (Carbone et al., 2015).

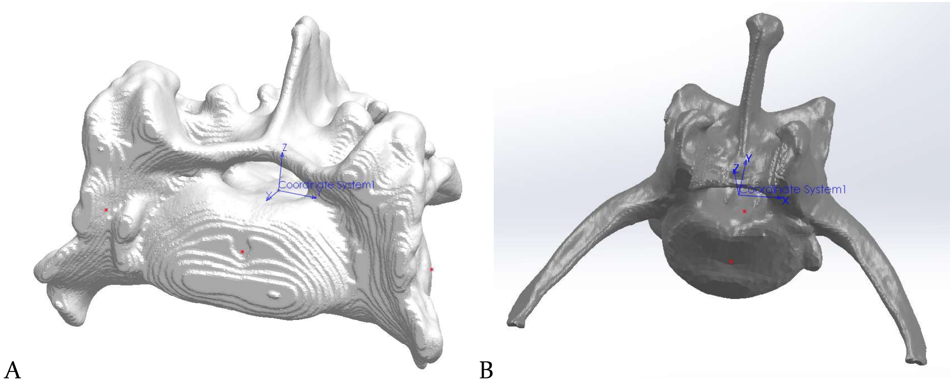

Figure 3.12. Joint nodes, and bone nodes of the sacrum (A) and L6 vertebrae as shown in SolidWorks.

3.2.5 Musculoskeletal model

3.2.5.1 Implementation into AnyBody Modeling System

The complete dataset, comprised of all aforementioned input parameters as drawn from the specimen and literature, was input into the AnyBody Modelling System (Figure 3.13). The result was a functioning canine model consisting of lumbar vertebrae four through seven, the sacrum, and the pelvis. Muscles were represented by the two-element muscle model (AnyMuscleModel2Elin), a bilinear model incorporating length and contraction velocity. This muscle representation presumed that muscle strength was proportional to the current length and contraction velocity, with the muscle weakening as its length decreased or contraction velocity increased. It also accounted for the build up of passive elasticity of a stretched muscle, which reduced the necessity for active muscle force. The two-element muscle model was selected due to the input parameter data available, and the necessary alterations to these parameters applied in the sensitivity analysis trials.

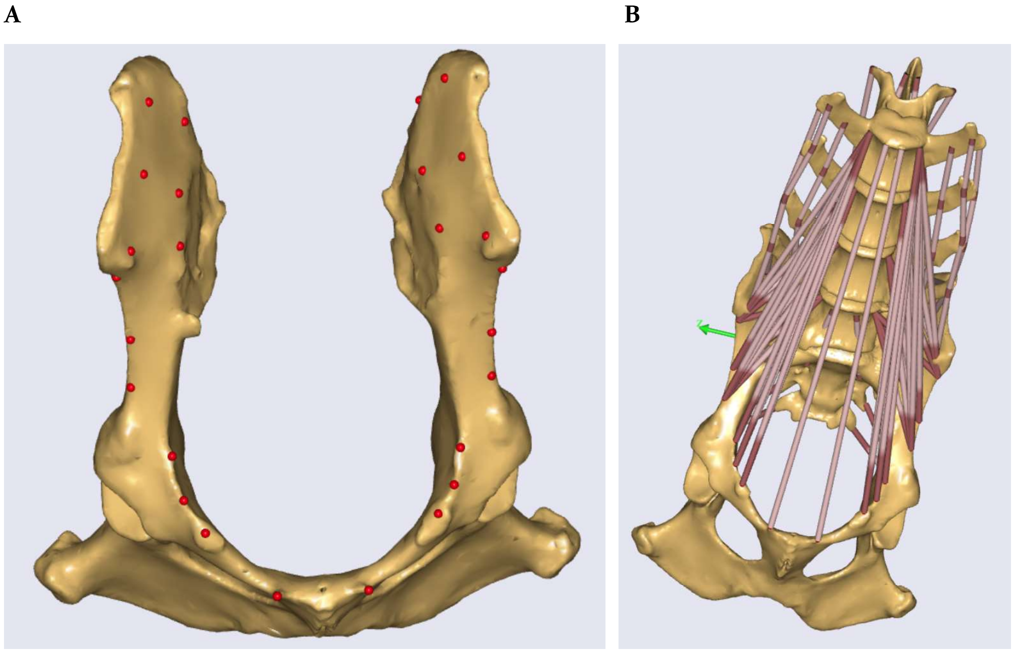

Figure 3.13. AMS muscle nodes (A), then shown with muscle elements attached (B).

The predefined specifications of joint nodes constraining the segments with respect to each other, and drivers defining the mechanism's movement assisted in determining where each bone segment was positioned in three-dimensional space at any point in time. However, several steps of definitions and equation solving were also required from the AnyBody Modelling System prior to the segments being arranged in their true anatomical positions. The model was required to be kinematically determinate for the system to perform a kinematic analysis to connect the model correctly at the joint nodes, with the purpose of determining all segment positions at all times.

Every segment possessed the two properties r0 and Axes0, which described the location in three-dimensional coordinates of the local origin in the global reference frame, and the orientation as a rotation matrix, respectively, of the segment at load time. A similar principle was applied to the segment nodes, but instead with sRel representing the relative position vector, and ARel representing the relative rotational transformation matrix, with respect to its base reference frame, i.e. the segment it attaches to.

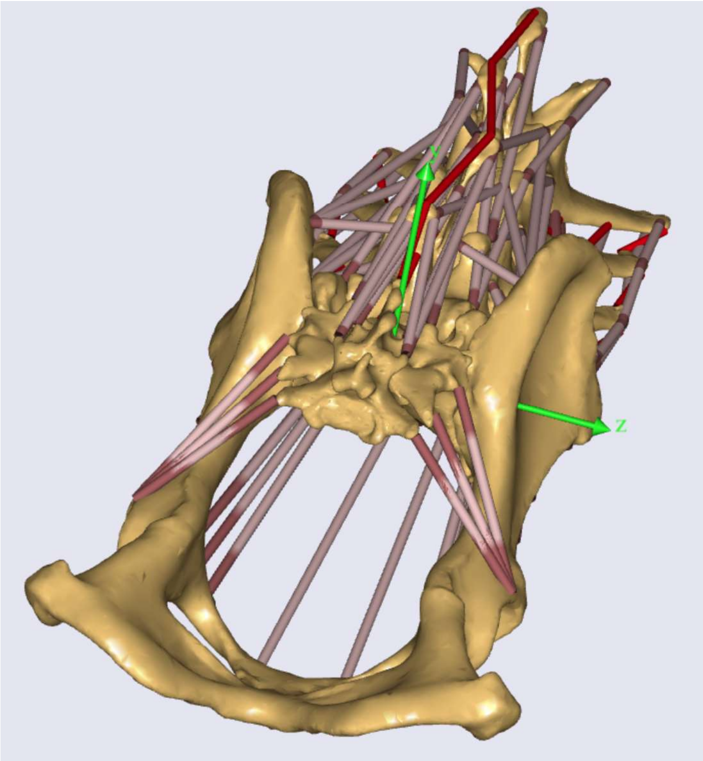

Figure 3.14. Full AMS muscle with all components attached.

With the model correctly configured and all parameter values input, simulations of the model ranges of motion were run for analysis. The kinematics simulation displayed only the model's range of motion across the three planes of flexion and extension, lateral bending, and axial rotation, as specified by external drivers. The inverse dynamics operation analysed the simulated muscle and joint forces across the model moving through its range of motion, computing the acting forces in any dynamic condition (Figure 3.15 - 3.18). Factors influencing the operation's dynamic analysis outputs for complex musculoskeletal systems included external force magnitudes and muscle attachment site locations. Inverse dynamics simulations in this study were utilised to quantify the linear forces acting on bones and joints, and to calculate the torsional moments around, and work done across the lumbar and lumbo-sacral joints in three-dimensions.

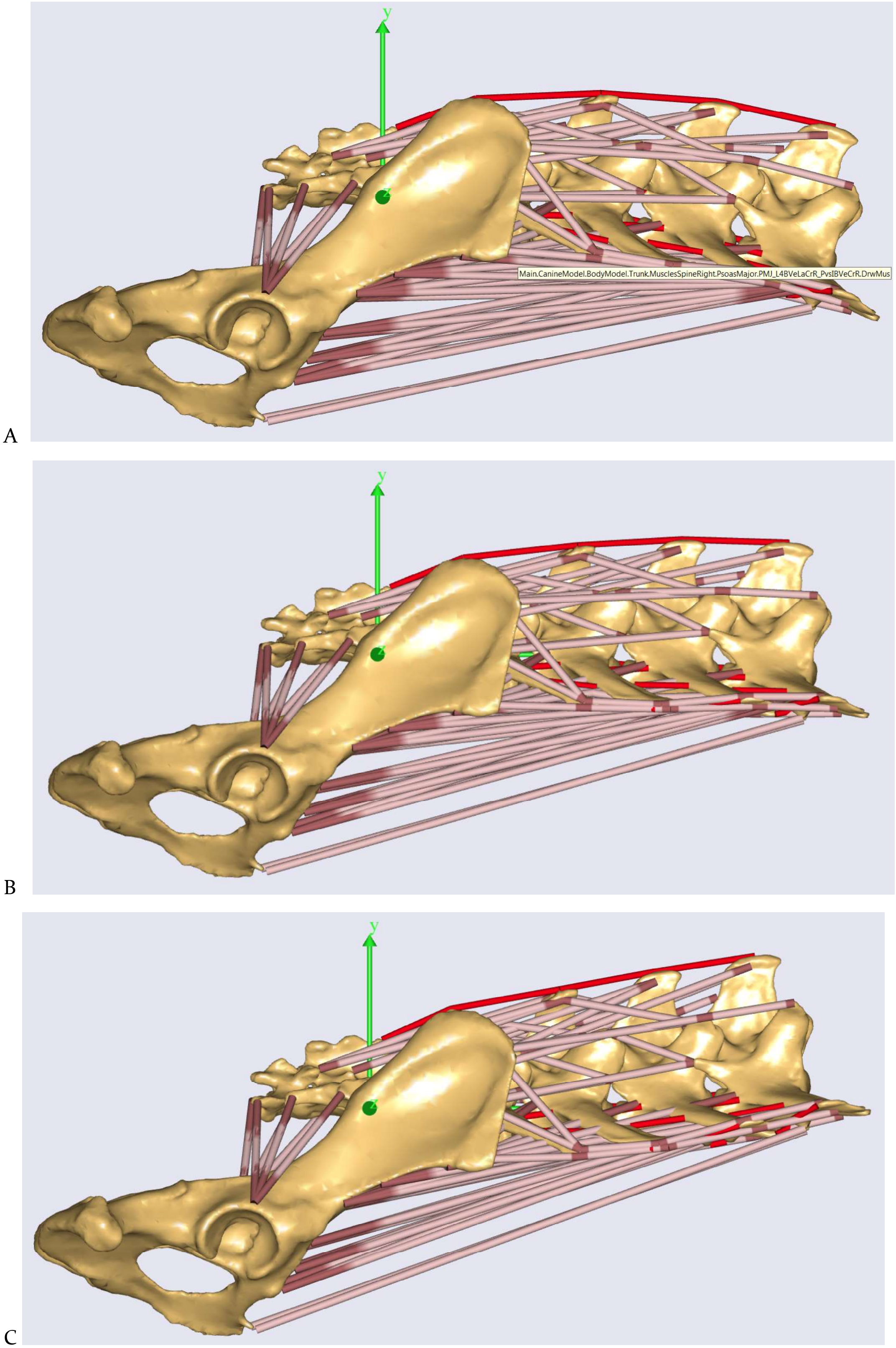

Figure 3.15. Flexion (A), neutral (B) and extension (C) spine positions.

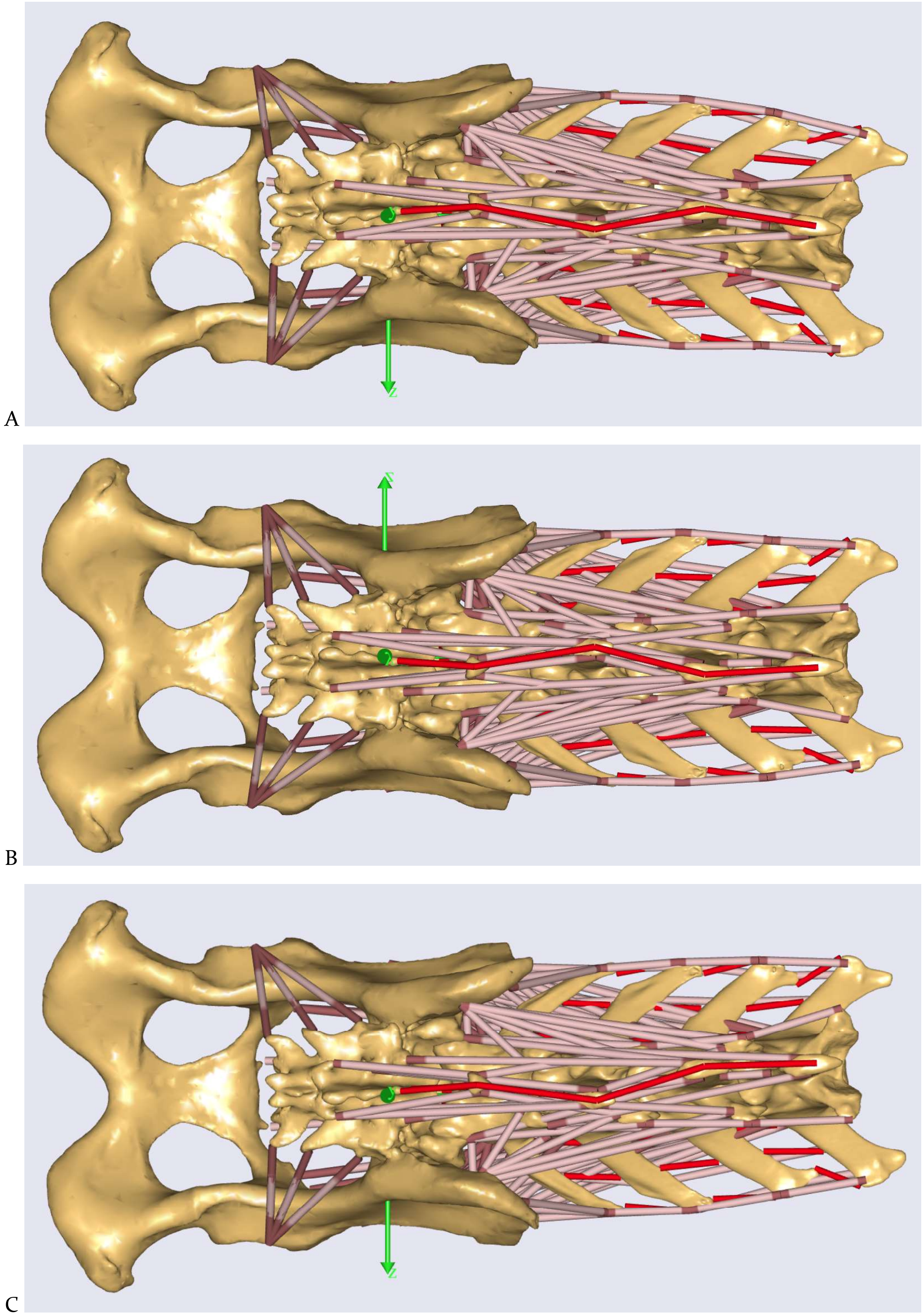

Figure 3.16. Lateral bending with left (A), neutral (B) and right (C) spine positions.

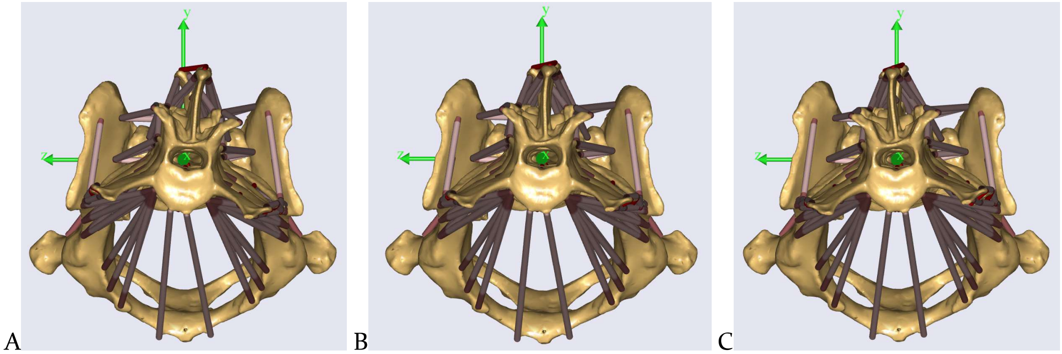

Figure 3.17. Axial rotation with anti-clockwise (A), neutral (B) and clockwise (C) spine positions.

3.2.5.2 Inverse Dynamics Sensitivity Analysis

The sensitivity analysis of the inverse dynamics simulations was run with small incremental alterations of soft tissue parameters commencing with the true value as measured from the specimen. The inverse dynamics outputs of force and strength were recorded for each trial. Outputs are detailed as follows:

- Force:

  Is the force in the muscle's contractile element. It is the product of tissue stress and cross-sectional area, with the smaller the tissue stress, the larger the cross-sectional area for a given force. The force in the contractile element decreased throughout the movement due to the moment arm of the external force reducing, and also because the passive force in the muscle is making an increasing contribution to balance the load.
- Strength:

  Is the muscle strength at each moment of the movement, or the muscle activation level compared to the muscle's maximum strength. Formulated mathematically:

  $$Strength = F_0\left(2\frac{L_m}{L_f}-1\right)\left(1-\frac{\dot{L}_m}{V_0}\right)$$

  Where *F0* is the muscle's presumed isometric strength, i.e. the force that the muscle can exert in a static condition at its optimum length, *Lm* is the length of the muscle's contractile element, *Lfbar* is the neutral fiber length, i.e. the length of the contractile element at which the muscle has the strength of F0, measured in length units, i.e. meters, *LmtDot* is the rate of change of Lmt, i.e. the length change velocity of the total muscle-tendon unit, and *V0* muscle's contraction velocity, measured in absolute velocity, i.e. m/s.

Two trials were run to independently alter the two parameters of interest, sarcomere length and the muscle-to-tendon length ratio, via the PCSA input parameter. These studies were run on the epaxial muscle sacrocaudalis dorsalis medialis, which was selected due to its span over the lumbo-sacral joint and representation in the model by a single element. Incremental adjustments of sarcomere length, then muscle-to-tendon input parameters were made, with outputs of force, strength, and activity recorded. Sarcomere length increment changes consisted of 0.1 μm, with a range of ± 0.7 μm from the true measured value, while muscle-to-tendon ratio increments were altered by the measurement accuracy value of 1 mm, with a range of ± 5 mm from the true measured value. In the latter trial, slack tendon length was altered alongside muscle fibre length enabling the sum of muscle and tendon lengths to match the original muscle-tendon element length. The purpose of running the sensitivity analysis was to analyse and compare varied/altered muscle measurement input parameters of the model and assess/determine the effect/impact on the inverse dynamic output values. The primary aim was to determine the necessity of measuring these input parameters in future modelling, or deeming, for example, the species optimal sarcomere length to be valid and sufficient.

An arbitrary threshold of ± 2.5% was assigned to the measured value's outputs displayed on the inverse dynamics graphs to show the total threshold window of 5% of the inverse dynamics output values from the true measured input data value. This margin identified which input value incremental adjustments resulted in output values within the 5% range. This threshold was employed to determine the required accuracy of cadaver muscle measurements gathered for model input parameters to obtain reliable inverse dynamics output data. The threshold also enabled determination of the variability of muscle input parameters that would be tolerated before exceeding the ± 2.5% value. Output values within this threshold were determined to have the level of accuracy required for muscle measurements without significantly affecting the output values. The ± 2.5% threshold was selected as an acceptable preliminary threshold to determine the significance of the effect of deviations from the true muscle input parameters on the inverse dynamics output data.

4. RESULTS

4.1 Cadaver measurements

Geometric parameters of muscles were measured from the cadaver, beginning with the lateral superficial muscles and continuing with deeper muscles as accessible in the dissection. A total of twelve muscles from the right side of the dog were excised with all morphometric data recorded in Table 4.1. The epaxial muscle sacrocaudalis dorsalis medialis, gluteal muscles, and piriformis were removed in their natural condition; while the remaining muscles were cut due to sectioning of the specimen, however, still partially contributed to a the dataset.

Table 4.1. Morphometric data from dissection of canine specimen with a neutral spine position.

	Muscle	State [1]	Lm_{nom} [2] (cm)	Lt_{nom} [3] (cm)	PA [4] (°)	Mass (g)	Vol [5] (cm^3)
1	gluteus superficialis	W	10.00	2.38	< 20	24.35	22.993
2	gluteus medius	W	10.80	7.32	< 20	77.57	73.248
3	piriformis	W	5.00	3.10	< 20	9.32	8.801
4	gluteus profundus	W	4.00	3.25	< 20	15.54	14.674
5	sacrocaudalis dorsalis medialis	W	6.50	2.63	< 20	4.50	4.249
6	sacrocaudalis dorsalis lateralis	C	13.50	0.50	< 20	7.66	7.233
7	multifidus lumborum	C	5.20	1.20	< 20	9.63	9.093
8	longissimus lumborum	C	2.30	0.50	< 20	3.74	3.532
9	iliocostalis lumborum	C	2.90	0.50	< 20	3.00	2.833
10	psoas major	C	-	3.27	< 20	-	-
11	psoas minor	C	-	4.40	< 20	-	-
12	iliacus	C	-	0.50	< 20	-	-

1 State: State of muscle in specimen (whole (W) or cut when GSD was sectioned (C))

2 Lm_{nom}: Muscle belly length (cm)

3 Lt_{nom}: Tendon length (cm)

4 PA: Pennation angle (°)

5 Vol: Volume (cm^3) measured via water dislocation method

4.2 Histology measurements

Nominal sarcomere length was calculated as the average of 100 sarcomere lengths measured from each muscle under microscopic examination, as recorded in Table 4.2. Microscope capture images indicate the spread of measurements across muscle fibres. Average sarcomere length possessed little variation across all muscles, ranging from 1.85 μm to 2.73 μm (mean 2.37 μm).

Table 4.2. Sarcomere length of muscles excised from canine specimen

	Area	**Ls $_{nom}$ (µm)**	**Ls Figures**	**Image Capture**
1	gluteus superficialis			
	1	26.41487885	**Min**	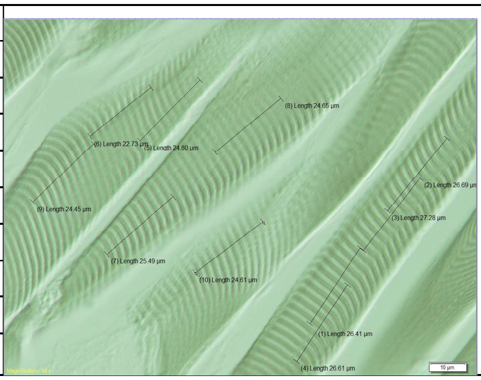
	2	26.69466782	22.72768021	
	3	27.27897263	**Max**	
	4	26.61006737	27.27897263	
	5	24.79997063	**Mean**	
	6	22.72768021	25.37274742	
	7	25.49367332	**Mean Ls $_{nom}$**	
	8	24.64838219	2.54	
	9	24.44833565		
	10	24.6108551	0.456	
2	gluteus medius			
	1	19.16699409	**Min**	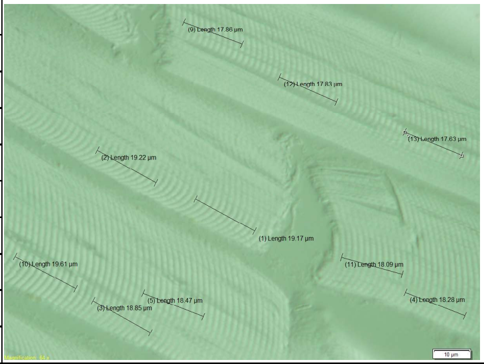
	2	19.21541977	17.62951851	
	3	18.85336876	**Max**	
	4	18.28478432	19.61095428	
	5	18.47268295	**Mean**	
	6	17.85848236	18.50117683	
	7	19.61095428	**Mean Ls $_{nom}$**	
	8	18.09381294	1.85	
	9	17.82575035		
	10	17.62951851	0.198	
3	piriformis			
	1	25.08724403	**Min**	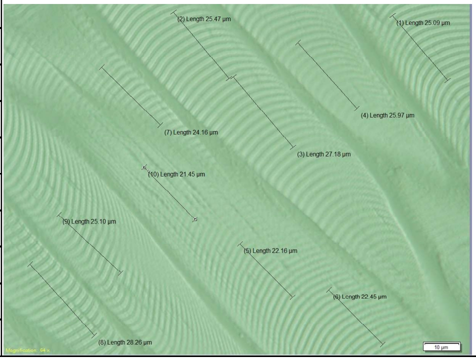
	2	25.47195053	21.45125961	
	3	27.17582893	**Max**	
	4	25.97146606	28.25615883	
	5	22.16294098	**Mean**	
	6	22.44799042	24.72884178	
	7	24.15913773	**Mean Ls $_{nom}$**	
	8	28.25615883	2.47	
	9	25.10444641		
	10	21.45125961	0.681	
4	gluteus profundus			
	1	23.25252914	**Min**	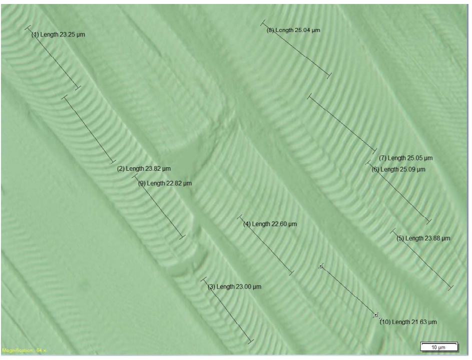
	2	23.82469559	21.62667847	
	3	22.99977303	**Max**	
	4	22.59950638	25.08825684	
	5	23.87579918	**Mean**	
	6	25.08825684	23.6178112	
	7	25.04611778	**Mean Ls $_{nom}$**	
	8	25.04185867	2.36	
	9	22.82289314		
	10	21.62667847	0.346	

	Area	**Ls $_{nom}$ (µm)**	**Ls Figures**	**Image Capture**
5	sacrocaudalis dorsalis medialis			
	1	25.60161209	**Min**	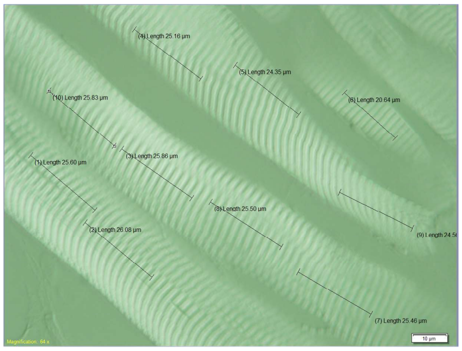
	2	26.08073807	20.63949776	
	3	25.85918045	**Max**	
	4	25.15597725	26.08073807	
	5	24.35176086	**Mean**	
	6	20.63949776	24.90500259	
	7	25.46337509	**Mean Ls $_{nom}$**	
	8	25.50004578	2.49	
	9	24.56459045		
	10	25.83324432	0.544	
6	sacrocaudalis dorsalis lateralis			
	1	27.38321304	**Min**	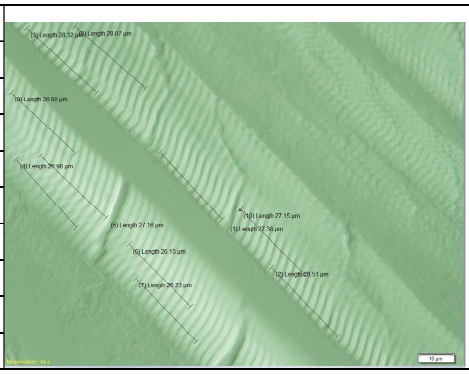
	2	28.51414871	26.15365601	
	3	28.317379	**Max**	
	4	26.97513199	28.51414871	
	5	27.1625576	**Mean**	
	6	26.15365601	27.2558136	
	7	26.23101807	**Mean Ls $_{nom}$**	
	8	28.07241821	2.73	
	9	26.59727669		
	10	27.15133667	0.236	
7	multifidus lumborum			
	1	24.63457489	**Min**	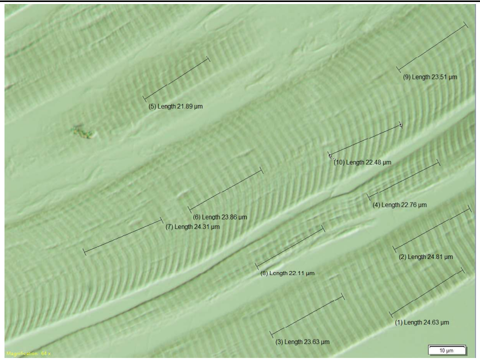
	2	24.80529404	21.89018822	
	3	23.63100052	**Max**	
	4	22.76184273	24.80529404	
	5	21.89018822	**Mean**	
	6	23.86494827	23.4004364	
	7	24.31168747	**Mean Ls $_{nom}$**	
	8	22.11338997	2.34	
	9	23.50818443		
	10	22.48325539	0.292	
8	longissimus lumborum			
	1	21.87788963	**Min**	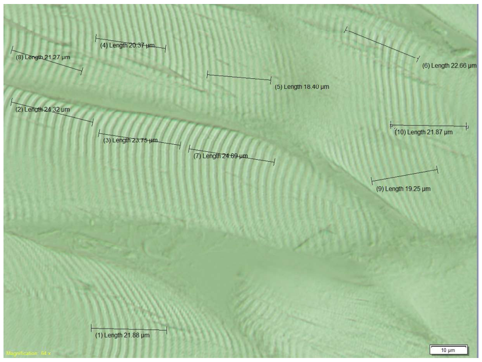
	2	24.32087708	18.40437889	
	3	23.7454834	**Max**	
	4	20.36704063	24.88705254	
	5	18.40437889	**Mean**	
	6	22.66345978	21.86594582	
	7	24.88705254	**Mean Ls $_{nom}$**	
	8	21.26579857	2.19	
	9	19.2542305		
	10	21.87324715	0.649	

	Area	Ls $_{\text{nom}}$ (µm)	Ls Figures	Image Capture
9	iliocostalis lumborum			
	1	27.09966469	**Min**	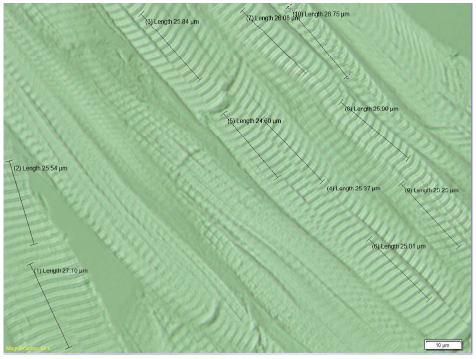
	2	25.54223251	24.59558105	
	3	25.836586	**Max**	
	4	25.37326813	27.09966469	
	5	24.59558105	**Mean**	
	6	25.01345062	25.74439812	
	7	26.08268547	**Mean Ls $_{\text{nom}}$**	
	8	25.8978405	2.57	
	9	25.25289345		
	10	26.74978065	0.314	
10	psoas major			
	1	21.17006111	**Min**	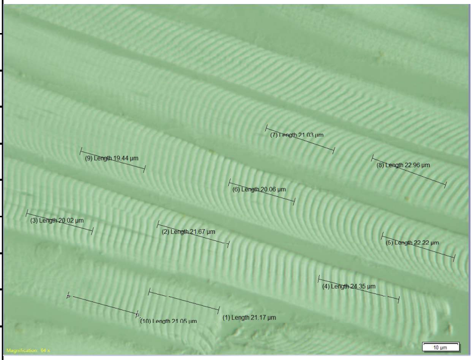
	2	21.66515541	19.43720055	
	3	20.02100182	**Max**	
	4	24.34571266	24.34571266	
	5	22.22152328	**Mean**	
	6	20.05952072	21.39562607	
	7	21.03408813	**Mean Ls $_{\text{nom}}$**	
	8	22.95512772	2.14	
	9	19.43720055		
	10	21.04688072	0.491	
11	psoas minor			
	1	25.51915741	**Min**	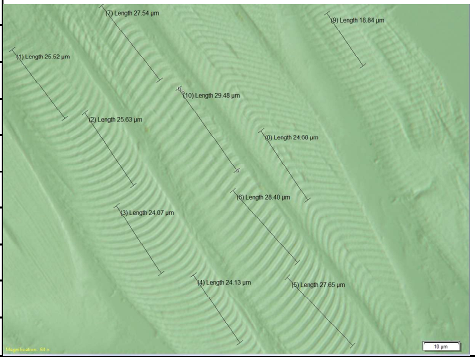
	2	25.63194275	18.84151268	
	3	24.06646919	**Max**	
	4	24.12548256	29.4764061	
	5	27.65339088	**Mean**	
	6	28.39850426	25.59386826	
	7	27.54408836	**Mean Ls $_{\text{nom}}$**	
	8	24.6817379	2.56	
	9	18.84151268		
	10	29.4764061	1.064	
12	iliacus			
	1	22.05152702	**Min**	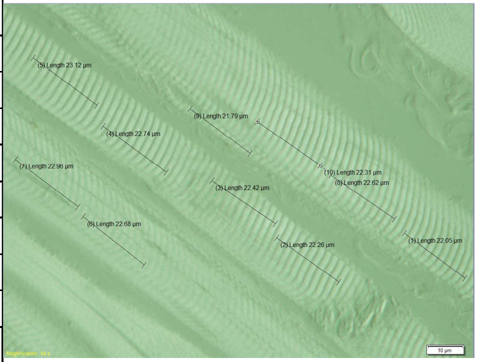
	2	22.259655	21.79160118	
	3	22.41810799	**Max**	
	4	22.74019051	23.11935997	
	5	23.11935997	**Mean**	
	6	22.68137932	22.49437141	
	7	22.958004	**Mean Ls $_{\text{nom}}$**	
	8	22.6150074	2.25	
	9	21.79160118		
	10	22.30887985	0.133	

4.3 Bony landmarks

Positions of prominent bony landmarks of the sacrum and pelvis bone segments were identified with coordinates acquired from the SolidWorks local reference frames. Each local coordinate was then transformed into the AnyBody Modeling System global model reference frame to enable alignment and orientation of bone segments into their true anatomical positions as observed in the intact specimen.

Table 4.3. Positions (X, Y, Z) of prominent bony landmarks of the sacrum with respect to the local and model global reference frames (in mm).

	Landmark	Local Position	Global Position
1	Left wing, dorsal tip	9.70, 18.96, 17.05	15.0, 11.42, -18.91
2	Right wing, dorsal tip	11.10, -17.41, 17.32	14.0, 12.24, 16.69
3	Median sacral crest S3, caudodorsal point	-24.71, -4.62, 14.33	-18.98, 20.55, 0.69
4	Right lateral sacral crest S3, caudal	-26.16, -18.69, -3.30	-20.73, 4.89, 14.71
5	Left lateral sacral crest S3, caudal	-27.77, 15.80, -1.64	-24.86, 6.21, -19.57

Table 4.4: Positions (X, Y, Z) of prominent bony landmarks of the pelvis with respect to the local and model global reference frames (in mm).

	Landmark	Local Position	Global Position
1	Left cranial dorsal iliac spine	62.98, -30.59, -25.44	16.90, 25.64, -29.82
2	Right cranial dorsal iliac spine	65.68, 27.07, -26.77	19.18, 27.49, 28.27
3	Right caudal dorsal iliac spine	29.51, 25.04, -13.41	-5.61, 2.92, 23.99
4	Left caudal dorsal iliac spine	29.61, -30.37, -13.61	-7.11, 0.64, -31.32

4.4 Bone segment origins

The origin for each of the six bone segments were identified as the segment centre of mass and assigned the (0,0,0) coordinate position in their local reference frames. These six bone segment origins were then transformed to the model global reference frame coordinates as described in Table 4.5. These positions of origin were calculated as the centre of mass for each bone segment.

Table 4.5. Positions (X, Y, Z) of the origin for each bone segment with respect to the model global reference frame (in mm) with the model at the neutral position.

Bone Segment	Origin Position
L4	123.7726, -1.35543, -0.05459954
L5	93.14771, -0.4442574, -0.1039912
L6	62.74051, -0.6563919, -0.04212698
L7	34.01678, -2.204375, -0.4571008
Sacrum	1.289303, -0.8117111, -1.764287
Pelvis	-28.00424, -23.91573, -0.001996682

4.5 Inertial parameters

Inertial parameters as reported in Table 4.6 were calculated in SolidWorks from the uniform bone density of 1400 kg/m^3. Bone mass (Table 4.6) ranged from 25.5 g to 119.7 g (mean 43.9 g).

Table 4.6. Principal axes and moments of inertia taken at the centre of mass of each bone segment.

Bone Segment	Bone Mass (g)	Principal axes of inertia	Principal moments of inertia (grams * mm^2)
L4	25.49224	Ix = 121.9036, 8.393117, -1.268365	Px = 4606.50536
		Iy = 123.8862, -0.09853916, 9.865473	Py = 5616.04216
		Iz = 133.5957, 0.4848095, -0.4003288	Pz = 5721.88379
L5	27.16023	Ix = 97.22423, -9.563972, 0.3572228	Px = 5398.97511
		Iy = 95.76986, 0.2410553, -9.729725	Py = 6188.72470
		Iz = 101.8945, 3.600603, 2.566727	Pz = 6327.08755
L6	27.23259	Ix = 62.40822, -4.046043, -9.444263	Px = 5263.79996
		Iy = 58.50534, 7.912263, -2.981636	Py = 5618.60942
		Iz = 71.79326, 3.227911, -1.762428	Pz = 6045.95525
L7	26.07071	Ix = 35.06601, -1.572666, -10.38179	Px = 4370.59779
		Iy = 25.4778, 2.968338, -1.030588	Py = 5317.58222
		Iz = 39.11433, 6.330492, 0.6249854	Pz = 5557.29576
Sacrum	37.43444	Ix = 10.8011, -3.845707, -1.198121	Px = 7601.08037
		Iy = 1.811699, -1.037012, -11.74809	Py = 9194.79001
		Iz = 4.33114, 8.714259, -1.820094	Pz = 13451.23650
Pelvis	119.72186	Ix = -18.9784, -19.61058, -0.002962693	Px = 141551.62437
		Iy = -28.00358, -23.91487, 9.998003	Py = 231539.94246
		Iz = -23.6991, -32.94156, -0.001507935	Pz = 336784.33408

4.6 Muscle parameters

The complete set of muscle parameters for the musculoskeletal model in the AnyBody Modeling System is described in Table 4.7. The input parameters for the 2E muscle model drawn from the dataset below were nominal tendon length (Lt_{nom}), nominal fibre length (Lf_{nom}), and physiological cross-sectional area (PCSA).

The Muscle-tendon element length (Lmt) was calculated as the combined nominal tendon and nominal fibre lengths. The physiological cross-sectional area calculation was more complex, incorporating nominal fibre length and nominal sarcomere length variables within the optimal fibre length factor of the equation.

There was some variation observed in values among the different muscles. PCSA varied from 1.05 to 7.33 in the epaxial muscles (mean 3.22), 0.58 to 10.277 in the hypaxial muscles (mean 3.32) and from 3.50 to 3.56 in the gluteal muscles (mean 3.53).

Table 4.7. Muscle parameters of the canine spine model with respect to the model global reference frame (in mm) with the model at the neutral position.

Muscle [1] **(MuscleName_Origin_Insertion)**	**E#** [2]	**Ori Info** [3]	**Ins Info** [4]	**Mass** [5] **(g)**	**Vol** [6] **(mL)**	**Lf_{opt}** [7] **(cm)**	**Lf_{nom}** [8] **(cm)**	**Lt_{nom}** [9] **(cm)**	**Lmt** [10] **(cm)**	**Ls_{nom}** [11] **(μm)**	**PCSA** [12]
M1 IliocostalisLumborum IL-L				**8.5** ^{D}	**8.036**	**2.489**				**2.574**	**3.229** ^{S}
IL_PvsMIWDoCrL_L7TPDoLaL	1	Ls 1/2	P	2.5	2.374	3.675	3.784	0.500	4.284	2.574	0.646
IL_PvsMIWMiCrL_L7TPDoLaL	2	Ls 2/2	P	1.8	1.703	2.636	2.714	0.500	3.214	2.574	0.646
IL_L7TPDoLaL_L6TPDoLaL	3	P	P	1.3	1.245	1.928	1.985	0.500	2.485	2.574	0.646
IL_L6TPDoLaL_L5TPDoLaL	4	P	P	1.4	1.288	1.994	2.053	0.500	2.553	2.574	0.646
IL_L5TPDoLaL_L4TPDoLaL	5	P	P	1.5	1.428	2.210	2.276	0.500	2.776	2.574	0.646
M1 IliocostalisLumborum IL-R				**8.1** ^{D}	**7.655**	**2.371**				**2.574**	**3.229** ^{S}
IL_PvsMIWDoCrR_L7TPDoLaR	1	Ls 1/2	P	2.3	2.138	3.309	3.407	0.500	3.907	2.574	0.646
IL_PvsMIWMiCrR_L7TPDoLaR	2	Ls 2/2	P	1.8	1.728	2.675	2.754	0.500	3.254	2.574	0.646
IL_L7TPDoLaR_L6TPDoLaR	3	P	P	1.3	1.194	1.848	1.903	0.500	2.403	2.574	0.646
IL_L6TPDoLaR_L5TPDoLaR	4	P	P	1.4	1.355	2.098	2.160	0.500	2.660	2.574	0.646
IL_L5TPDoLaR_L4TPDoLaR	5	P	P	1.3	1.243	1.924	1.981	0.500	2.481	2.574	0.646
M2 LongissimusLumborum LL-L				**13.3** ^{D}	**12.516**	**4.845**				**2.187**	**2.583** ^{S}
LL_L7SPL_L6CAPL	1	P	P	1.4	1.287	4.486	3.924	0.500	4.424	2.187	0.287
LL_L6SPL_L5CAPL	2	P	P	1.3	1.225	4.269	3.735	0.500	4.235	2.187	0.287
LL_PvsMIWDoCaL_L7CAPL	3	P	P	0.8	0.771	2.687	2.351	0.500	2.851	2.187	0.287
LL_PvsMIWDoCaL_L6CAPL	4	P	P	1.6	1.506	5.247	4.590	0.500	5.090	2.187	0.287
LL_PvsMIWDoCaL_L5CAPL	5	P	P	2.7	2.503	8.723	7.631	0.500	8.131	2.187	0.287
LL_PvsMIWMiCaL_L7ALaL	6	P	P	0.3	0.323	1.126	0.985	0.500	1.485	2.187	0.287
LL_PvsMIWMiCaL_L6APL	7	P	P	0.8	0.793	2.765	2.419	0.500	2.919	2.187	0.287
LL_PvsMIWMiCaL_L5APL	8	P	P	1.7	1.631	5.684	4.972	0.500	5.472	2.187	0.287
LL_PvsMIWMiCaL_L4APL	9	P	P	2.6	2.475	8.622	7.543	0.500	8.043	2.187	0.287

Muscle [1] (MuscleName_Origin_Insertion)	E# [2]	Ori Info [3]	Ins Info [4]	Mass [5] (g)	Vol [6] (mL)	Lf_{opt} [7] (cm)	Lf_{nom} [8] (cm)	Lt_{nom} [9] (cm)	Lmt [10] (cm)	Ls_{nom} [11] (μm)	PCSA [12]
M2 LongissimusLumborum LL-R				**12.5**[D]	**11.823**	**4.577**				**2.187**	**2.583**[S]
LL_L7SPR_L6CAPR	1	P	P	1.3	1.244	4.333	3.790	0.500	4.290	2.187	0.287
LL_L6SPR_L5CAPR	2	P	P	1.3	1.194	4.159	3.638	0.500	4.138	2.187	0.287
LL_PvsMIWDoCaR_L7CAPR	3	P	P	0.7	0.628	2.186	1.913	0.500	2.413	2.187	0.287
LL_PvsMIWDoCaR_L6CAPR	4	P	P	1.4	1.307	4.555	3.984	0.500	4.484	2.187	0.287
LL_PvsMIWDoCaR_L5CAPR	5	P	P	2.5	2.355	8.204	7.177	0.500	7.677	2.187	0.287
LL_PvsMIWMiCaR_L7ALaR	6	P	P	0.4	0.357	1.242	1.087	0.500	1.587	2.187	0.287
LL_PvsMIWMiCaR_L6APR	7	P	P	0.7	0.706	2.461	2.153	0.500	2.653	2.187	0.287
LL_PvsMIWMiCaR_L5APR	8	P	P	1.7	1.592	5.547	4.852	0.500	5.352	2.187	0.287
LL_PvsMIWMiCaR_L4APR	9	P	P	2.6	2.442	8.508	7.443	0.500	7.943	2.187	0.287
M3 MultifidusLumborum ML-L				**56.2**[D]	**53.045**	**7.242**				**2.340**	**7.325**[S]
ML_SacMPLCa1_L6SPL	1	P	P	11.6	10.930	7.461	6.983	1.200	8.183	2.340	1.465
ML_SacISCLS3_L6SPL	2	P	P	9.8	9.220	6.294	5.891	1.200	7.091	2.340	1.465
ML_SacISCLS2_L5SPL	3	P	P	13.1	12.393	8.459	7.918	1.200	9.118	2.340	1.465
ML_SacCAPLS1_L5SPL	4	P	P	10.7	10.086	6.885	6.444	1.200	7.644	2.340	1.465
ML_L7MPL_L4SPL	5	P	P	11.0	10.416	7.110	6.655	1.200	7.855	2.340	1.465
M3 MultifidusLumborum ML-R				**56.7**[D]	**53.582**	**7.315**				**2.340**	**7.325**[S]
ML_SacMPRCa1_L6SPR	1	P	P	11.4	10.766	7.349	6.878	1.200	8.078	2.340	1.465
ML_SacISCRS3_L6SPR	2	P	P	9.8	9.245	6.311	5.907	1.200	7.107	2.340	1.465
ML_SacISCRS2_L5SPR	3	P	P	13.3	12.597	8.598	8.048	1.200	9.248	2.340	1.465
ML_SacCAPRS1_L5SPR	4	P	P	10.7	10.089	6.886	6.446	1.200	7.646	2.340	1.465
ML_L7MPR_L4SPR	5	P	P	11.5	10.885	7.430	6.955	1.200	8.155	2.340	1.465
M4 Interspinales IS-C				**4.1**[D]	**3.900**	**1.249**				**2.491**	**3.123**[D]
IS_L7SPMiCr_L6SPMiCa	1	P	P	1.6	1.476	1.418	1.413	0.500	1.913	2.491	1.041
IS_L6SPMiCr_L5SPMiCa	2	P	P	1.4	1.324	1.272	1.267	0.500	1.767	2.491	1.041
IS_L5SPMiCr_L4SPMiCa	3	P	P	1.2	1.101	1.057	1.054	0.500	1.554	2.491	1.041

Muscle[1] (MuscleName_Origin_Insertion)	E#[2]	Ori Info[3]	Ins Info[4]	Mass[5] (g)	Vol[6] (mL)	Lf_{opt}[7] (cm)	Lf_{nom}[8] (cm)	Lt_{nom}[9] (cm)	Lmt[10] (cm)	Ls_{nom}[11] (μm)	PCSA[12]
M5 IntertransversariiLumborum ITL-L				**5.0**[D]	**4.718**	**2.185**				**2.491**	**2.108**[D]
ITL_L7MPL_L5APL	1	P	P	2.6	2.414	2.291	2.282	0.500	2.782	2.491	1.054
ITL_L6MPL_L4APL	2	P	P	2.4	2.303	2.185	2.177	0.500	2.677	2.491	1.054
M5 IntertransversariiLumborum ITL-R				**5.5**	**5.235**	**2.548**				**2.491**	**2.054**[D]
ITL_L7MPR_L5APR	1	P	P	2.9	2.702	2.631	2.622	0.500	3.122	2.491	1.027
ITL_L6MPR_L4APR	2	P	P	2.7	2.532	2.466	2.457	0.500	2.957	2.491	1.027
M6 SacrocaudalisDorsalisLateralis SDL-L				**10.4**[D]	**9.816**	**3.104**				**2.726**	**3.162**[D]
SDL_L4MPL_L5MPL	1	P	P	2.6	2.455	2.329	2.540	0.500	3.040	2.726	1.054
SDL_L5MPL_L6MPL	2	P	P	2.5	2.366	2.245	2.448	0.500	2.948	2.726	1.054
SDL_L6MPL_SacCAPLS1	3	P	P	5.3	4.995	4.739	5.168	0.500	5.668	2.726	1.054
M6 SacrocaudalisDorsalisLateralis SDL-R				**10.0**[D]	**9.443**	**3.065**				**2.726**	**3.081**[D]
SDL_L4MPR_L5MPR	1	P	P	2.5	2.337	2.276	2.481	0.500	2.981	2.726	1.027
SDL_L5MPR_L6MPR	2	P	P	2.6	2.487	2.421	2.640	0.500	3.140	2.726	1.027
SDL_L6MPR_SacCAPRS1	3	P	P	4.9	4.619	4.498	4.904	0.500	5.404	2.726	1.027
M7 SacrocaudalisDorsalisMedialis SDM-L				**4.5**	**4.249**	**4.032**				**2.491**	**1.054**
SDM_L7SPL_ SacMPLCa1	1	P	P	4.5	4.249	4.032	4.018	0.500	4.518	2.491	1.054
M7 SacrocaudalisDorsalisMedialis SDM-R				**4.5**	**4.249**	**4.136**				**2.491**	**1.027**
SDM_L7SPR_ SacMPRCa1	1	P	P	4.5	4.249	4.136	4.121	0.500	4.621	2.491	1.027
M8 SacrocaudalisVentralisLateralis SVL-L				**3.3**[D]	**3.070**	**2.913**				**2.491**	**1.054**[D]
SVL_L7BVeMeCrL_SacBVeLaLS1	1	P	P	3.3	3.070	2.913	2.902	0.500	3.402	2.491	1.054
M8 SacrocaudalisVentralisLateralis SVL-R				**3.0**[D]	**2.851**	**2.776**				**2.491**	**1.027**[D]
SVL_L7BVeMeCrR_SacBVeLaRS1	1	P	P	3.0	2.851	2.776	2.766	0.500	3.266	2.491	1.027

Muscle [1] (MuscleName_Origin_Insertion)	E# [2]	Ori Info [3]	Ins Info [4]	Mass [5] (g)	Vol [6] (mL)	Lf $_{opt}$ [7] (cm)	Lf $_{nom}$ [8] (cm)	Lt $_{nom}$ [9] (cm)	Lmt [10] (cm)	Ls $_{nom}$ [11] (μm)	PCSA [12]
M9 PsoasMinor PMN-L				**6.1** [D]	**5.769**	**9.946**				**2.559**	**0.580** [S]
PMR_L4BVeLaCrL_PvsALVeCrL	1	P	Lc1/3	1.1	1.050	10.860	11.116	4.401	15.517	2.559	0.097
PMR_L4BVeLaCrL_PvsALVeMiL	2	P	Lc2/3	1.2	1.100	11.382	11.651	4.401	16.052	2.559	0.097
PMR_L4BVeLaCrL_PvsALVeCaL	3	P	Lc3/3	1.2	1.139	11.784	12.062	4.401	16.462	2.559	0.097
PMR_L5BVeLaCrL_PvsALVeCrL	4	P	Lc1/3	0.8	0.778	8.051	8.241	4.401	12.642	2.559	0.097
PMR_L5BVeLaCrL_PvsALVeMiL	5	P	Lc2/3	0.9	0.831	8.594	8.797	4.401	13.198	2.559	0.097
PMR_L5BVeLaCrL_PvsALVeCaL	6	P	Lc3/3	0.9	0.871	9.008	9.221	4.401	13.621	2.559	0.097
M9 PsoasMinor PMN-R				**6.1** [D]	**5.718**	**9.859**				**2.559**	**0.580** [S]
PMR_L4BVeLaCrR_PvsALVeCrR	1	P	Lc1/3	1.1	1.034	10.700	10.953	4.401	15.354	2.559	0.097
PMR_L4BVeLaCrR_PvsALVeMiR	2	P	Lc2/3	1.2	1.094	11.317	11.584	4.401	15.985	2.559	0.097
PMR_L4BVeLaCrR_PvsALVeCaR	3	P	Lc3/3	1.2	1.140	11.797	12.076	4.401	16.476	2.559	0.097
PMR_L5BVeLaCrR_PvsALVeCrR	4	P	Lc1/3	0.8	0.760	7.857	8.042	4.401	12.443	2.559	0.097
PMR_L5BVeLaCrR_PvsALVeMiR	5	P	Lc2/3	0.9	0.821	8.494	8.695	4.401	13.096	2.559	0.097
PMR_L5BVeLaCrR_PvsALVeCaR	6	P	Lc3/3	0.9	0.869	8.988	9.200	4.401	13.601	2.559	0.097
M10 PsoasMajor PMJ-L				**63.8** [D]	**60.283**	**5.866**				**2.140**	**10.277** [S]
PMJ_L4BVeLaCrL_PvsIBVeCrL	1	P	Lc1/3	4.4	4.179	9.530	8.158	3.272	11.429	2.140	0.428
PMJ_L4BVeLaCrL_PvsIBVeMiL	2	P	Lc2/3	5.5	5.211	11.884	10.172	3.272	13.444	2.140	0.428
PMJ_L4BVeLaCrL_PvsIBVeCaL	3	P	Lc3/3	6.1	5.758	13.131	11.240	3.272	14.512	2.140	0.428
PMJ_L5BVeLaCrL_PvsIBVeCrL	4	P	Lc1/3	2.9	2.730	6.225	5.329	3.272	8.600	2.140	0.428
PMJ_L5BVeLaCrL_PvsIBVeMiL	5	P	Lc2/3	4.0	3.736	8.520	7.293	3.272	10.564	2.140	0.428
PMJ_L5BVeLaCrL_PvsIBVeCaL	6	P	Lc3/3	4.5	4.282	9.765	8.359	3.272	11.630	2.140	0.428
PMJ_L6BVeLaCrL_PvsIBVeCrL	7	P	Lc1/3	1.4	1.365	3.113	2.664	3.272	5.936	2.140	0.428
PMJ_L6BVeLaCrL_PvsIBVeMiL	8	P	Lc2/3	2.4	2.295	5.235	4.481	3.272	7.753	2.140	0.428
PMJ_L6BVeLaCrL_PvsIBVeCaL	9	P	Lc3/3	3.0	2.831	6.456	5.526	3.272	8.798	2.140	0.428
PMJ_L7BVeLaCrL_PvsIBVeCrL	10	P	Lc1/3	0.2	0.201	0.459	0.393	3.272	3.664	2.140	0.428
PMJ_L7BVeLaCrL_PvsIBVeMiL	11	P	Lc2/3	1.0	0.910	2.075	1.776	3.272	5.048	2.140	0.428

Muscle [1] **(MuscleName_Origin_Insertion)**	**E#** [2]	**Ori Info** [3]	**Ins Info** [4]	**Mass** [5] **(g)**	**Vol** [6] **(mL)**	**Lf** $_{opt}$ [7] **(cm)**	**Lf** $_{nom}$ [8] **(cm)**	**Lt** $_{nom}$ [9] **(cm)**	**Lmt** [10] **(cm)**	**Ls** $_{nom}$ [11] **(μm)**	**PCSA** [12]
PMJ_L7BVeLaCrL_PvsIBVeCaL	12	P	Lc3/3	1.5	1.414	3.224	2.759	3.272	6.031	2.140	0.428
PMJ_L4BLaCaL_PvsIBVeCrL	13	P	Lc1/3	3.5	3.331	7.595	6.501	3.272	9.773	2.140	0.428
PMJ_L4BLaCaL_PvsIBVeMiL	14	P	Lc2/3	4.6	4.374	9.974	8.538	3.272	11.809	2.140	0.428
PMJ_L4BLaCaL_PvsIBVeCaL	15	P	Lc3/3	5.2	4.936	11.257	9.636	3.272	12.907	2.140	0.428
PMJ_L5BLaCaL_PvsIBVeCrL	16	P	Lc1/3	2.0	1.898	4.327	3.704	3.272	6.976	2.140	0.428
PMJ_L5BLaCaL_PvsIBVeMiL	17	P	Lc2/3	3.1	2.907	6.629	5.675	3.272	8.946	2.140	0.428
PMJ_L5BLaCaL_PvsIBVeCaL	18	P	Lc3/3	3.7	3.473	7.921	6.780	3.272	10.052	2.140	0.428
PMJ_L6BLaCaL_PvsIBVeCrL	19	P	Lc1/3	0.7	0.696	1.587	1.359	3.272	4.630	2.140	0.428
PMJ_L6BLaCaL_PvsIBVeMiL	20	P	Lc2/3	1.7	1.599	3.646	3.121	3.272	6.392	2.140	0.428
PMJ_L6BLaCaL_PvsIBVeCaL	21	P	Lc3/3	2.3	2.158	4.921	4.213	3.272	7.484	2.140	0.428
PMJ_L7BLaCaL_PvsIBVeCrL	22	P	Lc1/3	0.0	0.000	0.000	0.000	3.072	3.072	2.140	0.428
PMJ_L7BLaCaL_PvsIBVeMiL	23	P	Lc2/3	0.5	0.471	1.074	0.919	3.272	4.191	2.140	0.428
PMJ_L7BLaCaL_PvsIBVeCaL	24	P	Lc3/3	1.0	0.979	2.232	1.910	3.272	5.182	2.140	0.428
M10 PsoasMajor PMJ-R				**60.7** [D]	**57.324**	**5.578**				**2.140**	**10.277** [S]
PMJ_L4BVeLaCrR_PvsIBVeCrR	1	P	Lc1/3	4.2	3.963	9.256	7.923	3.272	11.194	2.140	0.428
PMJ_L4BVeLaCrR_PvsIBVeMiR	2	P	Lc2/3	5.2	4.937	11.529	9.868	3.272	13.140	2.140	0.428
PMJ_L4BVeLaCrR_PvsIBVeCaR	3	P	Lc3/3	5.8	5.522	12.895	11.038	3.272	14.310	2.140	0.428
PMJ_L5BVeLaCrR_PvsIBVeCrR	4	P	Lc1/3	2.7	2.546	5.947	5.090	3.272	8.362	2.140	0.428
PMJ_L5BVeLaCrR_PvsIBVeMiR	5	P	Lc2/3	3.7	3.489	8.147	6.974	3.272	10.245	2.140	0.428
PMJ_L5BVeLaCrR_PvsIBVeCaR	6	P	Lc3/3	4.3	4.071	9.507	8.138	3.272	11.410	2.140	0.428
PMJ_L6BVeLaCrR_PvsIBVeCrR	7	P	Lc1/3	1.2	1.162	2.715	2.324	3.272	5.595	2.140	0.428
PMJ_L6BVeLaCrR_PvsIBVeMiR	8	P	Lc2/3	2.2	2.034	4.749	4.065	3.272	7.337	2.140	0.428
PMJ_L6BVeLaCrR_PvsIBVeCaR	9	P	Lc3/3	2.8	2.611	6.098	5.220	3.272	8.491	2.140	0.428
PMJ_L7BVeLaCrR_PvsIBVeCrR	10	P	Lc1/3	0.1	0.112	0.262	0.224	3.272	3.496	2.140	0.428
PMJ_L7BVeLaCrR_PvsIBVeMiR	11	P	Lc2/3	0.8	0.743	1.735	1.485	3.272	4.756	2.140	0.428
PMJ_L7BVeLaCrR_PvsIBVeCaR	12	P	Lc3/3	1.4	1.288	3.008	2.575	3.272	5.846	2.140	0.428

Muscle [1] (MuscleName_Origin_Insertion)	E# [2]	Ori Info [3]	Ins Info [4]	Mass [5] (g)	Vol [6] (mL)	Lf$_{opt}$ [7] (cm)	Lf$_{nom}$ [8] (cm)	Lt$_{nom}$ [9] (cm)	Lmt [10] (cm)	Ls$_{nom}$ [11] (μm)	PCSA [12]
PMJ_L4BLaCaR_PvsIBVeCrR	13	P	Lc1/3	3.3	3.128	7.305	6.253	3.272	9.524	2.140	0.428
PMJ_L4BLaCaR_PvsIBVeMiR	14	P	Lc2/3	4.3	4.105	9.588	8.207	3.272	11.47	2.140	0.428
PMJ_L4BLaCaR_PvsIBVeCaR	15	P	Lc3/3	5.0	4.705	10.987	9.405	3.272	12.67	2.140	0.428
PMJ_L5BLaCaR_PvsIBVeCrR	16	P	Lc1/3	1.8	1.718	4.012	3.434	3.272	6.706	2.140	0.428
PMJ_L5BLaCaR_PvsIBVeMiR	17	P	Lc2/3	2.8	2.663	6.218	5.323	3.272	8.594	2.140	0.428
PMJ_L5BLaCaR_PvsIBVeCaR	18	P	Lc3/3	3.5	3.268	7.633	6.534	3.272	9.805	2.140	0.428
PMJ_L6BLaCaR_PvsIBVeCrR	19	P	Lc1/3	0.6	0.588	1.373	1.176	3.272	4.447	2.140	0.428
PMJ_L6BLaCaR_PvsIBVeMiR	20	P	Lc2/3	1.5	1.392	3.250	2.782	3.272	6.054	2.140	0.428
PMJ_L6BLaCaR_PvsIBVeCaR	21	P	Lc3/3	2.1	1.988	4.642	3.974	3.272	7.246	2.140	0.428
PMJ_L7BLaCaR_PvsIBVeCrR	22	P	Lc1/3	0.0	0.000	0.000	0.000	3.072	3.056	2.140	0.428
PMJ_L7BLaCaR_PvsIBVeMiR	23	P	Lc2/3	0.4	0.375	0.877	0.750	3.272	4.022	2.140	0.428
PMJ_L7BLaCaR_PvsIBVeCaR	24	P	Lc3/3	1.0	0.916	2.140	1.832	3.272	5.103	2.140	0.428
M11 QuadratusLumborum QL-L				**27.0** [S]	**25.484**	**18.413**				**2.500** [D]	**1.384** [S]
QL_L4TPVeLaL_L5TPVeLaL	1	P	P	3.3	3.134	2.265	2.265	0.500	2.765	2.500	0.170
QL_L5TPVeLaL_L6TPVeLaL	2	P	P	3.1	2.907	2.101	2.101	0.500	2.601	2.500	0.158
QL_L6TPVeLaL_L7TPVeLaL	3	P	P	3.5	3.326	2.403	2.403	0.500	2.903	2.500	0.181
QL_L7TPVeLaL_PvsMIWVeCrL	4	P	P	3.9	3.717	2.686	2.686	0.500	3.186	2.500	0.202
QL_L4TPVeMiL_L5TPVeMiL	5	P	P	3.7	3.509	2.535	2.535	0.500	3.035	2.500	0.191
QL_L5TPVeMiL_L6TPVeMiL	6	P	P	3.4	3.195	2.309	2.309	0.500	2.809	2.500	0.174
QL_L6TPVeMiL_L7TPVeMiL	7	P	P	3.7	3.492	2.523	2.523	0.500	3.023	2.500	0.190
QL_L7TPVeMiL_PvsMIWVeCaL	8	P	P	2.3	2.203	1.592	1.592	0.500	2.092	2.500	0.120

Muscle [1] (MuscleName_Origin_Insertion)	E# [2]	Ori Info [3]	Ins Info [4]	Mass [5] (g)	Vol [6] (mL)	Lf_{opt} [7] (cm)	Lf_{nom} [8] (cm)	Lt_{nom} [9] (cm)	Lmt [10] (cm)	Ls_{nom} [11] (μm)	PCSA [12]
M11 QuadratusLumborum QL-R				**26.7**[S]	**25.206**	**18.213**				**2.500**[D]	**1.384**[S]
QL_L4TPVeLaR_L5TPVeLaR	1	P	P	2.9	2.698	1.949	1.949	0.500	2.449	2.500	0.148
QL_L5TPVeLaR_L6TPVeLaR	2	P	P	3.4	3.256	2.353	2.353	0.500	2.853	2.500	0.179
QL_L6TPVeLaR_L7TPVeLaR	3	P	P	3.2	3.059	2.210	2.210	0.500	2.710	2.500	0.168
QL_L7TPVeLaR_PvsMIWVeCrR	4	P	P	4.1	3.845	2.778	2.778	0.500	3.278	2.500	0.211
QL_L4TPVeMiR_L5TPVeMiR	5	P	P	3.3	3.134	2.265	2.265	0.500	2.765	2.500	0.172
QL_L5TPVeMiR_L6TPVeMiR	6	P	P	3.5	3.321	2.399	2.399	0.500	2.899	2.500	0.182
QL_L6TPVeMiR_L7TPVeMiR	7	P	P	3.7	3.525	2.547	2.547	0.500	3.047	2.500	0.194
QL_L7TPVeMiR_PvsMIWVeCaR	8	P	P	2.5	2.368	1.711	1.711	0.500	2.211	2.500	0.130
M12 GluteusSuperficialis GS-L				**24.4**	**22.993**	**6.573**				**2.537**	**3.498**
GS_SacLSCLS2_PvsTRL	1	P	P	10.1	9.571	2.736	2.776	2.375	5.151	2.537	1.456
GS_SacLSCLS3_PvsTRL	2	P	P	7.7	7.248	2.07	2.103	2.375	4.478	2.537	1.103
GS_SacTPLaLCa1_PvsTRL	3	P	P	6.5	6.174	1.765	1.791	2.375	4.166	2.537	0.939
M12 GluteusSuperficialis GS-R				**24.4**	**22.993**	**6.461**				**2.537**	**3.559**
GS_SacLSCRS2_PvsTRR	1	P	P	9.7	9.184	2.581	2.619	2.375	4.994	2.537	1.186
GS_SacLSCRS3_PvsTRR	2	P	P	7.6	7.172	2.015	2.045	2.375	4.420	2.537	1.186
GS_SacTPLaRCa1_PvsTRR	3	P	P	7.0	6.637	1.865	1.893	2.375	4.268	2.537	1.186
M13 Piriformis PF-L				**9.3**	**8.801**	**2.470**				**2.473**	**3.563**
PF_SacTPLaLCa1_PvsTRL	1	P	P	4.1	3.840	1.078	1.066	3.100	4.166	2.473	1.554
PF_SacLSCLS3_PvsTRL	2	P	P	5.3	4.961	1.393	1.378	3.100	4.478	2.473	2.008
M13 Piriformis PF-R				**9.3**	**8.801**	**2.515**				**2.473**	**3.500**
PF_SacTPLaRCa1_PvsTRR	1	P	P	4.4	4.131	1.180	1.168	3.100	4.268	2.473	1.643
PF_SacLSCRS3_PvsTRR	2	P	P	4.9	4.670	1.334	1.320	3.100	4.420	2.473	1.857

1 Muscle: Muscle number, name and abbreviation. Muscle element description: (Abbreviation _ Origin node _ Insertion node).
Node describes affiliated bone segment and abbreviated description of node position.

2 E#: Number of representative muscle elements for the muscle group (actuator).

3 Ori Info: Description of type of origin attachment site (point (P), straight line (Ls), and curved line (Lc).
Additional description of node number from total nodes representing the muscle element, e.g. 1/2 = Node 1 of 2.

4 Ins Info: Description of type of origin attachment site (P, Ls, Lc). Additional description of node number from total nodes representing the muscle element, e.g. Ls attachment site represented by 2 nodes, i.e. 1/2 = Node 1 of 2.

5 Mass: Muscle mass (g)

6 Vol: Muscle volume (cm^3)

7 Lf_{opt}: Optimal muscle fibre length (cm) ($Lf_{opt} = Lf_{nom} / Ls_{nom} * Ls_{opt\ (canine)}$)
N.B. $Ls_{opt\ (canine)}$ = optimum canine sarcomere length (2.5 μm)

8 Lf_{nom}: Nominal muscle fibre length (cm)

9 Lt_{nom}: Nominal tendon length (cm)

10 Lmt: Muscle-tendon element length ($Lmt = Lf_{nom} + Lt_{nom}$)

11 Ls_{nom}: Nominal sarcomere length (μm)

12 PCSA: physiological cross-sectional area ($PCSA = (m / \rho_{canine}) / Lf_{opt} = vol / Lf_{opt}$)
N.B. ρ_{canine} = uniform canine muscle tissue density assumed (1.059 g/cm^3)

N.B. Data measured, expect if marked as scaled (^{S}) or deduced (^{D})

4.7 Ligament parameters

Ligament input parameters were defined in Table 4.8 to model ligament properties of stiffness (k) and strain (eps) as scaled from human ligament studies.

Table 4.8. Modelling of spinal ligament input parameters of stiffness and strain.

Ligament Name (abbreviation & full title)		Input Parameter	L4-L5	L5-L6	L6-L7	L7-Sacrum
LVL	ventral longitudinal ligament	Stiffness (k)	20.8	39.5	40.5	13.2
		Strain (eps)	0.136	0.091	0.124	0.078
LDL	dorsal longitudinal ligament	Stiffness (k)	36.6	10.6	25.8	21.8
		Strain (eps)	0.031	0.044	0.035	0.042
LIS	interspinous ligament	Stiffness (k)	9.6	18.1	8.7	16.3
		Strain (eps)	0.143	1.268	0.243	1.147
LSS	supraspinous ligament	Stiffness (k)	24.8	34.8	18.0	17.8
		Strain (eps)	0.196	0.529	0.295	0.320
LY	yellow ligament	Stiffness (k)	25.1	34.5	27.2	20.2
		Strain (eps)	0.080	0.196	0.283	0.231
LIT	Intertransverse ligament	Stiffness (k)	50.0	50.0	50.0	50.0
		Strain (eps)	0.044	0.044	0.044	0.044

4.8 Joint geometry

Representative joint node coordinates for the intervertebral, lumbo-sacral, and sacroiliac joints were interpolated from the positions of two joint nodes on adjacent bone segments (table 4.9). The joint geometry (Table 4.9) of these spherical joints in the AMS was estimated across three rotational axes from the total canine joint range of motion in the literature, with the positive and negative motion percentages of the complete range of motion applied from human data.

Table 4.9. Joint node positions and bone node positions (X, Y, Z) with respect to the model global reference frame (in mm).

Joint	Joint Node Position	Bone	Bone Node Position
L4 - L5	107.1975, -11.1656, 0.9195921	L4 caudal	108.677, -11.5985, 1.164063
		L5 cranial	105.718, -10.73271, 0.6751207
L5 - L6	75.99545, -10.31086, 0.540189	L5 caudal	77.48854, -10.57274, 0.5097031
		L6 cranial	74.50237, -10.04898, 0.5706748
L6 - L7	46.60632, -10.30367, -0.5392731	L6 caudal	48.13061, -10.04165, -0.5584543
		L7 cranial	45.08203, -10.56568, -0.5200918
L7 - Sacrum	20.20014, -9.97063, -1.08893	L7 caudal	21.96424, -10.49104, -0.6467101
		S cranial	18.14262, -9.501943, -2.026449
Sacrum - Ilium	3.260489, -3.530237, 5.898203	L sacrum	2.902843, -7.712077, -24.5259
		R sacrum	3.36431, -7.259637, 20.46026

Table 4.10. Joint range of motion (ROM) with respect to the model global reference frame (in mm).

Joint	Joint Node Position	FE (°) ROM [1]	FE (°) [2]	AR (°) ROM	AR (°) [3]	LB (°) ROM	LB (°) [4]
L4 - L5	107.1975, -11.1656, 0.9195921	7.2	-4.25	1.9	-0.95	19.0	-9.5
			+2.95		+0.95		+9.5
L5 - L6	75.99545, -10.31086, 0.540189	6.8	-4.02	0.8	-0.4	4.1	-2.05
			+2.78		+0.4		+2.05
L6 - L7	46.60632, -10.30367, -0.5392731	11.8	-6.97	0.7	-0.35	7.1	-3.55
			+4.83		+0.35		+3.55
L7 - Sacrum	20.20014, -9.97063, -1.08893	37.0	-18.65	2.0	-1.0	9.5	-4.75
			+18.35		+1.0		+4.75
Sacrum - Ilium	3.260489, -3.530237, 5.898203	2.0	-1.0	0	0	0	0
			+1.0		0		0

[1] T.ROM = Total joint range of motion

[2] FE = Flexion (-) and extension (+)

[3] AR = Axial rotation: from caudal aspect moves anti-clockwise (-) and clockwise (+)

[4] LB = Lateral bending: from dorsal aspect right (-) and left (+)

4.9 Kinematic modelling

Inverse dynamics analyses were conducted to calculate force and strength outputs from the canine model. Prior to conducting inverse dynamics operations, the lumbo-sacral joint was isolated, with the normal spine rhythm suppressed. This was done in the interest of avoiding interference from other joint movements confounding the muscle of interest for this trial, sacrocaudalis dorsalis medialis, which crossed only the lumbo-sacral joint.

The second phase of the inverse dynamics simulations was a sensitivity analysis conducted through incremental alterations of a single selected muscle input parameter. This was achieved by altering the PCSA input values for the sarcomere length adjustments, and additionally the muscle fibre length and slack tendon lengths for the muscle fibre length adjustments. PCSA alterations were required for both incremental trials as sarcomere length and muscle fibre lengths are both contributing factors in the calculation of PCSA. The sensitivity analysis was conducted across the two independent trials for force and strength outputs. For both of the selected outputs, the two trials of muscle fibre length to tendon ratio and muscle sarcomere length were carried out with alterations of 1 mm and 0.1 μm, respectively. In addition, all graphs on sensitivity analysis trials had margins of 5% around the true values, with each margin representing a 2.5% output increase or decrease from the true measured value.

4.9.1 Inverse dynamics force operation

Force outputs were observed in only one direction from the neutral position across all ranges of motion. The largest forces were consistently experienced at or near the point furthest from the neutral position.

Figure 4.1. Inverse dynamic output property of force plotted against muscle-tendon element length for the left sacrocaudalis dorsalis medialis muscle with spine motion isolated to permit lumbo-sacral joint movement only. Flexion and extension (A), lateral bending (B), and axial rotation (C) movements are displayed with the central vertical line indicating the neutral spine position.

Figure 4.1

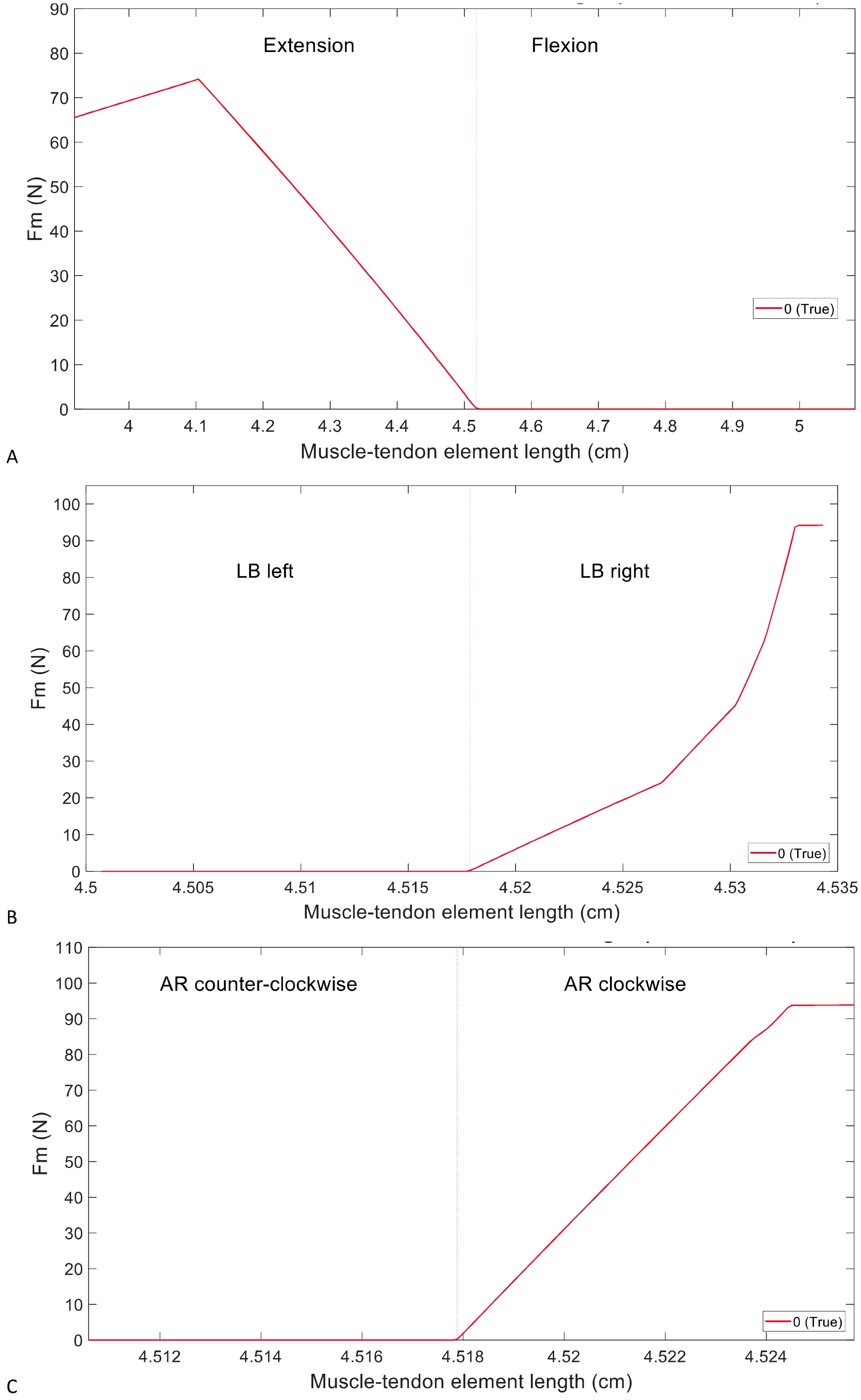
Extension
Flexion
Fm (N)
0 (True)
Muscle-tendon element length (cm)
A
LB left
LB right
Fm (N)
0 (True)
Muscle-tendon element length (cm)
B
AR counter-clockwise
AR clockwise
Fm (N)
0 (True)
Muscle-tendon element length (cm)
C

4.9.1.1 Inverse dynamics force sensitivity analysis of muscle length

The sensitivity analysis shows incremental adjustments of the measurement accuracy of 1 mm for data collection of muscle fibre length during a dissection. All ranges of motion required nominal muscle fibre measurements to have an error of no greater than 1 mm to maintain force outputs within 5% of the force output for the true measured nominal fibre length.

Figure 4.2. Inverse dynamic output property of force plotted against muscle-tendon element length for the left sacrocaudalis dorsalis medialis muscle with spine motion isolated to the permit lumbo-sacral joint movement only. Flexion and extension (A), lateral bending (B), and axial rotation (C) movements are displayed with the central vertical line indicating the neutral spine position. Muscle fibre length (Lf nom) is altered by increments of 1 mm from the true measured muscle fibre length, simulating both a decrease and increase of muscle fibre to tendon ratio.

Figure 4.2

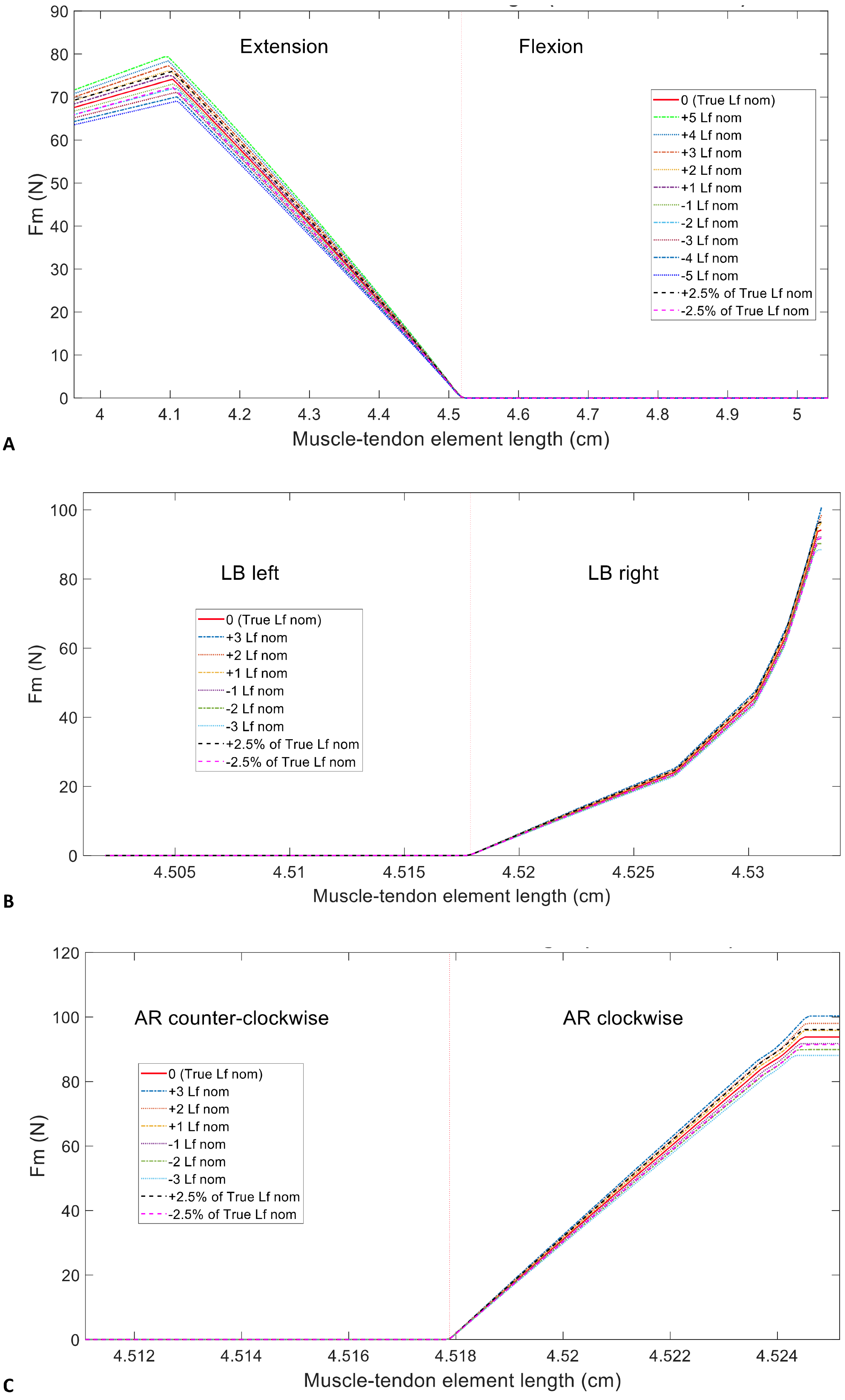

Extension
Flexion
Fm (N)
Muscle-tendon element length (cm)
0 (True Lf nom)
+5 Lf nom
+4 Lf nom
+3 Lf nom
+2 Lf nom
+1 Lf nom
-1 Lf nom
-2 Lf nom
-3 Lf nom
-4 Lf nom
-5 Lf nom
+2.5% of True Lf nom
-2.5% of True Lf nom
0
10
20
30
40
50
60
70
80
90
4
4.1
4.2
4.3
4.4
4.5
4.6
4.7
4.8
4.9
5
A
LB left
LB right
Fm (N)
Muscle-tendon element length (cm)
0 (True Lf nom)
+3 Lf nom
+2 Lf nom
+1 Lf nom
-1 Lf nom
-2 Lf nom
-3 Lf nom
+2.5% of True Lf nom
-2.5% of True Lf nom
0
20
40
60
80
100
4.505
4.51
4.515
4.52
4.525
4.53
B
AR counter-clockwise
AR clockwise
Fm (N)
Muscle-tendon element length (cm)
0 (True Lf nom)
+3 Lf nom
+2 Lf nom
+1 Lf nom
-1 Lf nom
-2 Lf nom
-3 Lf nom
+2.5% of True Lf nom
-2.5% of True Lf nom
0
20
40
60
80
100
120
4.512
4.514
4.516
4.518
4.52
4.522
4.524
C

4.9.1.2 Inverse dynamics force sensitivity analysis of sarcomere length

The sensitivity analysis shows incremental adjustments of the measurement accuracy of 0.1 µm for data collection of muscle fibre length during microscopic examination of the muscles excised in a dissection. All ranges of motion exceeded the threshold with a single variation of 0.1 µm at the maximum values.

Figure 4.3. Inverse dynamic output property of force plotted against muscle-tendon element length for the left sacrocaudalis dorsalis medialis muscle with spine motion isolated to the permit lumbo-sacral joint movement only Flexion and extension (A), lateral bending (B), and axial rotation (C) movements are displayed with the central vertical line indicating the neutral spine position. Muscle sarcomere length (Ls) is altered by increments of 0.1 µm from the true measured muscle sarcomere length, simulating both a decrease and increase from the true value.

Figure 4.3

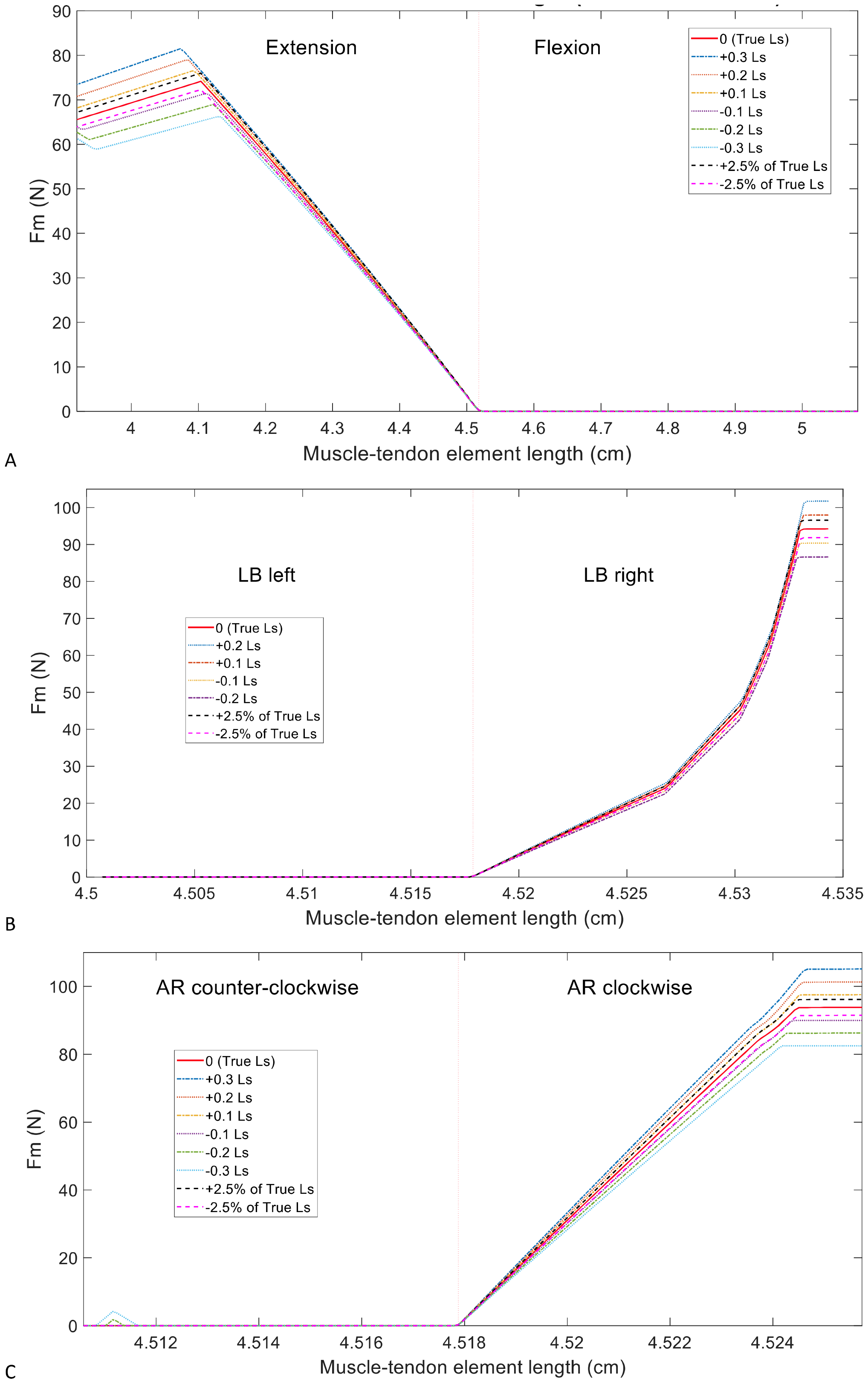
Extension
Flexion
0 (True Ls)
+0.3 Ls
+0.2 Ls
+0.1 Ls
-0.1 Ls
-0.2 Ls
-0.3 Ls
+2.5% of True Ls
-2.5% of True Ls
Fm (N)
0
10
20
30
40
50
60
70
80
90
4
4.1
4.2
4.3
4.4
4.5
4.6
4.7
4.8
4.9
5
Muscle-tendon element length (cm)
A
LB left
LB right
0 (True Ls)
+0.2 Ls
+0.1 Ls
-0.1 Ls
-0.2 Ls
+2.5% of True Ls
-2.5% of True Ls
Fm (N)
0
10
20
30
40
50
60
70
80
90
100
4.5
4.505
4.51
4.515
4.52
4.525
4.53
4.535
Muscle-tendon element length (cm)
B
AR counter-clockwise
AR clockwise
0 (True Ls)
+0.3 Ls
+0.2 Ls
+0.1 Ls
-0.1 Ls
-0.2 Ls
-0.3 Ls
+2.5% of True Ls
-2.5% of True Ls
Fm (N)
0
20
40
60
80
100
4.512
4.514
4.516
4.518
4.52
4.522
4.524
Muscle-tendon element length (cm)
C

4.9.2 Inverse dynamics strength operation

Strength output values were observed to have a linear slope across the full range of motion for all ranges of motion, without alteration through the neutral position. The steepest gradient was that of the flexion and extension graph, with a range of approximately 50 N. The remaining two ranges of motion possessed a range of approximately 1 N.

Figure 4.4. Inverse dynamic output property of strength plotted against muscle-tendon element length for the left sacrocaudalis dorsalis medialis muscle with spine motion isolated to permit lumbo-sacral joint movement only. Flexion and extension (A), lateral bending (B), and axial rotation (C) movements are displayed with the central vertical line indicating the neutral spine position.

Figure 4.4

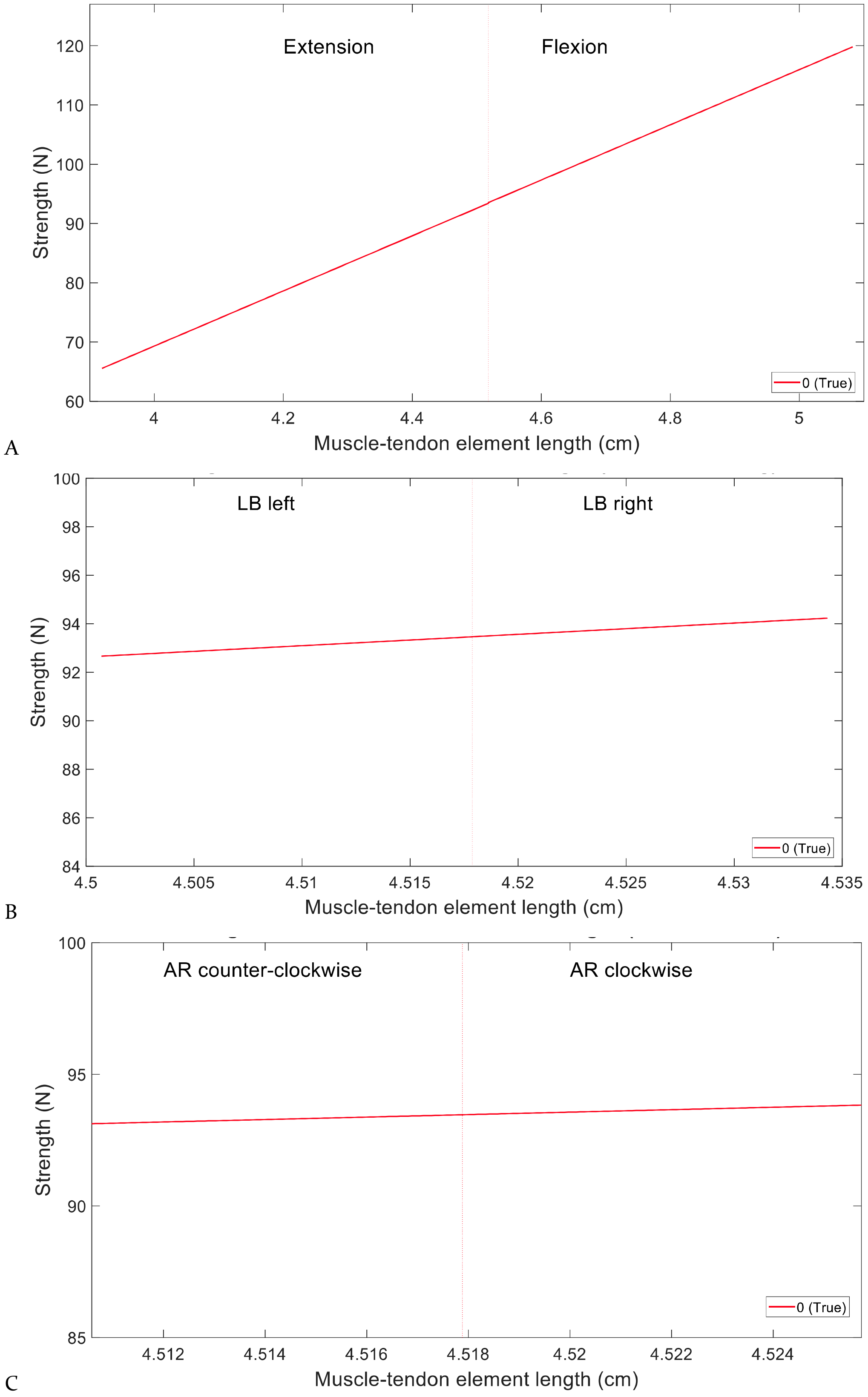
Extension
Flexion
Strength (N)
60
70
80
90
100
110
120
4
4.2
4.4
4.6
4.8
5
0 (True)
Muscle-tendon element length (cm)
A
LB left
LB right
Strength (N)
84
86
88
90
92
94
96
98
100
4.5
4.505
4.51
4.515
4.52
4.525
4.53
4.535
0 (True)
Muscle-tendon element length (cm)
B
AR counter-clockwise
AR clockwise
Strength (N)
85
90
95
100
4.512
4.514
4.516
4.518
4.52
4.522
4.524
0 (True)
Muscle-tendon element length (cm)
C

4.9.2.1 Inverse dynamics strength sensitivity analysis of muscle length

The sensitivity analysis shows incremental adjustments of the measurement accuracy of 1 mm for data collection of muscle fibre length during a dissection. All ranges of motion required nominal muscle fibre measurements to generally have an error of no greater than 1 mm to maintain strength outputs within 5% of the strength output of the true measured nominal fibre length. Flexion measures of ± 1 mm were observed to edge across the 5% margins with full flexion of the specimen, indicating a greater accuracy required with no margin for error.

Figure 4.5. Inverse dynamic output property of strength plotted against muscle-tendon element length for the left sacrocaudalis dorsalis medialis muscle with spine motion isolated to the permit lumbo-sacral joint movement only. Flexion and extension (A), lateral bending (B), and axial rotation (C) movements are displayed with the central vertical line indicating the neutral spine position. Muscle fibre length (Lf nom) is altered by increments of 1 mm from the true measured muscle fibre length, simulating both a decrease and increase of muscle fibre to tendon ratio.

Figure 4.5

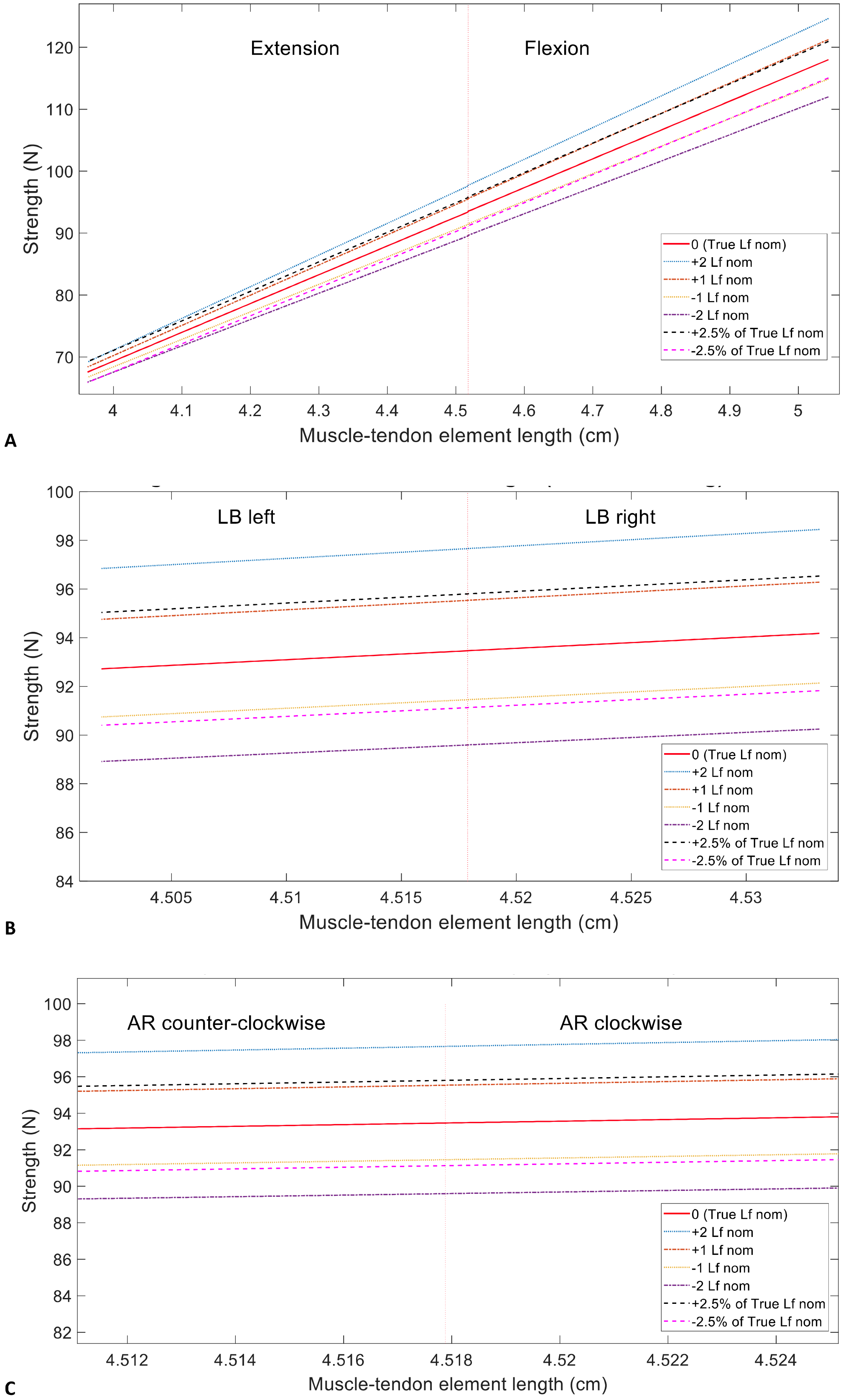
Extension
Flexion
Strength (N)
120
110
100
90
80
70
4
4.1
4.2
4.3
4.4
4.5
4.6
4.7
4.8
4.9
5
Muscle-tendon element length (cm)
0 (True Lf nom)
+2 Lf nom
+1 Lf nom
-1 Lf nom
-2 Lf nom
+2.5% of True Lf nom
-2.5% of True Lf nom
A
LB left
LB right
Strength (N)
100
98
96
94
92
90
88
86
84
4.505
4.51
4.515
4.52
4.525
4.53
Muscle-tendon element length (cm)
0 (True Lf nom)
+2 Lf nom
+1 Lf nom
-1 Lf nom
-2 Lf nom
+2.5% of True Lf nom
-2.5% of True Lf nom
B
AR counter-clockwise
AR clockwise
Strength (N)
100
98
96
94
92
90
88
86
84
82
4.512
4.514
4.516
4.518
4.52
4.522
4.524
Muscle-tendon element length (cm)
0 (True Lf nom)
+2 Lf nom
+1 Lf nom
-1 Lf nom
-2 Lf nom
+2.5% of True Lf nom
-2.5% of True Lf nom
C

4.9.2.2 Inverse dynamics strength sensitivity analysis of sarcomere length

The sensitivity analysis shows incremental adjustments of the measurement accuracy of 0.1 µm for data collection of sarcomere length during microscopic examination of the muscles excised in a dissection. All ranges of motion exceeded the threshold with a single variation of 0.1 µm at the maximum values.

Figure 4.6. Inverse dynamic output property of strength plotted against muscle-tendon element length for the left sacrocaudalis dorsalis medialis muscle with spine motion isolated to the permit lumbo-sacral joint movement only. Flexion and extension (A), lateral bending (B), and axial rotation (C) movements are displayed with the central vertical line indicating the neutral spine position. Muscle sarcomere length (Ls) is altered by increments of 0.1 µm from the true measured muscle sarcomere length, simulating both a decrease and increase from the true value.

Figure 4.6

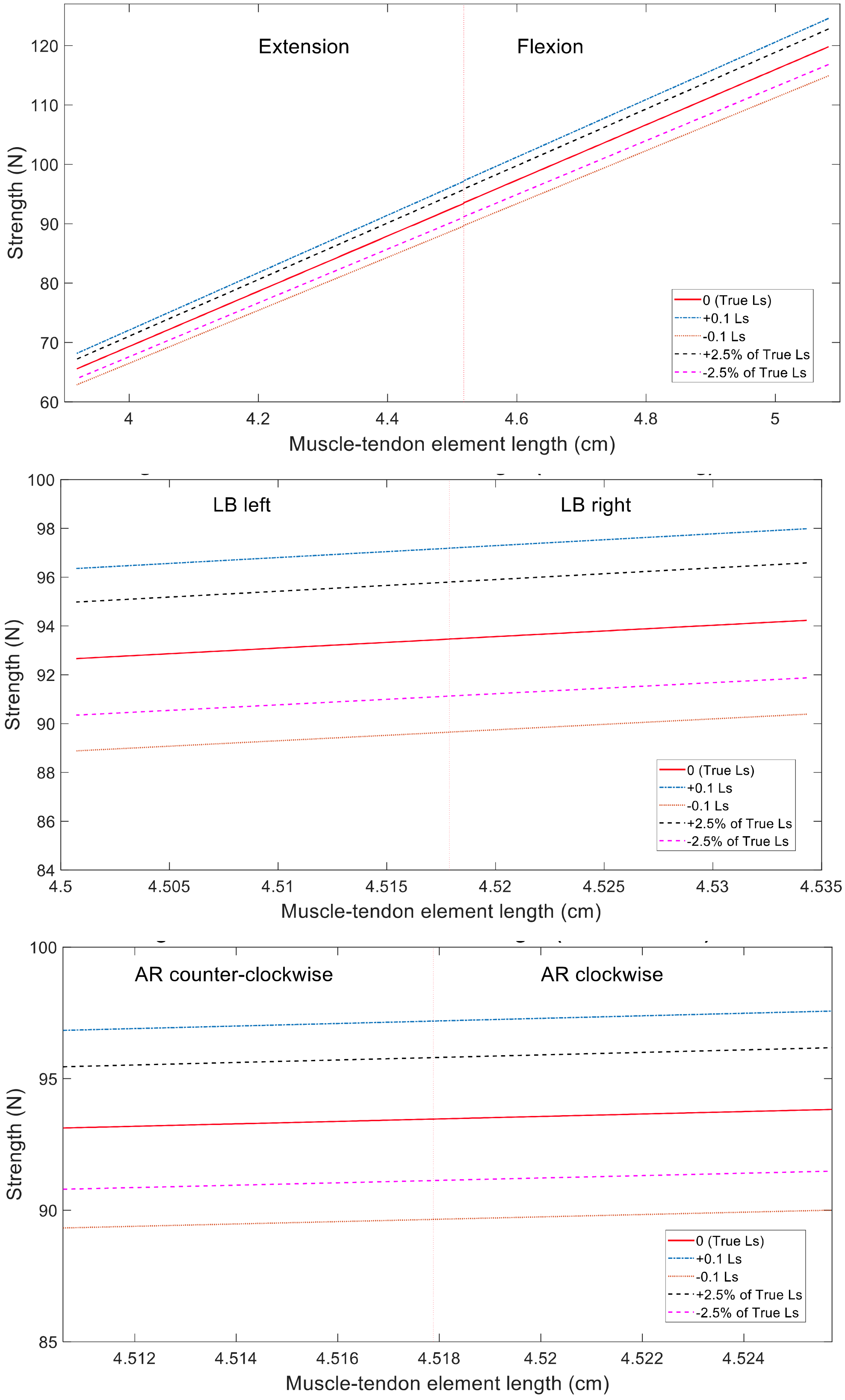
Extension
Flexion
Strength (N)
Muscle-tendon element length (cm)
60
70
80
90
100
110
120
4
4.2
4.4
4.6
4.8
5
0 (True Ls)
+0.1 Ls
-0.1 Ls
+2.5% of True Ls
-2.5% of True Ls
A
LB left
LB right
84
86
88
90
92
94
96
98
100
4.5
4.505
4.51
4.515
4.52
4.525
4.53
4.535
B
AR counter-clockwise
AR clockwise
85
90
95
100
4.512
4.514
4.516
4.518
4.52
4.522
4.524
C

5. DISCUSSION

5.1 General discussion

The primary aim of this research project was to develop a preliminary three-dimensional musculoskeletal and patient-specific model of a single German shepherd lumbo-sacral spine. The model developed functions as intended and aptly fulfilled its role as a pilot model. A critical requirement for the model was for it to be a template scalable to the medical images from subsequent GSDs. The prerequisite for future scaling to be permitted was the application of a scaling law to bones and muscle attachment sites from the template of the initial cadaver model to the target model of a subsequent GSD. Due to vast variations between dog breeds, this preliminary model is only applicable to GSDs.

Key findings from the study revolved around identifying how critical the accuracy of input variables were to the inverse dynamics output data. While the model input parameters tested were found to be very sensitive, the precise implications of discrepancies in data collection for model input parameters needs further investigation for future models. Overall, achieving reliable inverse dynamics results requires the hugely comprehensive task of obtaining a complete and accurate definition of all elements in the model.

The condition of the available GSD specimen contributed to limiting factors in this study. The time in frozen storage exceeded two years and, while preferable to fixation, the morphology of the skeletal muscle is likely to be in less than optimal condition after this prolonged period. The section through the seventh lumbar vertebrae also hindered data collection with an intact specimen better suited to provide the complete dataset required. Lack of access to further available GSD cadavers also restricted the depth of data available for collection. It is essential to have access to multiple cadavers in collecting some data, for example, ligaments stress and strain, for which collection of data from one ligament destroys surrounding tissues due to the nature of testing required. While the model is built around musculoskeletal conformations of a single GSD, access to multiple GSD cadavers would be preferable to compile a sound and reliable dataset for the generic pilot dog model. An additional restriction experienced throughout this study was the approach applied to gathering musculoskeletal data parameters. Positions of attachment were obtained from medical images of the specimen, however, specialised tools to capture three-dimensional positions such as the palpator (Pronk & Vanderhelm, 1991), would enable a more efficient method of gathering three-dimensional coordinates during the dissection. Post-processing tools and software proven beneficial in human biomechanical modelling would likely also be advantageous in the extension of this canine modelling project.

Limitations of the ability to collect GSD-specific data in this study consequentially impacted on the ability of modelling, for example, the quality of muscle representations. AnyBody has three muscle models available of varying levels of complexity and range of biologically realistic outputs, increasing from the one-element to three-element models. Due to the available data and the requirement for testing of muscle fibre length and sarcomere length, the two-element model was selected for use in the preliminary development of this model. The preferred choice would be the comprehensive three-element model, a Hill-type muscle model with representation of active properties of muscle fibres, tendon elasticity, and passive stiffness of muscle fibres. It was not, however, a feasible choice due to the lack of necessary input parameters required, including the ratio of fast-twitch to slow-twitch fibres, tendon serial-elastic and muscle parallel-elastic data, and other inputs relating to force and muscle fibre details.

Assumptions and simplifications of this study, to be rectified in future studies, are listed as follows. The weight of the limbs and remainder of the dog were neglected. Ventral muscles were approximated to represent abdominal muscles and provide necessary resistance to the dorsal spinal muscles. The sacroiliac joint was restricted to movements of flexion and extension due to the representative central joint node, although this is not of large consequence as the sacroiliac joint is primarily subjected to flexion and extension through caudal spine movement in gait.

5.2 Discussion of findings

5.2.1 Cadaver measurements

Most of the canine muscle, tendon and ligament anatomical descriptions viewed and recorded in the dissection concurred with data available in the literature of veterinary textbooks. Parameters measured from the specimen were of critical importance to the final model, with many of the parameters recorded not identified in the literature of GSDs.

Limitations of data collection arose from the cadaver having been sectioned through L7 prior to the dissection, restricting the number of parameters collected, namely muscle and tendon element lengths, mass, and volume. However, previously cut, hence incomplete, muscles were still capable of providing the essential contribution to the dataset of sarcomere length information.

5.2.2 Histology measurements

Histology provided sarcomere length measurements essential to the AMS muscle input parameters, which were found to be largely unavailable in the literature regarding canine specimens, and in particular for GSDs. Furthermore, sourcing these data from a single specimen, the source of data for the majority of the model input parameters provided a consistent and unique dataset specific to this canine subject.

The number of 100 individual sarcomeres measured for each muscle accounted for variability between fibres in that sample. The intramuscular difference in minimum and maximum lengths of the 10 consecutive sarcomere lengths ranged from 0.133 μm of m. iliacus to 0.681 μm of m. longissimus lumborum. Variability may be the result of the measured fibre being from a peripheral rather than core muscle biopsy, or a distortion of the fibre observed on the image capture. The intermuscular average range of the 10 units of 10 consecutive sarcomere lengths was recorded as 0.389 μm. This range is of relevance to the sensitivity analysis that altered sarcomere length and will be addressed at para 5.2.9. No differences were expected due to the differences between slow and fast twitch muscle fibres due to the primarily epaxial muscles with largely postural support roles.

The accuracy of histological measurements was attributed to the calibration of the light microscope and image capturing software and negligible limitations of the fibre disruption from freezing and shrinkage of less than 5% from submersion in formalin. Any variability existing is likely common to all fibres and of minimal effect.

5.2.3 Bony landmarks

Recommended improvements to identifying bony landmarks on the cadaver are to insert discrete pins on prominent bony landmarks prior to capturing CT data. These prominent bony landmarks should be selected on the basis of their ease of identification in radiographs, which is pivotal in determining muscle attachment sites from anthropometric scaling of subsequent dogs in the future. Inserting landmark pins creates a set of reference frame markers across all datasets, easily identifiable in both the intact specimen, and individual bone segments medical images. The importance of this is to enable efficient modelling reconstruction of the individual bone segments back into their correct anatomical orientations and alignments.

Limitations of landmark positions obtained from the specimen dissection in this study pertained to the misalignment of prominent bony landmark positions between the dissection coordinates and those obtained from medical imaging. The Qualisys coordinates were not used for this final model due to the selection of bony landmarks on the specimen not aligning with those from the CT images. For future reference, it is recommended to establish bony landmark positions by inserting multiple pins into each bone to create landmarks common to both medical imagery and dissection coordinates. This enables Qualisys markers to be positioned on the existing pins enabling all coordinate data collected from the dissection to be applicable to the CT images and rendered useful in the final model by marrying up the landmark pins' positions. Furthermore, fixing the specimen in a frame prior to establishing a single reference frame is advised to eliminate the occurrence of multiple confounding dissection reference frames.

5.2.4 Bone segment origins

While bone segment origins (0,0,0) are not imperative to the results of the study, they are of use to future studies to analyse bone orientation in relation to their adjacent segments. In conjunction with inertial parameters these coordinates may be used to determine every coordinate used in the model in both global and local reference frames. Coordinates in the global model reference frame enable successive measurements between, for example, two nodes on different bone segments to determine the distance between them.

5.2.5 Inertial parameters

Anthropometric measurements for estimation of inertial parameters as seen in Carbone et al. (2015) include: segment mass, centre of mass, principal axis of inertia and principal moment of inertia calculated in SolidWorks based on segmented bone, muscle and fat volumes. These volumes were extracted from MRI data with high precision, and are recommended for future studies to improve the accuracy of data for inertia. This higher level of data would not have significantly improved inertial effects due to the low angular accelerations experienced in this region, however, they will be of importance to segments subjected to significant accelerations, such as the pelvic limb. Additionally, the true centre of mass should be defined in future studies, considering distribution and densities of surrounding muscle, fat and other soft tissues, as opposed to the bone centre of mass used in this study. This would need to be determined experimentally.

5.2.6 Muscle parameters

The dataset of muscle parameters recorded from both the dissection and analysis of medical imagery will be a significant contribution to the literature.

Prior to modelling, the muscles identified as relevant to the model were deconstructed into representative elements, as seen in the TLEM 2.0 study (Carbone et al., 2015). When subdividing the muscle into elements, values of mass, for example, were divided among the individual elements. For instance, three nodes represented the curved-line insertion of psoas minor on the arcuate line of the pelvis (Van Der Helm & Veenbaas, 1991). Each of these nodes defined the insertion point of a muscle element partially representing psoas minor, whose combined mass equalled the psoas minor complete mass.

Implications of muscle parameters included the dissection and medical imaging bony landmarks not marrying up, as discussed at para 5.2.3, and the specimen lacking lumbar vertebrae remaining on the specimen after sectioning. To rectify this situation, all nodes were successfully obtained by acquisition in SolidWorks from medical image files with guidance from the literature to represent musculo-tendon and ligament attachment sites.

As not all parameters from this dataset were obtainable through the available GSD cadaver, some data such as PCSA were sourced from the literature (Horsman et al., 2007) and scaled by mass where it was felt that it was transferrable to the GSD. Absent, but required, data parameters essential to the functioning of the model were sourced through the next best means of canine or human musculo-skeletal datasets. Epaxial muscle PCSA data was applied from a muscle that possessed all parameters measured from the GSD cadaver, and applied to other epaxial muscles lacking the full dataset parameters.

Scaling of muscle parameters by mass from human data presented problems because of the different postures of biped and quadruped animals as the postural muscles are expected to vary somewhat. Comparing the morphology of the human and canine epaxial musculature requires caution due to the significant differences between the two skeletal conformations. Overall, the benefit of sourcing some data from other canine and human studies outweighed the cost, and was regarded as acceptable and the best available option for providing valid muscle input values for critical values in this initial canine spinal model. These limitations will not be experienced with access to intact GSD specimens for dissection for future GSD modelling projects.

5.2.7 Ligament parameters

In this study, the required input parameters of ligament stiffness and strain were not attainable, therefore taken from scaled human parameters (Chazal et al., 1985; Pintar et al., 1992), which was regarded sufficient for the generation of a preliminary model. Future consideration to improve the accuracy of input parameters to represent canine ligament behaviours would be to include collection of GSD ligament parameters through testing to obtain load-deformation curves. Multiple fresh specimens would be required for ligament testing to add the required detail due to the destructive effects on surrounding tissues, and this alone would be a comprehensive project.

5.2.8 Joint geometry

Joint nodes were represented as the equidistant point between single nodes on each of two adjacent bone segments; for example, the lumbo-sacral joint node was calculated from the mid-point of the central sacrum base and seventh lumbar vertebral central body. These points are not, however, centres of rotation determined experimentally but represent convenient points around which contiguous segments rotate in the three planes.

Future work to refine the model will include obtaining the actual behaviours of segments around joints from the specimen prior to dissection, with medical imaging captured from the intact dog indicating the full ranges of motion in the orientation of three orthogonal rotational axes with full movement of flexion and extension, lateral bending, and axial rotation. The centre of rotation of each joint may then be calculated from the motion patterns of the segments.

Joint range of motion may also be recorded using the Qualisys motion capture camera system after excision of all muscles with ligaments remaining intact, with the movement restrained only by bone contact, ligaments or intervertebral discs. Lumbo-sacral and lumbar intervertebral synovial and facet joints would require manipulation by hand to determine their ranges of motion. Bone-mounted markers could be tracked in three-dimensions to determine the range of joints in the anatomical planes.

5.2.9 Inverse dynamics assessments

Once built, the model tested muscle input parameters of fibre length and sarcomere length by subjecting them to incremental alterations. This enabled the relevance of the input parameters to be determined and the impact of any variation from the true measured value on the inverse dynamic outputs to be ascertained. To gauge the effect of varying the input parameters, an arbitrary deviation of ± 2.5% from the true measured muscle value was applied throughout the entire range of motion, creating a total threshold of 5% around the true output value. The function of the sensitivity analysis was to test the direct impact of varying input muscle parameters on the inverse dynamics output with reference to the established threshold.

Altering the true measured muscle fibre length and sarcomere length was shown, as expected, to affect inverse dynamics outputs of force and strength. Increasing sarcomere length decreased the optimal fibre length, which increased the PCSA, and ultimately increased both force and strength. Increasing muscle fibre length also increased force and strength output, as the passive tendon element was reduced and active muscle element increased to maintain the total muscle-tendon element length.

Values for fibre length and sarcomere length were varied to achieve ± 2.5% changes with force and strength model output values. This threshold of 5% of the true values defined a parameter of acceptable discrepancy when recording cadaver measurements for input parameters, to maintain a limited effect of the variation of inverse dynamics outputs. Input parameters for muscle fibre length were generally small, with minimal margin for error allowed for with measurement accuracy of 1 mm typically required.

In the sensitivity analysis, muscles were activated only in one direction from the neutral position. This allows the activation and allocation of various amounts of work from specific muscles to achieve a moment around two bone segments. When several muscles are viewed simultaneously it is apparent that they are recruited and active to different degrees throughout the progression of the movement. This is apparent in the force-length curve, which is abbreviated due to the muscle's starting length.

Inverse dynamics output graphs of force appear to have the incremental adjustments grouped more tightly around the true measured values than the comparable strength outputs. Upon first viewing, this is misleading due to the different scales and linear gradients between these graphs, however, they have a common measure of only 1 mm adjustments falling within margins surrounding the true value. The sensitivity analysis for the varied sarcomere lengths indicates that sarcomere lengths must be measured precisely to avoid affecting strength outputs. There is some conflict in interpreting these results. For example, a 0.1 μm sarcomere length increase exceeded the + 2.5% margin of the force-length curve, however, the intermuscular average range of the 10 units of 10 consecutive sarcomere lengths was recorded as 0.389 μm. This emphasises the critical effect of the sarcomere length input parameter on the inverse dynamics output values. It also suggests that ± 2.5% threshold for accuracy will be easily exceeded by the range of sarcomere length values observed in the data.

From the above findings in this preliminary investigation it appears that both force and strength output variables are very sensitive to accuracy of muscular input parameters, with small measurement inaccuracies exceeding the 5% threshold of the output. The range observed in this study was the result of a single central muscle biopsy per muscle. It was not necessarily representative of the whole muscle, and it is reasonable to expect values to be more discrepant when sampling from multiple locations across a muscle. Critically, this sensitivity analysis has identified the effect of muscle input variations on output values, and the ramifications of using imprecise muscle input parameters not relevant to an individual muscle.

Considering that small changes in muscle fibre length and sarcomere length cause large changes in force and strength output values, the 5% threshold assigned in this study may indeed be too constraining and unrealistic in practical terms and require expansion to allow for more achievable data collection. Nonetheless, the implications of measurement accuracy of input parameters being highly influential to inverse dynamics output parameters should be kept in mind when gathering data.

Future sensitivity analyses are recommended to explore modifications of other musculoskeletal factors such as bone conformation and tissue attachment site area, and investigate the possibility of determining biologically accurate inverse dynamics output parameters for reliable simulation mimicking conditions experienced in GSD hard and soft tissue elements.

5.3 Future direction and considerations

While many future considerations are previously listed under relevant topics throughout this chapter, the general progression of this research topic is of a broader scope.

The initial objective of this study was to test the lumbo-sacral joint of the GSD, but in the longer term to test the whole spine and pelvic limbs, incorporating all surrounding bony and soft tissue. Realistic gait data obtained via high-speed cameras is then required, as well as data from force platforms to capture environment interactions and forces of activities ranging from normal gait to high-impact movements. A complete model will allow comparison of simulated force and moment values with those obtained from real gait data.

Subsequent modelling of the entire spine and locomotor system will aim to calculate ground reaction forces transmitted through the spine during work done by the limbs from normal gait through to movements of high intensity and impact, as captured by high-speed cameras and force platforms. Predicting this effect on the spine has high relevance and application to police and military working dogs that experience strenuous and high-impact activities throughout their working lives.

Simulations will be enhanced by capturing the electrical activity produced by the skeletal muscles of the dog through electromyography to determine realistic contraction values during various activities and these can be input to the model. Intra-abdominal pressures affecting the spine and its movements would be better represented through the inclusion of abdominal muscles that also contribute substantially to the flexor moment of each vertebral segment. Further investigations are also recommended into contributions of passive and active stiffness elements, optimal postures, and differentiating motion of GSD with and without lumbo-sacral deficits.

These progressions all ultimately lead to the functionality of the model to calculate forces and moments transmitted across joints and determine failure mechanisms, and to identify musculoskeletal conformations that predispose working GSD to injury, debilitating conditions and loss from service. With the forces and torques experienced during various dynamic activities identified, geometric properties of the spine and soft tissue behaviours can be manipulated to evaluate the behaviour of all joints and determine the peak stresses experienced. This will enable examination of the effects of different spinal conformations across dogs, and evaluation of the likelihood of subsequent spinal injury per dog.

Other applications of the advanced model include clinical modelling of the functional outcome of surgical interventions. These can be analysed to investigate implications of procedures such as bridging a joint, and to provide maximal information for a cost-benefit analysis.

A more distant scope for this modelling programme of research also includes application of this modelling technique to other canine breeds, and its use as a powerful orthopaedic tool to diagnose common aliments in working and companion dogs. However, ground-up models of each breed are likely to be required due to the tremendous variation in orthopaedic geometry between breeds.

6. CONCLUSION

The primary objective of this study was to develop a functional biomechanical tool to address the prevalent failure of the lumbo-sacral joint in working GSDs, which can result in their health and welfare being compromised. A working mathematical model now exists of the GSD lumbo-sacral spine capable of simulation studies of the forces and moments around the lumbar and lumbo-sacral bones and joints. It is a subject-specific model that has been build around an individual GSD, however, it is capable of being scaled for future assessment of live GSDs.

Musculoskeletal data was successfully acquired from the dissection of a GSD specimen, providing specific muscle parameters crucial to the workings of the model. These data, which were not identified in any current literature, provided input data values of high integrity, which enabled reliable output parameters specific to the GSD breed. With the purpose of the research being to provide a true and accurate model of articulated elements of the lumbo-sacral spine, the attachment of physiologically valid muscles to anatomically correct points was an essential component in the success of the project.

The biomechanical model developed was also tested for its capabilities in inverse dynamics operations through a sensitivity analysis. This evaluation succeeded in identifying the influence of the muscle input parameters of muscle fibre and sarcomere lengths on the values of inverse dynamics output values of force and strength. The incremental alterations of muscle input parameters also established their significance on model output values, confirming the requirement for precise measurements of these critically important muscle parameters.

This preliminary model is the crucial first stage of this area of research of biomechanical application modelling of the canine spine and limbs. This model will be expanded in future to include the rest of the locomotion system. Ultimately, the contribution from this study will be conducive to improving the wellbeing of working GSDs.

7. APPENDICES

7.1 Appendix I

The following Qualisys camera system datasets provide a greater depth of information than presented in the Results chapter (chapter 4) regarding muscle and ligament data acquired from software analysis of the medical images taken of the intact specimen. This data may be of interest for progressing this GSD model, as well as future biomechanical studies of the canine spine.

Table 7.1. Qualisys camera system reference points and soft tissue points of interest (muscle attachment sites, muscle lines-of-action, muscle-tendon lengths, and muscle fibre direction) as captured during the dissection of the canine specimen. Coordinates were captured with respect to the local reference frame (in mm).

MEASURE		REFERENCE	X	Y	Z
Gluteus superficialis					
LOA	1	RLumbarVentral	-326.145	71.936	73.703
	2	MidLumbarVentral	-314.374	56.092	62.081
	3	LLumbarVentral	-305.885	36.008	68.717
	4	SacrumMidline1	-262.109	78.714	117.622
	5	SacrumMidline2	-216.592	105.482	116.974
	6	LOA 1 (craniodorsal)	-246.260	59.243	98.526
	7	LOA 2 (caudalventral) I(P)	-190.573	42.955	59.520
Origin 1	1	RLumbarVentral	-278.610	227.979	124.744
	2	MidLumbarVentral	-266.250	214.762	109.469
	3	LLumbarVentral	-253.258	195.033	115.407
	4	SacrumMidline1	-220.878	239.570	139.296
	5	SacrumMidline2	-176.903	283.816	107.726
	6	ORIGIN 1	-145.906	206.450	118.206
Origin 2	1	RLumbarVentral	-278.830	229.008	125.203
	2	MidLumbarVentral	-266.576	215.673	110.026
	3	LLumbarVentral	-253.606	195.949	116.123
	4	SacrumMidline1	-221.145	240.648	139.589
	5	SacrumMidline2	-177.483	281.898	107.698
	6	ORIGIN 2	-134.402	216.112	114.042
Origin 3	1	RLumbarVentral	-254.822	247.753	124.509
	2	MidLumbarVentral	-245.505	232.646	109.422
	3	LLumbarVentral	-234.836	211.516	115.320
	4	SacrumMidline1	-195.978	250.491	139.128
	5	SacrumMidline2	-144.948	287.271	108.434
	6	ORIGIN 1	-162.261	250.970	101.015

Table 7.1 Continued

MEASURE		REFERENCE	X	Y	Z
Origin 4	1	RLumbarVentral	-252.210	243.489	124.991
	2	MidLumbarVentral	-242.430	228.832	109.754
	3	LLumbarVentral	-231.125	207.957	115.498
	4	SacrumMidline1	-193.548	248.292	139.232
	5	SacrumMidline2	-144.177	286.944	107.995
	6	ORIGIN 1	-153.163	259.996	102.688
Origin 5	1	RLumbarVentral	-252.217	243.795	124.826
	2	MidLumbarVentral	-242.470	228.834	109.706
	3	LLumbarVentral	-231.190	207.934	115.476
	4	SacrumMidline1	-193.600	248.280	139.213
	5	SacrumMidline2	-144.414	287.011	107.969
	6	ORIGIN 1	-149.414	260.373	93.081
Gluteus medius					
LOA Dorsal	1	RLumbarVentral	-251.999	242.252	124.524
	2	MidLumbarVentral	-242.044	227.723	109.184
	3	LLumbarVentral	-230.768	206.822	114.803
	4	SacrumMidline1	-193.289	247.333	138.474
	5	SacrumMidline2	-144.039	286.117	107.838
	6	LOA 1	-187.068	208.099	126.123
LOA Ventral	1	RLumbarVentral	-251.551	241.632	124.539
	2	MidLumbarVentral	-241.489	227.210	109.161
	3	LLumbarVentral	-230.118	206.326	114.817
	4	SacrumMidline1	-192.824	246.939	138.463
	5	SacrumMidline2	-143.927	286.161	107.711
	6	LOA 2	-140.247	210.522	55.684
Origin 1	1	RLumbarVentral	-252.151	242.612	124.652
	2	MidLumbarVentral	-242.339	227.977	109.384
	3	LLumbarVentral	-229.372	209.025	114.770
	4	SacrumMidline1	-193.426	247.434	138.541
	5	SacrumMidline2	-144.056	286.008	107.740
	6	Origin 1	-197.844	197.804	129.138
Origin 2	1	RLumbarVentral	-252.321	242.593	124.629
	2	MidLumbarVentral	-242.472	227.953	109.374
	3	LLumbarVentral	-231.217	207.035	115.041
	4	SacrumMidline1	-193.575	247.432	138.551
	5	SacrumMidline2	-144.192	286.011	107.741
	6	ORIGIN 2	-189.256	208.821	128.562
Origin 3	1	RLumbarVentral	-252.135	242.478	124.641
	2	MidLumbarVentral	-242.279	227.865	109.369
	3	LLumbarVentral	-230.995	206.962	115.010
	4	SacrumMidline1	-193.314	247.392	138.516
	5	SacrumMidline2	-144.062	285.965	107.739
	6	ORIGIN 3	-182.640	218.415	116.786

Table 7.1 Continued

MEASURE		REFERENCE	X	Y	Z
Origin 4	1	RLumbarVentral	-252.295	242.739	124.699
	2	MidLumbarVentral	-242.504	228.052	109.465
	3	LLumbarVentral	-231.263	207.152	115.089
	4	SacrumMidline1	-193.606	247.436	138.581
	5	SacrumMidline2	-144.140	285.910	107.671
	6	ORIGIN 4	-186.382	216.595	107.642
Origin 5	1	RLumbarVentral	-251.474	241.662	124.683
	2	MidLumbarVentral	-241.270	227.151	109.415
	3	LLumbarVentral	-230.106	205.885	115.343
	4	SacrumMidline1	-192.767	247.375	138.643
	5	SacrumMidline2	-144.047	286.619	107.735
	6	ORIGIN 5	-191.910	213.942	98.005
Origin 6	1	RLumbarVentral	-251.581	241.812	124.620
	2	MidLumbarVentral	-241.395	227.319	109.345
	3	LLumbarVentral	-229.957	206.470	115.180
	4	SacrumMidline1	-192.938	247.538	138.557
	5	SacrumMidline2	-144.143	286.678	107.713
	6	ORIGIN 6	-201.116	200.074	104.203
Origin 7	1	RLumbarVentral	-250.091	242.303	125.325
	2	MidLumbarVentral	-241.979	226.839	109.435
	3	LLumbarVentral	-230.038	206.199	115.175
	4	SacrumMidline1	-192.706	247.685	138.529
	5	SacrumMidline2	-143.966	286.804	107.641
	6	ORIGIN 7	-203.273	198.760	99.370
Origin 8	1	RLumbarVentral	-257.887	245.034	124.824
	2	MidLumbarVentral	-252.691	224.132	112.281
	3	LLumbarVentral	-239.048	208.415	115.305
	4	SacrumMidline1	-199.141	247.056	138.256
	5	SacrumMidline2	-147.544	282.042	107.432
	6	ORIGIN 8	-222.060	193.755	111.207
Origin 9	1	RLumbarVentral	-258.238	244.672	124.920
	2	MidLumbarVentral	-249.304	229.744	109.701
	3	LLumbarVentral	-238.939	208.428	115.350
	4	SacrumMidline1	-198.933	246.685	138.479
	5	SacrumMidline2	-147.469	282.071	107.420
	6	ORIGIN 9	-218.013	189.484	126.535
Insertion	1	RLumbarVentral	-257.780	245.674	125.097
	2	MidLumbarVentral	-249.229	230.357	109.970
	3	LLumbarVentral	-238.731	209.113	115.558
	4	SacrumMidline1	-198.789	247.610	138.580
	5	SacrumMidline2	-147.881	283.477	283.477
	6	INSERTION 1	-152.015	209.753	56.713

Table 7.1 Continued

MEASURE		REFERENCE	X	Y	Z
Piriformis					
LOA	1	RLumbarVentral	-263.683	330.682	121.545
	2	MidLumbarVentral	-264.993	311.151	110.785
	3	LLumbarVentral	-264.082	290.592	114.784
	4	SacrumMidline1	-211.083	303.910	137.720
	5	SacrumMidline2	-150.954	310.418	103.360
	6	LOA 1	-195.685	282.816	102.968
	7	LOA 2	-187.092	261.253	66.999
Origin - cranial	1	RLumbarVentral	-264.025	330.661	121.007
	2	MidLumbarVentral	-265.277	311.159	110.154
	3	LLumbarVentral	-265.194	290.005	114.456
	4	SacrumMidline1	-211.665	303.675	137.419
	5	SacrumMidline2	-151.305	310.060	103.407
	6	ORIGIN 1	-204.792	283.473	102.975
Origin - middle	1	RLumbarVentral	-264.003	330.760	121.033
	2	MidLumbarVentral	-265.271	311.216	110.177
	3	LLumbarVentral	-265.154	290.111	114.477
	4	SacrumMidline1	-211.473	303.933	137.355
	5	SacrumMidline2	-151.289	310.107	103.407
	6	ORIGIN 2	-197.702	286.031	105.993
Origin - caudal	1	RLumbarVentral	-264.065	330.477	121.020
	2	MidLumbarVentral	-265.255	311.066	110.139
	3	LLumbarVentral	-265.217	289.854	114.458
	4	SacrumMidline1	-211.657	303.596	137.389
	5	SacrumMidline2	-151.303	310.010	103.392
	6	ORIGIN 3	-193.676	285.347	104.666
Insertion	1	RLumbarVentral	-264.144	330.043	120.990
	2	MidLumbarVentral	-265.373	310.537	110.149
	3	LLumbarVentral	-265.102	289.547	114.246
	4	SacrumMidline1	-211.629	303.202	137.286
	5	SacrumMidline2	-151.290	309.735	103.327
	6	INSERTION 1	-182.036	250.540	55.418
Gluteus profundus					
Origin 1	1	RLumbarVentral	-263.886	332.111	120.839
	2	MidLumbarVentral	-265.294	312.692	110.006
	3	LLumbarVentral	-264.778	292.036	114.134
	4	SacrumMidline1	-211.792	304.706	137.373
	5	SacrumMidline2	-151.871	310.149	103.454
	6	ORIGIN 1	-253.618	268.503	101.313
Origin 2	1	RLumbarVentral	-263.946	332.417	120.853
	2	MidLumbarVentral	-265.417	312.830	110.114
	3	LLumbarVentral	-264.782	292.344	114.180
	4	SacrumMidline1	-211.867	304.904	137.383
	5	SacrumMidline2	-151.905	310.227	103.445
	6	ORIGIN 2	-235.381	271.129	106.545

Table 7.1 Continued

MEASURE		REFERENCE	X	Y	Z
Origin 3	1	RLumbarVentral	-263.677	332.309	120.823
	2	MidLumbarVentral	-265.247	312.634	109.975
	3	LLumbarVentral	-264.726	291.989	114.139
	4	SacrumMidline1	-211.827	304.733	137.244
	5	SacrumMidline2	-151.828	310.159	103.434
	6	ORIGIN 3	-221.680	274.132	106.891
Origin 4	1	RLumbarVentral	-263.656	332.202	120.780
	2	MidLumbarVentral	-265.201	312.460	109.953
	3	LLumbarVentral	-264.696	291.847	114.141
	4	SacrumMidline1	-211.792	304.595	137.221
	5	SacrumMidline2	-151.811	310.092	103.430
	6	ORIGIN 4	-207.207	276.177	87.544
Origin 5	1	RLumbarVentral	-264.034	331.833	120.873
	2	MidLumbarVentral	-265.325	312.452	109.995
	3	LlumbarVentral	-264.819	291.800	114.152
	4	SacrumMidline1	-211.898	304.528	137.402
	5	SacrumMidline2	-151.957	310.052	103.436
	6	ORIGIN 5	-221.563	273.830	76.102
Origin 6 & 7	1	RLumbarVentral	-261.850	335.513	121.367
	2	MidLumbarVentral	-263.194	315.322	111.997
	3	LLumbarVentral	-262.597	295.047	117.523
	4	SacrumMidline1	-209.559	309.532	139.510
	5	SacrumMidline2	-149.819	312.961	104.979
	6	ORIGIN 6	-240.583	271.287	90.196
	7	ORIGIN 7	-247.724	271.239	103.265
Insertion	1	RLumbarVentral	-262.544	334.119	120.740
	2	MidLumbarVentral	-263.693	314.060	111.129
	3	LLumbarVentral	-262.840	293.847	116.399
	4	SacrumMidline1	-210.125	308.223	138.867
	5	SacrumMidline2	-150.709	311.016	103.600
	6	INSERTION 1	-183.151	249.984	57.185
	7	INSERTION 2	-189.633	244.277	57.194
LOA	1	RLumbarVentral	-264.214	330.916	120.967
	2	MidLumbarVentral	-265.392	311.471	110.070
	3	LLumbarVentral	-264.622	290.937	114.077
	4	SacrumMidline1	-211.891	303.816	137.384
	5	SacrumMidline2	-151.444	310.113	103.458
	6	LOA 1	-235.191	270.767	95.923
	7	LOA 2	-208.209	256.178	61.791

Table 7.1 Continued

MEASURE		REFERENCE	X	Y	Z
Sacrocaudalis dorsalis medialis					
Origin Insertion LOA	1	RLumbarVentral	-263.261	333.040	120.299
	2	MidLumbarVentral	-264.254	313.030	110.519
	3	LLumbarVentral	-263.971	292.243	115.864
	4	SacrumMidline1	-210.685	307.528	138.435
	5	SacrumMidline2	-150.691	311.755	103.649
	6	ORIGIN 1	-221.503	300.747	141.669
	7	INSERTION 1	-176.068	299.564	116.097
Sacrocaudalis dorsalis lateralis					
Cranial Origin Insertion	1	RLumbarVentral	-263.589	331.724	119.691
	2	MidLumbarVentral	-264.860	311.427	109.877
	3	LLumbarVentral	-262.312	293.064	114.469
	4	SacrumMidline1	-210.647	306.485	138.277
	5	SacrumMidline2	-150.763	311.470	103.598
	6	ORIGIN 1	-193.498	297.657	119.508
	7	INSERTION 1	-235.117	276.896	141.383
LOA	1	RLumbarVentral	-263.279	332.925	120.198
	2	MidLumbarVentral	-264.332	312.867	110.472
	3	LLumbarVentral	-263.996	292.049	115.777
	4	SacrumMidline1	-210.323	307.513	138.715
	5	SacrumMidline2	-150.798	311.693	103.652
	6	LOA 1	-247.212	285.667	144.126
	7	LOA 2	-207.764	289.742	128.972
Multifidus lumborum					
Insertion - caudal	1	RLumbarVentral	-263.592	331.474	119.998
	2	MidLumbarVentral	-264.165	311.590	109.925
	3	LLumbarVentral	-263.068	291.509	114.969
	4	SacrumMidline1	-210.395	306.678	138.368
	5	SacrumMidline2	-150.840	311.939	103.585
	6	INSERTION 1	-218.754	299.149	125.798
Origin - cranial	1	RLumbarVentral	-261.853	332.654	119.751
	2	MidLumbarVentral	-263.948	311.219	110.224
	3	LLumbarVentral	-262.831	291.108	115.339
	4	SacrumMidline1	-209.643	305.813	138.854
	5	SacrumMidline2	-150.356	311.292	103.504
	6	ORIGIN 1	-233.162	300.354	150.077
	7	ORIGIN 2	-230.506	294.776	130.426
LOA	1	RLumbarVentral	-263.210	332.865	120.246
	2	MidLumbarVentral	-264.192	312.833	110.478
	3	LLumbarVentral	-263.901	291.991	115.829
	4	SacrumMidline1	-211.041	306.704	137.689
	5	SacrumMidline2	-150.750	311.701	103.634
	6	LOA 1	-249.268	292.147	148.194
	7	LOA 2	-212.808	296.392	131.247

Table 7.1 Continued

MEASURE		REFERENCE	X	Y	Z
Longissimus lumborum					
Origin 1	1	RLumbarVentral	-189.492	210.156	119.962
	2	MidLumbarVentral	-169.634	211.328	110.090
	3	LLumbarVentral	-149.237	211.664	114.977
	4	SacrumMidline1	-166.860	263.361	138.302
	5	SacrumMidline2	-174.147	323.024	103.637
	6	ORIGIN 1	-139.369	226.730	132.953
Origin 2	1	RLumbarVentral	-189.426	209.248	119.758
	2	MidLumbarVentral	-169.482	210.132	110.005
	3	LLumbarVentral	-149.192	211.599	114.965
	4	SacrumMidline1	-166.817	263.292	138.293
	5	SacrumMidline2	-175.931	322.367	103.600
	6	ORIGIN 2	-143.939	239.951	131.884
Origin 3	1	RLumbarVentral	-189.779	210.149	119.921
	2	MidLumbarVentral	-169.917	211.321	110.022
	3	LLumbarVentral	-149.516	211.638	114.985
	4	SacrumMidline1	-167.097	263.402	138.250
	5	SacrumMidline2	-174.229	323.000	103.629
	6	ORIGIN 3	-145.619	236.640	122.221
Iliocostalis lumborum					
Origin 1	1	RLumbarVentral	-186.790	174.448	120.455
	2	MidLumbarVentral	-171.642	161.405	110.356
	3	LLumbarVentral	-155.357	149.652	115.209
	4	SacrumMidline1	-134.048	200.157	138.412
	5	SacrumMidline2	-100.850	250.384	103.684
	6	ORIGIN 1	-137.975	148.533	133.998
Origin 2	1	RLumbarVentral	-187.149	173.847	120.426
	2	MidLumbarVentral	-171.354	161.109	110.109
	3	LLumbarVentral	-155.197	149.178	114.991
	4	SacrumMidline1	-133.878	199.831	138.258
	5	SacrumMidline2	-99.857	249.438	103.171
	6	ORIGIN 2	-136.893	152.226	132.018
Origin 3	1	RLumbarVentral	-187.197	174.085	120.496
	2	MidLumbarVentral	-171.570	161.342	110.232
	3	LLumbarVentral	-155.460	148.272	115.399
	4	SacrumMidline1	-134.206	200.160	138.278
	5	SacrumMidline2	-100.778	250.336	103.652
	6	ORIGIN 3	-138.784	147.491	109.220
Psoas major					
LOA	1	Ref1 (L)	-208.164	22.348	57.872
	2	MiddleRef	-186.136	27.771	62.412
	3	Ref2 (R)	-167.408	23.972	49.107
	4	ORIGIN 1	-158.335	51.657	65.621
	5	INSERTION 1	-143.252	102.315	68.315

Table 7.1 Continued

MEASURE		REFERENCE	X	Y	Z
Insertion	1	Ref1(L)	-344.215	105.727	58.609
	2	MiddleRef	-334.273	85.393	63.074
	3	Ref2 (R)	-334.875	65.965	50.141
	4	INSERTION 1	-212.810	54.917	59.511
Psoas minor					
Insertion	1	Ref1(L)	-344.000	104.111	58.347
	2	MiddleRef	-333.794	83.943	62.889
	3	Ref2 (R)	-334.092	64.436	50.103
	4	INSERTION 1	-260.322	73.822	67.513
	5	INSERTION 2	-250.599	81.173	73.323
LOA	1	Ref1 (L)	-344.034	103.948	58.286
	2	MiddleRef	-333.767	83.795	62.825
	3	Ref2 (R)	-333.929	64.344	49.957
	4	ORIGIN 1	-301.784	63.804	65.648
	5	INSERTION 1	-260.056	73.272	68.226
Iliacus					
Origin Insertion	1	Ref1 (L)	-344.217	105.650	57.918
	2	MiddleRef	-334.029	85.473	62.596
	3	Ref2 (R)	-334.075	66.084	49.918
	4	ORIGIN 1	-279.922	73.978	58.847
	5	INSERTION 1	-224.366	54.791	66.222

Table 7.2. Qualisys camera system reference points and prominent bony landmarks as captured from the surfaces of individual bone segments of the canine specimen. Coordinates were captured with respect to the local reference frame (in mm).

BONE		LANDMARK	X, Y, Z
L7	1	Right Mamillary Process – caudal tip	363.855, 220.18, -104.215
	2	L Mamillary Process – caudal tip	361.703, 220.38, -123.268
	3	Spinous Process – craniodorsal	347.709, 233.484, -112.268
	4	Right Caudal Articular Process - caudodorsal	334.891, 213.444, -98.427
	5	Left Caudal Articular Process - caudodorsal	334.994, 214.781, -123.321
Sacrum	1	Left Wing – caudodorsal tip	454.427, 213.559, -131.607
	2	Left Articular Surface – cranioventral tip	459.129, 187.592, -139.421
	3	Left Lateral Sacral Crest – caudodorsal tip	416.705, 194.851, -128.661
	4	Median Sacral Crest S3 – caudodorsal tip	420.789, 211.564, -108.59
	5	Right Wing – caudodorsal tip	454.146, 213.176, -93.248
	6	Right Articular Surface – cranioventral tip	461.74, 187.077, -86.563
	7	Right Lateral Sacral Crest – caudodorsal tip	419.224, 194.08, -94.38
Pelvis	1	R Cranial dorsal iliac spine	394.654, 83.155, -91.204
	2	R Caudal dorsal iliac spine	365.415, 63.582, -94.938
	3	R Ischiatic tuberosity	277.286, 43.582, -67.243
	4	L Cranial dorsal iliac spine	395.096, 82.679, -148.519
	5	L Caudal dorsal iliac spine	365.29, 63.543, -148.258
	6	L Ischiatic tuberosity	277.016, 45.694, -176.798

7.2 Appendix II

The following datasets provide a greater depth of information than presented in the Results chapter (chapter 4) regarding muscle and ligament data acquired from software analysis of the medical images taken of the intact specimen. This data may be of interest for progressing this GSD model, as well as future biomechanical studies of the canine spine. Muscle and ligament elements used in the AnyBody Modeling System were listed within their respective system groups in tables 6.1 and 6.3, respectively. Their names contain descriptions of origin and insertion nodes, defining muscle and ligament elements in the order of 'Abbreviation_Origin_Insertion'. Attachment node names were formatted to describe the bone segment to which the node was attached, the location of the node, and the position as left, right or central. All muscle (Table 6.2) and ligament (table 6.4) node coordinates were extracted from SolidWorks .stl files of the bone segments.

Abbreviations used in the tables of this section are defined as follows:

Bone Locations

A	arch
AL	arcuate line
AP	accessory process
B	body
Br	border
CAP	cranial articular process
IB	ilium body
I	ilium
ISC	intermediate sacral crest (S2/S3)
ITLA	ischiatic tuberosity lateral angle
ITS	ilium tuber sacrale
LSC	lateral sacral crest (S2/S3)
MIW	medial iliac wing
MP	mamillary process
SIJ	sacroiliac joint
SP	spinous process
SPS	sacropelvic surface
TP	transverse process
TR	trochanter representation
TS	tuber sacrale
W	wing

Positions

L	left
R	right
Ca	caudal
Cr	cranial
Do	dorsal
Ve	ventral
Mi	middle
Me	medial
Ro	root
La	lateral

Segments

L4-7	lumbar vertebrae 4-7
Sac	sacrum
S1-3	sacral vertebrae 1-3
Ca1	caudal vertebra
Pvs	pelvis

Table 7.3. Nodes of muscle element attachment sites of the canine spine model as displayed in the AnyBody Modeling System.

M#	LEFT MUSCLE ELEMENT	RIGHT MUSCLE ELEMENT
M1	**IliocostalisLumborum IL-L**	**IliocostalisLumborum IL-R**
1	IL_PvsMIWDoCrL_L7TPDoLaL	IL_PvsMIWDoCrR_L7TPDoLaR
2	IL_PvsMIWMiCrL_L7TPDoLaL	IL_PvsMIWMiCrR_L7TPDoLaR
3	IL_L7TPDoLaL_L6TPDoLaL	IL_L7TPDoLaR_L6TPDoLaR
4	IL_L6TPDoLaL_L5TPDoLaL	IL_L6TPDoLaR_L5TPDoLaR
5	IL_L5TPDoLaL_L4TPDoLaL	IL_L5TPDoLaR_L4TPDoLaR
M2	**LongissimusLumborum LL-L**	**LongissimusLumborum LL-R**
1	LL_L7SPL_L6CAPL	LL_L7SPR_L6CAPR
2	LL_L6SPL_L5CAPL	LL_L6SPR_L5CAPR
3	LL_PvsMIWDoCaL_L7CAPL	LL_PvsMIWDoCaR_L7CAPR
4	LL_PvsMIWDoCaL_L6CAPL	LL_PvsMIWDoCaR_L6CAPR
5	LL_PvsMIWDoCaL_L5CAPL	LL_PvsMIWDoCaR_L5CAPR
6	LL_PvsMIWMiCaL_L7ALaL	LL_PvsMIWMiCaR_L7ALaR
7	LL_PvsMIWMiCaL_L6APL	LL_PvsMIWMiCaR_L6APR
8	LL_PvsMIWMiCaL_L5APL	LL_PvsMIWMiCaR_L5APR
9	LL_PvsMIWMiCaL_L4APL	LL_PvsMIWMiCaR_L4APR
M3	**MultifidusLumborum ML-L**	**MultifidusLumborum ML-R**
1	ML_SacMPLCa1_L6SPL	ML_SacMPRCa1_L6SPL
2	ML_SacISCLS3_L6SPL	ML_SacISCRS3_L6SPL
3	ML_SacISCLS2_L5SPL	ML_SacISCRS2_L5SPL
4	ML_SacCAPLS1_L5SPL	ML_SacCAPRS1_L5SPL
5	ML_L7MPL_L4SPL	ML_L7MPL_L4SPL
M4	**Interspinales IS (CENTRAL MUSCLE ELEMENT)**	
1	IS_L7SPMiCr_L6SPMiCa	
2	IS_L6SPMiCr_L5SPMiCa	
3	IS_L5SPMiCr_L4SPMiCa	
M5	**IntertransversariiLumborum ITL-L**	**IntertransversariiLumborum ITL-R**
1	ITL_L7MPL_L5APL	ITL_L7MPR_L5APR
2	ITL_L6MPL_L4APL	ITL_L6MPR_L4APR
M6	**SacrocaudalisDorsalisLateralis SDL-L**	**SacrocaudalisDorsalisLateralis SDL-R**
1	SDL_L4MPL_L5MPL	SDL_L4MPR_L5MPR
2	SDL_L5MPL_L6MPL	SDL_L5MPR_L6MPR
3	SDL_L6MPL_SacCAPLS1	SDL_L6MPR_SacCAPRS1
M7	**SacrocaudalisDorsalisMedialis SDM-L**	**SacrocaudalisDorsalisMedialis SDM-R**
1	SDM_L7SPL_ SacMPLCa1	SDM_L7SPR_ SacMPRCa1
M8	**SacrocaudalisVentralisLateralis SVL-L**	**SacrocaudalisVentralisLateralis SVL-R**
1	SVL_L7BVeMeCrL_SacBVeLaLS1	SVL_L7BVeMeCrR_SacBVeLaRS1
M9	**PsoasMinor PMN (L)**	**PsoasMinor PMN-R**
1	PMR_L4BVeLaCrL_PvsALVeCrL	PMR_L4BVeLaCrR_PvsALVeCrR
2	PMR_L4BVeLaCrL_PvsALVeMiL	PMR_L4BVeLaCrR_PvsALVeMiR
3	PMR_L4BVeLaCrL_PvsALVeCaL	PMR_L4BVeLaCrR_PvsALVeCaR
4	PMR_L5BVeLaCrL_PvsALVeCrL	PMR_L5BVeLaCrR_PvsALVeCrR
5	PMR_L5BVeLaCrL_PvsALVeMiL	PMR_L5BVeLaCrR_PvsALVeMiR
6	PMR_L5BVeLaCrL_PvsALVeCaL	PMR_L5BVeLaCrR_PvsALVeCaR

Table 7.3 Continued

M#	LEFT MUSCLE ELEMENT	RIGHT MUSCLE ELEMENT
M10	**PsoasMajor PMJ-L**	**PsoasMajor PMJ-R**
1	PMJ_L4BVeLaCrL_PvsIBVeCrL	PMJ_L4BVeLaCrR_PvsIBVeCrR
2	PMJ_L4BVeLaCrL_PvsIBVeMiL	PMJ_L4BVeLaCrR_PvsIBVeMiR
3	PMJ_L4BVeLaCrL_PvsIBVeCaL	PMJ_L4BVeLaCrR_PvsIBVeCaR
4	PMJ_L5BVeLaCrL_PvsIBVeCrL	PMJ_L5BVeLaCrR_PvsIBVeCrR
5	PMJ_L5BVeLaCrL_PvsIBVeMiL	PMJ_L5BVeLaCrR_PvsIBVeMiR
6	PMJ_L5BVeLaCrL_PvsIBVeCaL	PMJ_L5BVeLaCrR_PvsIBVeCaR
7	PMJ_L6BVeLaCrL_PvsIBVeCrL	PMJ_L6BVeLaCrR_PvsIBVeCrR
8	PMJ_L6BVeLaCrL_PvsIBVeMiL	PMJ_L6BVeLaCrR_PvsIBVeMiR
9	PMJ_L6BVeLaCrL_PvsIBVeCaL	PMJ_L6BVeLaCrR_PvsIBVeCaR
10	PMJ_L7BVeLaCrL_PvsIBVeCrL	PMJ_L7BVeLaCrR_PvsIBVeCrR
11	PMJ_L7BVeLaCrL_PvsIBVeMiL	PMJ_L7BVeLaCrR_PvsIBVeMiR
12	PMJ_L7BVeLaCrL_PvsIBVeCaL	PMJ_L7BVeLaCrR_PvsIBVeCaR
13	PMJ_L4BLaCaL_PvsIBVeCrL	PMJ_L4BLaCaR_PvsIBVeCrR
14	PMJ_L4BLaCaL_PvsIBVeMiL	PMJ_L4BLaCaR_PvsIBVeMiR
15	PMJ_L4BLaCaL_PvsIBVeCaL	PMJ_L4BLaCaR_PvsIBVeCaR
16	PMJ_L5BLaCaL_PvsIBVeCrL	PMJ_L5BLaCaR_PvsIBVeCrR
17	PMJ_L5BLaCaL_PvsIBVeMiL	PMJ_L5BLaCaR_PvsIBVeMiR
18	PMJ_L5BLaCaL_PvsIBVeCaL	PMJ_L5BLaCaR_PvsIBVeCaR
19	PMJ_L6BLaCaL_PvsIBVeCrL	PMJ_L6BLaCaR_PvsIBVeCrR
20	PMJ_L6BLaCaL_PvsIBVeMiL	PMJ_L6BLaCaR_PvsIBVeMiR
21	PMJ_L6BLaCaL_PvsIBVeCaL	PMJ_L6BLaCaR_PvsIBVeCaR
22	PMJ_L7BLaCaL_PvsIBVeCrL	PMJ_L7BLaCaR_PvsIBVeCrR
23	PMJ_L7BLaCaL_PvsIBVeMiL	PMJ_L7BLaCaR_PvsIBVeMiR
24	PMJ_L7BLaCaL_PvsIBVeCaL	PMJ_L7BLaCaR_PvsIBVeCaR
M11	**QuadratusLumborum QL-L**	**QuadratusLumborum QL-R**
1	QL_L4TPVeLaL_L5TPVeLaL	QL_L4TPVeLaR_L5TPVeLaR
2	QL_L5TPVeLaL_L6TPVeLaL	QL_L5TPVeLaR_L6TPVeLaR
3	QL_L6TPVeLaL_L7TPVeLaL	QL_L6TPVeLaR_L7TPVeLaR
4	QL_L7TPVeLaL_PvsMIWVeCrL	QL_L7TPVeLaR_PvsMIWVeCrR
5	QL_L4TPVeMiL_L5TPVeMiL	QL_L4TPVeMiR_L5TPVeMiR
6	QL_L5TPVeMiL_L6TPVeMiL	QL_L5TPVeMiR_L6TPVeMiR
7	QL_L6TPVeMiL_L7TPVeMiL	QL_L6TPVeMiR_L7TPVeMiR
8	QL_L7TPVeMiL_PvsMIWVeCaL	QL_L7TPVeMiR_PvsMIWVeCaR
M12	**GluteusSuperficialis GS-L**	**GluteusSuperficialis GS-R**
1	GS_SacLSCLS2_PvsTRL	GS_SacLSCRS2_PvsTRR
2	GS_SacLSCLS3_PvsTRL	GS_SacLSCRS3_PvsTRR
3	GS_SacTPLaLCa1_PvsTRL	GS_SacTPLaRCa1_PvsTRR
M13	**Piriformis PF-L**	**Piriformis PF-R**
1	PF_SacTPLaLCa1_PvsTRL	PF_SacTPLaRCa1_PvsTRR
2	PF_SacLSCLS3_PvsTRL	PF_SacLSCRS3_PvsTRR

Table 7.4. Node coordinates of muscle element attachment sites of the canine spine model as acquired in SolidWorks with respect to the local reference frame (in mm).

NODE	COORDINATES	NODE	COORDINATES
L4 Segment			
APL	12.38950, -12.10263, -18.59534	SPL	32.34119, -0.04636, 9.56192
APR	10.45147, 13.01684, -18.54284	SPR	32.25913, 4.15804, 9.63415
BLaCaL	-2.17247, -14.15004, -9.65324	SPMiCa	27.57938, 2.02118, -3.44910
BLaCaR	-4.01187, 12.56463, -10.52026	TPDoLaL	-12.39845, -32.84280, 16.06662
BVeLaCrL	-13.02273, -10.60563, 5.32245	TPDoLaR	-18.65838, 31.84415, 12.75854
BVeLaCrR	-13.78043, 10.00163, 5.49438	TPVeMiL	-12.74929, -22.78089, 9.98996
CAPL	17.79881, -11.51895, 14.62409	TPVeMiR	-16.57174, 20.79064, 7.53917
CAPR	15.93669, 13.58858, 13.33643	TPVeLaL	-17.28795, -29.57060, 19.08336
MPL	16.79924, -15.73165, 18.02234	TPVeLaR	-22.48677, 28.56153, 16.23413
MPR	14.93330, 17.55032, 17.13679		
L5 Segment			
APL	-12.13646, 8.07861, -15.50832	SPMiCa	-27.58355, 1.30342, 2.06753
APR	-11.13039, -15.61996, -8.32803	SPMiCr	-18.41962, 4.83599, 14.87216
BLaCaL	-0.79698, 11.05435, -13.29173	SPL	-29.76131, 8.30910, 13.30239
BLaCaR	-0.58785, -16.51138, -5.49624	SPR	-29.89311, 4.45470, 14.67049
BVeLaCrL	15.39439, 10.89896, -0.70979	TPDoLaL	19.31601, 38.59025, 3.27804
BVeLaCrR	15.89969, -9.26353, 5.42855	TPDoLaR	22.28767, -28.65111, 23.63171
CAPL	-14.19846, 12.90737, 12.54529	TPVeLaL	25.13626, 34.57069, 6.20765
CAPR	-13.61741, -4.79518, 19.13588	TPVeLaR	26.57759, -24.85011, 25.53858
MPL	-12.28737, 17.55166, 17.91013	TPVeMiL	16.46018, 24.94763, -1.09432
MPR	-11.90327, -7.26306, 25.04830	TPVeMiR	18.21412, -21.21039, 13.68781
L6 Segment			
APL	12.58607, 11.15128, -8.22726	SPMiCa	-8.14239, 24.82551, 0.64153
APR	-13.22525, 6.66146, -13.44333	SPMiCr	-7.00186, 19.55923, 13.06494
BLaCaL	14.85130, 6.02078, -4.81783	SPL	-11.70382, 28.20886, 13.20359
BLaCaR	-12.64425, 1.13105, -10.25878	SPR	-14.99233, 25.40578, 12.29034
BVeLaCrL	13.24934, -12.40629, 4.40535	TPDoLaL	39.67230, -14.75161, 23.31470
BVeLaCrR	-6.70563, -17.07323, 0.89909	TPDoLaR	-30.75209, -34.93276, 11.55171
CAPL	3.71582, 14.64850, 15.34239	TPVeMiL	28.95933, -10.09679, 12.64235
CAPR	-14.09587, 12.19251, 12.49932	TPVeMiR	-23.19807, -26.24996, 4.02675
MPL	4.86474, 12.28017, 23.86489	TPVeLaL	38.65089, -17.07530, 26.22870
MPR	-17.44945, 8.09255, 18.87931	TPVeLaR	-30.32333, -37.10506, 13.58587

Table 7.4 Continued

NODE	COORDINATES	NODE	COORDINATES
L7 Segment			
ALaL	10.31287, 9.38904, -4.57347	MPL	14.86340, -4.74953, 21.99925
ALaR	-12.03667, 7.78116, -2.31328	MPR	-7.77860, -3.11017, 23.84934
BLaCaL	13.80735, 2.43097, -7.48981	SPL	5.82885, 20.49498, 20.09535
BLaCaR	-14.78643, 0.46806, -3.33399	SPR	1.18773, 20.62289, 22.52598
BVeLaCrL	10.37995, -11.62014, -7.64680	SPMiCr	2.32767, 10.27708, 18.03669
BVeLaCrR	-11.43782, -11.94254, -3.65088	TPDoLaL	38.30346, -30.07041, 0.78586
BVeMeCaL	2.11687, -1.84371, -16.34659	TPDoLaR	-34.09216, -34.99181, 9.23372
BVeMeCaR	-6.98982, -2.38084, -15.32834	TPVeMiL	26.88478, -14.11996, -2.62109
BVeMeCrL	3.29303, -11.17153, -9.71746	TPVeMiR	-24.09406, -17.26867, 4.29821
BVeMeCrR	-6.11182, -11.32008, -8.39689	TPVeLaL	37.87733, -30.78986, -1.67992
CAPL	9.02964, 2.06455, 18.63704	TPVeLaR	-34.49498, -35.69797, 7.42289
CAPR	-2.63471, 2.86890, 19.27125		
Sacrum Segment			
BVeLaLS1	7.40891, 11.42764, -10.60787	SPLS1	-4.91103, 0.76931, 19.85300
BVeLaRS1	9.03382, -10.22295, -10.49504	SPRS1	-4.50229, -1.61242, 19.88690
BVeLaLS2	-5.20822, 8.80939, -3.85881	SPLS2	-13.96420, -0.68785, 17.95380
BVeLaRS2	-4.04130, -9.55811, -2.79587	SPRS2	-13.32514, -3.36345, 16.69606
BVeMeLS3	-19.30802, 1.77828, -8.51628	SPLS3	-22.86784, -1.98721, 14.03350
BVeMeRS3	-19.01987, -1.43132, -8.61834	SPRS3	-21.78498, -5.13609, 12.74737
BVeMeLCa1	-29.16217, 0.53708, -11.80865	TPLaLCa1	-37.34065, 14.00354, -7.82364
BVeMeRCa1	-28.89851, -2.49141, -11.52959	TPLaRCa1	-33.932, -18.63670, -8.13882
CAPLS1	17.11311, 16.26359, 14.97232	TPVeRoLCa1	-29.70850, 9.24956, -7.57696
CAPRS1	19.30395, -13.77798, 15.90502	TPVeRoRCa1	-27.48088, -11.97784, -8.12932
ISCLS2	-0.29288, 8.91874, 13.95271	LSCLS2	-12.36955, 19.95009, 3.13993
ISCRS2	0.35460, -9.09266, 13.13965	LSCRS2	-9.82537, -20.87919, 1.84412
ISCLS3	-9.70583, 5.59302, 10.28060	LSCLS3	-24.65225, 16.49000, -2.64149
ISCRS3	-9.56608, -6.47468, 9.93286	LSCRS3	-23.93815, -19.63986, -3.65289
MPLCa1	-20.97729, 6.70397, 7.66911	LSCVeRoLS3	-19.96542, 12.43139, -3.13445
MPRCa1	-19.28087, -9.09813, 7.38618	LSCVeRoRS3	-16.07409, -12.80258, -2.76154

Table 7.4 Continued

NODE	COORDINATES	NODE	COORDINATES
Pelvis Segment			
ALVeCaL	-12.89763, -26.19898, 27.19657	ITSCrR	44.59010, 24.34088, -19.22730
ALVeCaR	-12.74079, 23.91331, 29.27530	MIWDoCaL	64.08078, -27.16375, -18.43693
ALVeMiL	-7.59142, -29.92427, 24.23187	MIWDoCaR	67.38190, 23.77566, -12.08918
ALVeMiR	-6.52212, 28.11368, 25.28839	MIWDoCrL	76.57911, -32.32414, -10.05929
ALVeCrL	-0.76301, -31.71623, 20.16205	MIWDoCrR	78.23669, 31.57325, -6.09755
ALVeCrR	1.52139, 30.10572, 19.92642	MIWMiCaL	58.01887, -26.58516, -2.10083
IBVeCaL	13.22256, -39.09643, 13.68405	MIWMiCaR	58.75442, 26.09580, 1.39237
IBVeCaR	15.83761, 38.11545, 13.40609	MIWMiCrL	67.55093, -34.76894, 5.63914
IBVeMiL	25.01762, -39.47466, 13.44377	MIWMiCrR	68.08649, 33.69635, 5.67586
IBVeMiR	28.64314, 37.91173, 12.92056	MIWVeCaL	51.04921, -29.23819, 9.09723
IBVeCrL	46.24915, -41.94560, 18.09120	MIWVeCaR	49.23840, 26.45433, 7.54942
IBVeCrR	49.32069, 40.68187, 16.90352	MIWVeCrL	56.47752, -38.71679, 19.38275
ITSCaL	35.18692, -26.00963, -15.89164	MIWVeCrR	57.35951, 37.56669, 18.23756
ITSCaR	35.61058, 25.02206, -16.78994	TRL	-12.77346, -44.36588, -0.31974
ITSCrL	47.13694, -27.21059, -19.48751	TRR	-8.95180, 44.03708, 1.45373

Table 7.5. Nodes of ligament attachment sites of the canine spine model as displayed in the AnyBody Modeling System.

#	LEFT LIGAMENT	RIGHT LIGAMENT
L1	**Supraspinous LSS (Central)**	
1	LSS_L4LSPDo_L5LSPDo	
2	LSS_L5LSPDo_L6LSPDo	
3	LSS_L6LSPDo_L7LSPDo	
4	LSS_L7LSPDo_SacLSPDo	
L2	**Ventral Longitudinal LVL (Central)**	
1	LVL_L4LBVeCa_L5LBVeCr	
2	LVL_L5LBVeCa_L6LVeCr	
3	LVL_L6LBVeCa_L7LBVeCr	
4	LVL_L7LBVeCa_SacLBVeCr	
L3	**Dorsal Longitudinal LDL (Central)**	
1	LDL_L4LBDoCa_L5LBDoCr	
2	LDL_L5LVDoCa_L6LVDoCr	
3	LDL_L6LVDoCa_L7LVDoCr	
4	LDL_L7LVDoCa_SacLVDoCr	

Table 7.5 Continued

#	LEFT LIGAMENT	RIGHT LIGAMENT
L4	**L4 Interspinous LIS (Central)**	
1	LIS_L4LSPMiCa_L5LSPMiCr	
2	LIS_L5LSPMiCa_L6LSPMiCr	
3	LIS_L6LSPMiCa_L7LSPMiCr	
4	LIS_L7LSPMiCa_SacLSPMiCrS1	
L5	**Intertransverse LIT-L**	**Intertransverse LIT-R**
1	LIT_L4LTPMeCaL_L5LTPMeCrL	LIT_L4LTPMeCaR_L5LTPMeCrR
2	LIT_L5LTPMeCaL_L6LTPMeCrL	LIT_L5LTPMeCaR_L6LTPMeCrR
3	LIT_L6LTPMeCaL_L7LTPMeCrL	LIT_L6LTPMeCaR_L7LTPMeCrR
4	LIT_L4LTPMiCaL_L5LTPMiCrL	LIT_L4LTPMiCaR_L5LTPMiCrR
5	LIT_L5LTPMiCaL_L6LTPMiCrL	LIT_L5LTPMiCaR_L6LTPMiCrR
6	LIT_L6LTPMiCaL_L7LTPMiCrL	LIT_L6LTPMiCaR_L7LTPMiCrR
7	LIT_L4LTPLaCaL_L5LTPLaCrL	LIT_L4LTPLaCaR_L5LTPLaCrR
8	LIT_L5LTPLaCaL_L6LTPLaCrL	LIT_L5LTPLaCaR_L6LTPLaCrR
9	LIT_L6LTPLaCaL_L7LTPLaCrL	LIT_L6LTPLaCaR_L7LTPLaCrR
L6	**Yellow LY-L**	**Yellow LY-R**
1	LY_L4LACaL_L5LACrL	LY_L4LACaR_L5LACrR
2	LY_L5LACaL_L6LACrL	LY_L5LACaR_L6LACrR
3	LY_L6LACaL_L7LACrL	LY_L6LACaR_L7LACrR
4	LY_L7LACaL_SacLACrL	LY_L7LACaR_SacLACrR
L7	**Ventral Sacroiliac LVSI-L**	**Ventral Sacroiliac LVSI-R**
	LVSI_PvsLSPSCrL_SacLWVeCrL	LVSI_PvsRSPSCrR_SacRWVeCrR
	LVSI_PvsLSPSCaL_SacLWVeCrMiL	LVSI_PvsLSPSCaR_SacLWVeCrMiR
	LVSI_PvsLIBVeCrL_SacLWVeCaMiL	LVSI_PvsLIBVeCrR_SacLWVeCaMiR
	LVSI_PvsLIBVeCaL_SacLWVeCaL	LVSI_PvsLIBVeCaR_SacLWVeCaR
L8	**Dorsal Sacroiliac LDSI-L**	**Dorsal Sacroiliac LDSI-R**
	LDSI_PvsLTSCrMeL_SacLWCaL	LDSI_PvsLTSCrMeR_SacLWCaR
	LDSI_PvsLTSCaLaL_SacLLSCLS2	LDSI_PvsLTSCaLaR_SacLLSCRS2
L9	**Sacrotuberous LST-L**	**Sacrotuberous LST-R**
	LST_SacLLSCLS3_PvsLITLAL	LST_SacLLSCRS3_PvsLITLAR
	LST_SacLTPLaLCa1_PvsLITLAL	LST_SacLTPLaRCa1_PvsLITLAR
L10	**Sacroiliac Joint Capsule LSIJ-L**	**Sacroiliac Joint Capsule LSIJ-R**
	LSIJ_PvsLIMeCrL_SacLWDoCrL	LSIJ_PvsLIMeCrR_SacLWDoCrR
	LSIJ_PvsLIMeMiL_SacLWDoMiL	LSIJ_PvsLIMeMiR_SacLWDoMiR
	LSIJ_PvsLIMeCaL_SacLWDoCaL	LSIJ_PvsLIMeCaR_SacLWDoCaR

Table 7.6. Node coordinates of ligament attachment sites of the canine spine model as acquired in SolidWorks with respect to the local reference frame (in mm).

NODE	COORDINATES	NODE	COORDINATES
L4 Segment			
LACaL	10.21956, -5.96926, -12.98804	LTPMeCaL	-3.41737, -14.68778, -8.83152
LACaR	8.66233, 6.95353, -12.67846	LTPMeCaR	-5.78321, 13.34147, -9.87272
LBDoCa	-0.25498, -0.17023, -14.38662	LTPMiCaL	-9.18635, -22.76485, 1.93347
LBVeCa	-14.47867, -0.28930, -18.04745	LTPMiCaR	-13.73005, 22.13469, 1.8457
LSPDo	34.90437, 1.85033, 12.03934	LTPLaCaL	-12.69297, -34.78024, 14.01899
LSPMiCa	27.48445, 2.01833, -3.60006	LTPLaCaR	-19.19742, 33.38914, 10.72690
L5 Segment			
LACaL	-10.63652, 3.73075, -11.68316	LTPMeCaR	0.85342, -16.46410, -4.77900
LACaR	-10.17215, -9.27438, -7.28619	LTPMeCrL	9.47015, 14.54316, 2.37138
LACrL	-0.53548, 6.77482, 12.47829	LTPMeCrR	10.54839, -11.37248, 10.58608
LACrR	0.85260, 0.40249, 16.48517	LTPMiCaL	9.50913, 21.29500, -7.93033
LBDoCa	-3.21030, -4.01754, -13.72527	LTPMiCaR	11.41622, -22.40537, 6.49561
LBDoCr	8.29540, 2.64655, 9.26263	LTPMiCrL	15.81815, 23.77296, 3.75439
LBVeCa	9.80343, -6.72030, -21.03614	LTPMiCrR	18.12403, -16.90416, 17.25732
LBVeCr	21.55310, -0.12934, 2.58350	LTPLaCaL	19.65071, 38.39470, 1.98244
LSPDo	-32.64081, 7.78794, 15.47571	LTPLaCaR	22.78929, -29.75011, 21.90976
LSPMiCa	-27.48856, 1.25526, 1.96139	LTPLaCrL	28.28789, 33.34146, 12.86771
LSPMiCr	-18.31552, 4.80945, 14.85093	LTPLaCrR	29.34431, -19.30742, 29.89708
LTPMeCaL	0.73472, 11.52406, -12.69921		
L6 Segment			
LACaL	7.03015, 11.36494, -7.68433	LTPMeCaR	-13.57283, -4.54335, -8.50573
LACaR	-7.89445, 7.71255, -11.30496	LTPMeCrL	14.11562, -3.79487, 8.99630
LACrL	1.24619, 1.01992, 13.91526	LTPMeCrR	-12.64608, -11.66821, 3.73703
LACrR	-6.49799, -0.13463, 12.35607	LTPMiCaL	26.61878, -3.18463, 5.04783
LBDoCa	2.05394, 3.46598, -13.00021	LTPMiCaR	-21.89436, -18.46292, -2.80027
LBDoCr	0.32830, -7.06256, 9.99286	LTPMiCrL	25.37065, -9.96400, 16.55266
LBVeCa	6.62978, -8.13172, -20.14642	LTPMiCrR	-20.33837, -22.25624, 8.66304
LBVeCr	4.68356, -19.64875, 2.33095	LTPLaCaL	39.87690, -14.85378, 21.70135
LSPDo	-14.88531, 29.02526, 12.93039	LTPLaCaR	-30.43762, -35.36917, 9.29713
LSPMiCa	-8.13668, 24.73688, 0.50863	LTPLaCrL	36.08593, -18.93015, 29.52923
LSPMiCr	-6.98871, 19.36563, 13.07033	LTPLaCrR	-28.16940, -37.08074, 18.51305
LTPMeCaL	16.48565, 4.03802, -2.74032		

Table 7.6 Continued

NODE	COORDINATES	NODE	COORDINATES
L7 Segment			
LACaL	3.66102, 17.30279, -1.69159	LSPMiCa	1.84215, 19.12312, 12.20760
LACaR	-4.07524, 17.79827, -1.20363	LSPMiCr	2.06486, 10.26915, 18.10065
LACrL	6.00379, -5.35243, 11.75318	LTPMeCrL	16.67156, -6.43963, -0.72528
LACrR	-1.88442, -6.41032, 13.11642	LTPMeCrR	-14.24622, -8.32802, 3.59154
LBDoCa	-0.53000, 9.31060, -5.36728	LTPMiCrL	27.61218, -18.30079, 0.84245
LBDoCr	1.12023, -8.78550, 4.11531	LTPMiCrR	-23.88742, -20.34783, 7.02442
LBVeCa	-2.56311, 0.42481, -19.97465	LTPLaCrL	37.16388, -35.76134, 1.83466
LBVeCr	0.11865, -17.00250, -8.11259	LTPLaCrR	-31.82730, -40.03915, 11.16198
LSPDo	3.43636, 23.03751, 23.96220		
Sacrum Segment			
LSPDoS1	-4.02964, -0.76133, 21.76012	LWDoCaL	9.54000, 10.82523, -19.07663
LSPMiCrS1	0.95999, 0.18266, 16.17165	LWDoCaR	8.21547, 10.997790, 14.69180
LACrL	12.71994, 4.99565, 8.94201	LWCaL	-0.53299, 7.56827, -20.66190
LACrR	13.67618, -3.81611, 8.92259	LWCaR	-2.21332, 7.80108, 18.91691
LBDoCr	14.79684, 0.70427, 2.70799	LLSCS2L	-7.65995, 8.4578., -18.17528
LBVeCr	16.77465, 0.69275, -11.90639	LLSCS2R	-9.17782, 8.47905, 14.97100
LLSCLS3	-28.17251, 16.39731, -4.04654	LWVeCrL	20.23674, -7.70360, -21.74770
LLSCRS3	-25.96946, -19.38039, -5.75999	LWVeCrR	18.53240, -6.70464, 19.14452
LTPLaLCa1	-37.71376, 13.32889, -7.99228	LWVeCrMiL	14.85860, -19.19719, -25.71927
LTPLaRCa1	-34.81520, -17.43958, -8.42651	LWVeCrMiR	13.60843, -16.55889, 23.00748
LWDoCrL	21.22419, 3.11069, -22.41289	LWVeCaMiL	5.35589, -20.54870, -24.30047
LWDoCrR	19.33327, 6.70657, 20.74309	LWVeCaMiR	8.97098, -19.28596, 25.55024
LWDoMiL	17.55435, 9.80449, -20.83059	LWVeCaL	0.57594, -18.65169, -23.38479
LWDoMiR	15.21651, 11.39234, 18.03364	LWVeCaR	0.68997, -20.56087, 21.82651
Pelvis Segment			
LITLAL	-52.81643, -50.37990, -21.49843	LIBVeCrL	3.61202, -21.65138, -26.99556
LITLAR	-50.48292, 50.42136, -20.36265	LIBVeCrR	7.59114, -20.84852, 27.11053
LTSCrMeL	2.47042, 10.78904, -27.35371	LIBVeCaL	-1.01008, -19.10530, -24.94336
LTSCrMeR	2.73564, 10.65319, 22.82605	LIBVeCaR	-0.65576, -20.90668, 23.49412
LTSCaLaL	2.54098, 10.31691, -30.76796	LIMeCrL	22.10196, 3.75561, -25.53479
LTSCaLaR	1.41742, 9.45976, 26.94194	LIMeCrR	19.33327, 6.70657, 20.74309
LSPSCrL	22.78597, -3.34196, -27.46711	LIMeMiL	18.296, 11.05298, -23.82128
LSPSCrR	20.89730, -3.55287, 25.273444	LIMeMiR	15.21651, 11.39234, 18.03364
LSPSCaL	17.95099, -15.65202, -30.24250	LIMeCaL	6.50254, 12.20715, -23.07655
LSPSCaR	18.88628, -13.05152, 27.79446	LIMeCaR	8.21547, 10.97790, 14.69180

8. REFERENCES

Aleotti, J., Caselli, S., Bracchi, P. G., & Gosi, S. (2008). *Physically-Based Simulation of the Spine in Dog Walking*.

Arshad, R., Zander, T., Dreischarf, M., & Schmidt, H. (2016). Influence of lumbar spine rhythms and intra-abdominal pressure on spinal loads and trunk muscle forces during upper body inclination. *Medical Engineering & Physics, 38*(4), 333-338.

Benninger, M. I., Seiler, G. S., Robinson, L. E., Ferguson, S. J., Bonel, H. M., Busato, A. R., & Lang, J. (2004). Three-dimensional motion pattern of the caudal lumbar and lumbosacral portions of the vertebral column of dogs. *American Journal of Veterinary Research, 65*(5), 544-551.

Benninger, M. I., Seiler, G. S., Robinson, L. E., Ferguson, S. J., Bonel, H. M., Busato, A. R., & Lang, J. (2006). Effects of anatomic conformation on three-dimensional motion of the caudal lumbar and lumbosacral portions of the vertebral column of dogs. *American Journal of Veterinary Research, 67*(1), 43-50.

Bergknut, N., Egenvall, A., Hagman, R., Gustas, P., Hazewinkel, H. A. W., Meij, B. P., & Lagerstedt, A. (2012). Incidence of intervertebral disk degeneration-related diseases and associated mortality rates in dogs. *Journal of the American Veterinary Medical Association, 240*(11), 1300-1309.

Brown, N. A. T., Kawcak, C. E., McIlwraith, C. W., & Pandy, M. G. (2003). Architectural properties of distal forelimb muscles in horses, Equus caballus. *Journal of Morphology, 258*(1), 106-114.

Carbone, V., Fluit, R., Pellikaan, P., van der Krogt, M. M., Janssen, D., Damsgaard, M., & Verdonschot, N. (2015). TLEM 2.0-A comprehensive musculoskeletal geometry dataset for subject-specific modeling of lower extremity. *Journal of Biomechanics, 48*(5), 734-741.

Chazal, J., Tanguy, A., Bourges, M., Gaurel, G., Escande, G., Guillot, M., & Vanneuville, G. (1985). Biomechanical properties of spinal ligaments and a histological study of the supraspinal ligament in traction. *Journal of Biomechanics, 18*(3), 167-176.

Christophy, M., Senan, N. A. F., Lotz, J. C., & O'Reilly, O. M. (2012). A Musculoskeletal model for the lumbar spine. *Biomechanics and Modeling in Mechanobiology, 11*(1-2), 19-34.

Damsgaard, M., Rasmussen, J., Christensen, S. T., Surma, E., & de Zee, M. (2006). Analysis of musculoskeletal systems in the anybody modeling system. *Simulation Modelling Practice and Theory, 14*(8), 1100-1111.

De Zee, M., Hansen, L., Wong, C., Rasmussen, J., & Simonsen, E. B. (2007). A generic detailed rigid-body lumbar spine model. *Journal of Biomechanics, 40*(6), 1219-1227.

Dries, B., Jonkers, I., Dingemanse, W., Vanwanseele, B., Vander Sloten, J., van Bree, H., & Gielen, I. (2016). Musculoskeletal modelling in dogs: challenges and future perspectives. *Veterinary and Comparative Orthopaedics and Traumatology, 29*(3), 181-187.

Early, P., Mente, P., Dillard, S., & Roe, S. (2015). In vitro biomechanical evaluation of internal fixation techniques on the canine lumbosacral junction. *Peerj, 3*.

Evans, R. I., Herbold, J. R., Bradshaw, B. S., & Moore, G. E. (2007). Causes for discharge of military working dogs from service: 268 cases (2000-2004). *Journal of the American Veterinary Medical Association, 231*(8), 1215-1220.

Evans, H. E., & de Lahunta, A. (2013). *Miller's Anatomy of the Dog* (4th ed.). St. Louis, Missouri: Elsevier Saunders.

Fraser, D. (2003). Assessing animal welfare at the farm and group level: The interplay of science and values. *Animal Welfare, 12*(4), 433-443.

Hediger, K. U., Ferguson, S. J., Gedet, P., Busato, A., Forterre, F., Isler, S., & Lang, J. (2009). Biomechanical analysis of torsion and shear forces in lumbar and lumbosacral spine segments of nonchondrodystrophic dogs. *Veterinary Surgery, 38*(7), 874-880.

Herzog, W., Kamal, S., & Clarke, H. D. (1992). Myofilament lengths of cat skeletal-muscle - theoretical considerations and functional implications. *Journal of Biomechanics, 25*(8), 945-948.

Horsman, M. D. K., Koopman, H. F. J. M., van der Helm, F. C. T., Prose, L. P., & Veeger, H. E. J. (2007). Morphological muscle and joint parameters for musculoskeletal modelling of the lower extremity. *Clinical Biomechanics, 22*(2), 239-247.

Ignasiak, D., Dendorfer, S., & Ferguson, S. J. (2015). Thoracolumbar spine model with articulated ribcage for the prediction of dynamic spinal loading. *Journal of Biomechanics*.

Infantolino, B. W., Ellis, M. J., & Challis, J. H. (2010). Individual sarcomere lengths in whole muscle fibers and optimal fiber length computation. *Anatomical Record-Advances in Integrative Anatomy and Evolutionary Biology, 293*(11), 1913-1919.

King, T., Reiss, M., & Roberts, M. (2001). *Practical Advanced Biology*. Cheltenham, United Kingdom: Thomas Nelson and Sons Ltd.

Klein Breteler, M. D., Spoor, C. W., & Van der Helm, F. C. T. (1999). Measuring muscle and joint geometry parameters of a shoulder for modeling purposes. *Journal of Biomechanics, 32*(11), 1191-1197.

Koblauch, H. (2015). *Low back load in airport baggage handlers.* University of Copenhagen, Copenhagen, Denmark.

Kura, H., Luo, Z. P., Kitaoka, H. B., & An, K. N. (1997). Quantitative analysis of the intrinsic muscles of the foot. *Anatomical Record, 249*(1), 143-151.

Lim, T. H., Goel, V. K., Weinstein, J. N., & Kong, W. Z. (1994). Stress-analysis of a canine spinal motion segment using the finite-element technique. *Journal of Biomechanics, 27*(10), 1259-&.

Linn, L. L., Bartels, K. E., Rochat, M. C., Payton, M. E., & Moore, G. E. (2003). Lumbosacral stenosis in 29 military working dogs: Epidemiologic findings and outcome after surgical intervention (1990-1999). *Veterinary Surgery, 32*(1), 21-29.

Littlewood, K. E., & Mellor, D. J. (2016). Changes in the welfare of an injured working farm dog assessed using the Five Domains Model. *Animals, 6*(9), 58-58.

Marra, M. A., Vanheule, V., Fluit, R., Koopman, B. H. F. J. M., Rasmussen, J., Verdonschot, N., & Andersen, M. S. (2015). A subject-specific musculoskeletal modeling framework to predict in vivo mechanics of total knee arthroplasty. *Journal of Biomechanical Engineering-Transactions of the Asme, 137*(2).

Meij, B. P., Suwankong, N., Van der Veen, A. J., & Hazewinkel, H. A. W. (2007). Biomechanical flexion-extension forces in normal canine lumbosacral cadaver specimens before and after dorsal laminectomy-discectomy and pedicle screw-rod fixation. *Veterinary Surgery, 36*(8), 742-751.

Meij, B. P., & Bergknut, N. (2010). Degenerative lumbosacral stenosis in dogs. *Veterinary Clinics of North America-Small Animal Practice, 40*(5), 983.

Mellor, D. J., Patterson-Kane, E., & Stafford, K. J. (2009). *The Sciences of Animal Welfare*. Oxford, UK: Wiley-Blackwell.

Mellor, D. J., & Beausoleil, N. J. (2015). Extending the 'five domains' model for animal welfare assessment to incorporate positive welfare states. *Animal Welfare, 24*(3), 241-253.

Moore, G. E., Burkman, K. D., Carter, M. N., & Peterson, M. R. (2001). Causes of death or reasons for euthanasia in military working dogs: 927 cases (1993-1996). *Journal of the American Veterinary Medical Association, 219*(2), 209-214.

Morgan, J. P., Bahr, A., Franti, C. E., & Bailey, C. S. (1993). Lumbosacral transitional vertebrae as a predisposing cause of cauda-equina syndrome in german-shepherd dogs - 161 cases (1987-1990). *Journal of the American Veterinary Medical Association, 202*(11), 1877-1882.

Pellikaan, P., van der Krogt, M. M., Carbone, V., Fluit, R., Vigneron, L. M., Van Deun, J., & Koopman, H. F. J. M. (2014). Evaluation of a morphing based method to estimate muscle attachment sites of the lower extremity. *Journal of Biomechanics, 47*(5), 1144-1150.

Pintar, F. A., Yoganandan, N., Myers, T., Elhagediab, A., & Sances, A. (1992). Biomechanical properties of human lumbar spine ligaments. *Journal of Biomechanics, 25*(11), 1351-1356.

Pressel, T., Bouguecha, A., Vogt, U., Meyer-Lindenberg, A., Behrens, B., Nolte, I., & Windhagen, H. (2005). Mechanical properties of femoral trabecular bone in dogs. *BioMedical Engineering OnLine, 4*(17).

Pronk, G. M., & Vanderhelm, F. C. T. (1991). The palpator - an instrument for measuring positions of bones in 3 dimensions. *Journal of Medical Engineering & Technology, 15*(1), 15-20.

Putzer, M., Ehrlich, I., Rasmussen, J., Gebbeken, N., & Dendorfer, S. (2015). Sensitivity of lumbar spine loading to anatomical parameters. *Journal of Biomechanics*.

Sacks, R. D., & Roy, R. R. (1982). Architecture of the hindlimb muscles of cats - functional-significance. *Journal of Morphology, 173*(2), 185-195.

Saunders, F. C., Cave, N. J., Hartman, K. M., Gee, E. K., Worth, A. J., Bridges, J. P., & Hartman, A. C. (2013). Computed tomographic method for measurement of inclination angles and motion of the sacroiliac joints in german shepherd dogs and greyhounds. *American Journal of Veterinary Research, 74*(9), 1172-1182.

Schmidt, T. A., An, H. S., Lim, T. H., Nowicki, B. H., & Haughton, V. M. (1998). The stiffness of lumbar spinal motion segments with a high-intensity zone in the anulus fibrosus. *Spine, 23*(20), 2167-2173.

Shahar, R., & Milgram, A. (2001). Morphometric and anatomic study of the hind limb of a dog. *American Journal of Veterinary Research, 62*(6), 928-933.

Shahar, R., & Banks-Sills, L. (2004). A quasi-static three-dimensional, mathematical, three-body segment model of the canine knee. *Journal of Biomechanics, 37*(12), 1849-1859.

Sharir, A., Milgram, J., & Shahar, R. (2006). Structural and functional anatomy of the neck musculature of the dog (canis familiaris). *Journal of Anatomy, 208*(3), 331-351.

Stafford, K. J. (2006). *The Welfare of Dogs*. Dordrecht, Netherlands: Springer.

Stafford, K. J. (2013). *Animal Welfare in New Zealand*. Cambridge, New Zealand: New Zealand Society of Animal Production Inc.

Tafazzol, A., Arjmand, N., Shirazi-Adl, A., & Parnianpour, M. (2014). Lumbopelvic rhythm during forward and backward sagittal trunk rotations: Combined in vivo measurement with inertial tracking device and biomechanical modeling. *Clinical Biomechanics, 29*(1), 7-13.

Van Der Helm, F. C. T., & Veenbaas, R. (1991). Modelling the mechanical effect of muscles with large attachment sites application to the shoulder mechanism. *Journal of Biomechanics, 24*(12), 1151-1164.

Van Der Helm, F. C. T., Veeger, H. E. J., Pronk, G. M., Van Der Woude, L. H. V., & Rozendal, R. H. (1992). Geometry parameters for musculoskeletal modelling of the shoulder system. *Journal of Biomechanics, 25*(2), 129-144.

Wachs, K., Fischer, M. S., & Schilling, N. (2016). Three-dimensional movements of the pelvis and the lumbar intervertebral joints in walking and trotting dogs. *Veterinary Journal, 210*, 46-55.

Wilke, H. J., Wenger, K., & Claes, L. (1998). Testing criteria for spinal implants: recommendations for the standardization of in vitro stability testing of spinal implants. *European spine journal : official publication of the European Spine Society, the European Spinal Deformity Society, and the European Section of the Cervical Spine Research Society, 7*(2), 148-154.

Worth, A. J., Sandford, M., Gibson, B., Stratton, R., Erceg, V., Bridges, J., & Jones, B. (2013). Causes of loss or retirement from active duty for New Zealand police German shepherd dogs. *Animal Welfare, 22*(2), 167-174.

Worth, A. J. (2014). *A study of debilitating orthopaedic conditions of working new zealand police german shepherd dogs.* (Doctoral dissertation), Massey University, Palmerston North, New Zealand.

Young, L. L., Papa, C. M., Lyon, C. E., George, S. M., & Miller, M. F. (1990). Comparison of microscopic and laser differaction methods for measuring sarcomere lengths of contracted muscle-fibers of chicken pectoralis major muscle - research note. *Poultry Science, 69*(10), 1800-1802.

Zimmerman, M. C., Vuonohawkins, M., Parsons, J. R., Carter, F. M., Gutteling, E., Lee, C. K., & Langrana, N. A. (1992). The mechanical properties of the canine lumbar-disk and motion segment. *Spine, 17*(2), 213-220.